UNIVERSITY OF NOVA GORICA
GRADUATE SCHOOL

DEVELOPMENT OF THE CONFOCAL PIXE SET-UP FOR MULTIELEMENTAL DEPTH RESOLVED MEASUREMENTS AND THREE-DIMENSIONAL MICROSCOPY

DISSERTATION

Nataša Grlj

Mentors:
doc. dr. Primož Pelicon
doc. dr. Matjaž Žitnik

Nova Gorica, 2012

UNIVERZA V NOVI GORICI
FAKULTETA ZA PODIPLOMSKI ŠTUDIJ

RAZVOJ SISTEMA ZA SOGORIŠČNO METODO PIXE TER UPORABA PRI VEČELEMENTNIH GLOBINSKIH MERITVAH IN TRIDIMENZIONALNI MIKROSKOPIJI

DISERTACIJA

Nataša Grlj

Mentorja:
doc. dr. Primož Pelicon
doc. dr. Matjaž Žitnik

Nova Gorica, 2012

Da je tale dizertacija ugledala luč sveta, odgovornosti ne nosi samo avtorica, temveč mnogi drugi, ki so v raziskavah sodelovali. To je le delni seznam tistih, ki jih zahvala nikakor ne more zaobiti.

V prvi vrsti bi se rada zahvalila mentorjema, doc.dr. Primožu Peliconu in doc.dr. Matjažu Žitniku. Piljenje teksta je velik prispevek, pa vendar ne edini. Vsa pomoč, nasveti in ves trud, ki sta ga v teh letih vložila vame in v moje delo, niso izmerljivi in se jih ne da poplačati.

Nadalje najlepša hvala za izjemno vzdušje celotnemu timu Mikroanalitskega centra. Predvsem pa najbližjim sodelavcem Primožu Vavpetiču, dr. Pauli Pongrac, Gašper Kukec-Mezku in Luku Jeromelu. Pa seveda dr. Davidu Jezeršku in dr. Andreju Miheliču za premnoge pogovore o življenju, vesolju in nasploh vsem.

I would like to express my gratitude to both groups we started the CF PIXE method with. The coworkers from Athens, mostly prof.dr. Andreas Karydas and dr. Dimosthenis Sokaras and from Berlin, Roman Schütz and specially prof.dr. Birgit Kanngießer put all their expertise in this, as in all of their work. Their help and understanding is greatly appreciated.

Thanks to dr. Melanie Bailey from the University of Surrey who provided the gunshot residue samples and helped me peeked into the field of forensics.

Zahvala gre seveda tudi Frantzu Gasserju, za razvoj in izdelavo mehanskih komponent, od nosilcev za vzorce, za leče, do detektorskega sistema. Sodelovati z vami je privilegij.

Doktorsko delo je potekalo pod pokroviteljstvom Javne agencije za raziskovalno dejavnost Republike Slovenije v okviru programa mladih raziskovalcev na osnovi pogodbe št. 1000-08-310257.

The work was also partially supported by the European Community as an Integrating Activity "Support of Public and Industrial Research Using Ion Beam Technology (SPIRIT)" under EC contract No. 227012. Transnational access was an opportunity to work with numerous European scientists from different fields. This was a great experience.

Zahvala pa gre seveda še vsem tistim, ki direkno z doktorskim delom niso imeli nič, je pa njihovo znanstvo, prijateljstvo in včasih potrpljenje veliko bolj pomembno.

Na koncu pa še pogled k družini. Žigi, ki vztraja z mano, ter Vilku in Dubravki, brez katerih tako ne bi bilo nič. Tale bukvica je posvečena vam.

Abstract

Proton induced X-ray spectroscopy with focused proton beam, known as micro-PIXE method, is a powerful tool for the quantitative analysis of elemental distribution in the sample. The proton beam that is focused down to a micrometer level, penetrate the sample without significant spread. As it is possible to deflect the beam electromagnetically, the sample can be raster-scanned by the beam. The method combines both high elemental sensitivity and lateral resolution, however depth distribution of elements can not be directly measured. A way to approach this problem is by the restriction of the field of view of the X-ray detector with an X-ray lens in the so-called confocal PIXE arrangement. Collecting intensity profile of the polycapillary lens can be described with an axially-symmetric Gaussian function. The application of the lens allows distinction of detected signals from different depths. Three-dimensional elemental distribution in the sample could be measured by beam scanning and sample translation.

A dedicated confocal PIXE set-up was constructed at the microbeam experimental chamber at the tandem accelerator at the Jožef Stefan Institute. The system is composed of a silicon-drifted X-ray detector and a polycapillary X-ray half-lens attached to the X-ray detector. The detector and the lens are configured to combine reasonable depth resolution and acceptable working distance. The detector arm load-lock system and the snout-alignment interface were designed to allow a fast and accurate alignment of the confocal set-up.

Polycapillary X-ray lenses must be characterized individually for their performance in the collecting mode of application. Therefore the available lenses were studied in detail. The full width at half maximum was measured for each lens at different X-ray energies, the transmission efficiency and the effects of the lens on the shape of the X-ray spectra were discussed, including properties that limit the applicability, such as asymmetry of the sensitive volume and "halo" effect. The obtained data on the lens characteristics were successfully used to interpret the measured results on standard reference materials.

The simplest application of CF PIXE is depth-resolved analysis of layered materials. Two types of measurements are feasible – a beam- or a sample-scanning mode. In the scope of this work, the method is demonstrated on two samples – an artificially made layered material and a cooper sample coated with tin.

Emphasis was given on the element specific three-dimensionally resolved analysis. Three-dimensionally-shaped samples can be analyzed with CF PIXE, even when they are too thick to be transparent for protons with the energy of few MeV or photons within several keV energy range. The general procedure for the 3D elemental reconstruction is described and different aspects in the excitation-emission processes are considered. An example of such analysis is shown on a gunshot residue particle. The 3D distribution of the two elements, Ti and Zn, that

compose the GSR microparticle is reconstructed.

At the end, some limitations of the CF PIXE method are discussed.

PACS (2010): 78.70.En, 41.50.+h, 87.64.mk, 87.59.-e, 29.20.Ej, 29.30.Kv, 07.85.Nc

Key words: confocal PIXE, micro-PIXE, polycapillary lens, X-ray lens, polycapillary conic collimator, X-ray spectra, depth profiling, 3D imaging, 3D elemental distribution, nuclear microprobe, high-energy focused ion beam

Povzetek

Spektroskopija rentgenskih žarkov vzbujenih s fokusiranim protonskim žarkom, znana pod imenom mikro-PIXE, je uveljavljena metoda za določanje elementne sestave snovi. Omogoča hkratno detekcijo elementov v sledovih, kvantifikacijo koncentracij brez umerjanja z referenčnimi materiali in prilagoditev meritev tako vzorcem, ki jih postavimo v vakuum, kot tudi večjim in dragocenim predmetom, ki jih pomerimo na zraku. S fokusiranim protonskim žarkom se lahko premikamo po vzorcu in izmerimo površinsko porazdelitev elementov v njem. Protonski žarek prodre v snov in vzbuja karakteristične rentgenske žarke tudi v globini nekaj deset mikrometrov, vendar zaradi velikega prostorskega kota, ki ga pokrijejo rentgenski detektorji, ne razločimo, v kateri globini so nastali. Tako dosegamo pri metodi mikro-PIXE zelo dobro površinsko ločljivost, določeno z velikostjo protonskega žarka, ne razločimo pa globinske porazdelitve. To informacijo lahko izluščimo s postavitvijo rentgenske leče pred detektorjem rentgenskih žarkov. Leča zmanjša vidno polje, poleg tega pa ima ovojnica vstopnih žarkov intenzitetni profil, ki ga lahko opišemo z osno-simetrično Gaussovo funkcijo. V konfokalnem meritvenem načinu pripeljemo skupaj protonski žarek in gorišče leče. Na ta način lahko razločimo signale, ki prihajajo iz različnih globin. V kombinaciji s premikanjem protonskega žarka in vzorca lahko izmerimo tridimenzionalne porazdelitve elementov v vzorcu.

Na Mikroanalitskem centru Instituta Jožefa Stefana smo na mikrožarkovni liniji postavili sistem za konfokalno metodo PIXE (angl. confocal PIXE, CF PIXE). Njegova glavna sestavna dela sta nov silicijev rentgenski detektor s prečnim zbiranjem naboja (angl. silicon-drifted detector, SDD) in rentgenska polikapilarna leča. Ključno pri izbiri detektorja je bilo dejstvo, da ne potrebuje zunanjega hlajenja s tekočim dušikom, temveč zadostuje Peltierjev termočlen. Tako zmanjšamo maso celotne konstrukcije in omogočimo lažjo in stabilnejšo poravnavo. Med pripravo sistema smo skonstruirali nosilca za detektor in lečo ter izdelali vmesnik, s katerim natančno poravnamo os detektorja in leče. Pri izbiri leče smo upoštevali kompromis med optimalno globinsko ločljivostjo, ki jo pretežno določa velikost netočkastega lečinega gorišča, med sprejemljivo delovno razdaljo ter prepustnostjo. S proizvajalcem smo za metodo pripravili tri različne rentgenske leče in izbrali tisto z najboljšimi lastnostmi.

Vsako rentgensko lečo je potrebno karakterizirati v izbranem načinu uporabe. Tako smo za vse tri leče izmerili njihove lastnosti za uporabo pri metodi CF PIXE. V delu so podani rezultati analiz razsežnosti ovojnice v odvisnosti od oddaljenosti od roba leče ter velikosti gorišča v odvisnosti od energije rentgenskih žarkov. Prav tako smo raziskali, kaj se dogaja s prepustnostjo leče in kako se pozna njen vpliv na obliko izmerjenega rentgenskega spektra. Preučili smo tudi pojav asimetrije pri koničnem kolimatorju (angl. polycapillary conic collimator, poly-CCC) in "halo" efekt, ki zmanjšujeta uporabnost izbranega optičnega elementa. Če lastnosti

leče izmerimo dovolj natančno, lahko poleg elementne sestave v vzorcu dobimo tudi njihovo koncentracijo. To smo poskušali preveriti pri meritvah z Ni in Ti standardom.

Prikazali smo različne uporabe metode CF PIXE. Globinske elementne profile večplastnih struktur izmerimo na dva načina: s premikanjem žarka po mirujočem vzorcu ali s premikanjem vzorca vzdolž smeri mirujočega žarka. S premikanjem protonskega žarka po mirujočem vzorcu smo določili globinsko porazdelitev plasti v umetno izdelani večplastni strukturi ter v pokositrani bakreni ploščici.

Natančno smo se posvetili meritvam tridimenzionalnih elementnih porazdelitev. Metoda CF PIXE je uporabna tudi za vzorce, ki niso presevni za protone z energijo nekaj MeV oziroma za fotone z nekaj keV energije. V tem primeru lahko rekonstruiramo del vzorca, ki ga določa t.i. informacijska globina. V delu smo prikazali postopek meritev ter postopek rekonstrukcije tridimenzionalne porazdelitve elementov v mikrodelcu, dobljenem iz ostankov streljanja (ang. gunshot residue) s strelivom Sintox. V delcu opazimo dva dominantna elementa, Ti in Zn, ki ju izmerimo z metodo PIXE. Običajno uporabljene metode forenzične analize ne morejo izmeriti tridimenzionalne porazdelitve elementov v delcih ostankov streljanja. S pomočjo metode CF PIXE smo rekonstruirali položaj in koncentracijo Ti in Zn v delcu. Čeprav je globinska resolucija slabša od površinske (10 μm vs. cca. 1 μm), lahko v vzorcu s premerom nekaj deset mikrometrov določimo porazdelitvi obeh elementov in potrdimo prisotnost koncentracijsko osiromašenega območja v centru.

Za konec smo opisali primere, s katerimi pokažemo na omejitve konfokalne metode PIXE.

Stvarni vrstilec, PACS (2010): 78.70.En, 41.50.+h, 87.64.mk, 87.59.-e, 29.20.Ej, 29.30.Kv, 07.85.Nc

Ključne besede: konfokalna metoda PIXE, mikro-PIXE, polikapilarne rentgenske leče, rentgenska optika, rentgenski spektri, elementna globinska analiza, 3D slikanje, 3D elementna porazdelitev, jedrska mikrosonda, fokusirani ionski žarki

Contents

List of Figures

List of Tables

Abbreviations

Methods:

IBA ion beam analysis
PIXE particle induced X-ray emission
PIGE particle induced γ-ray emission
NRA nuclear reaction analysis
RBS Rutherford backscattering spectroscopy
EBS elastic backscattering spectroscopy
ERDA elastic recoil detection analysis
STIM scanning transmission ion microscopy
CT, μ-CT computed tomography, micro computed tomography
XRF X-ray fluorescence
CF PIXE confocal PIXE
SEM scanning electron microscopy
EDS energy-dispersive X-ray spectroscopy – a term used with electron excitation

Facilities and companies:

JSI Jožef Stefan Institute, Slovenia
MIC Microanalytical center at the Jožef Stefan Institute
AGLAE Accélerateur Grand Louvre d'Analyse Elémentaire (Tandem accelerator at the CNRS laboratory of the Louvre museum, Paris)
CNRS National Center for Scientific Research, France
LENP The Institute of Low Energy Nuclear Physics, Beijing, China
IfG Institute for Scientific Instruments, Berlin, Germany
XOS X-ray optical systems, New York, USA
ITN Campus tecnologico e nuclear (Nuclear and Technological Campus, Lisbon, Portugal)

Devices:

HPGe high purity germanium detector

Si(Li) lithium-drifted silicon detector
SDD silicon-drifted detector
CCD charge-coupled device
polyCCC polycapillary conic collimator
lens A first tested polycapillary half-lens 58mkl14
lens B second tested polycapillary half-lens 119mmkl03
PCXRL polycapillary X-ray lens
PCXRHL polycapillary X-ray half-lens
CRLs compound refractive multiple lenses

Samples/targets:

GSR gunshot residue (particle)
S14P1 stub 14, particle 1; the analyzed sample of gunshot residue particle
PES polyester fiber

Miscellaneous:

2D two-dimensional
3D three-dimensional
FWHM full width at half maximum

Units used:

eV electron volt, unit of energy (1 eV = $1.6 \cdot 10^{-19}$ J), together with keV, MeV
amu atomic mass unit (1 amu = $1.66 \cdot 10^{-27}$ kg)
ppm parts per million – a common description of elemental concentration in spectroscopic methods (1% = 10000 ppm)
ppb parts per billion
Hz Herz, unit of frequency (1 Hz = 1 s^{-1})
A Ampere, unit of current; together with pA, nA, μA
kg kilogram, unit of mass; together with g, mg, μg
m meter, unit of length; together with cm, mm, μm, nm
barn unit used for the ionization cross-sections (1 barn = 10^{-24} cm^2)
bar unit of pressure (1 bar = 100000 $\frac{N}{m^2}$)
mol unit used to express amounts of a chemical substance

Chapter 1

Introduction

1.1 Field overview

The field of material characterization covers a wide range of different techniques and methods that are used for determination of the material composition and structure. The addressed material properties include the elemental and chemical composition, as well as various thermal, electrical and magnetic properties. Required instrumentation for the material characterization include handy set-ups, tabletop systems, as well as accelerators, storage rings or lasers. Electrostatic accelerators are routinely used for the analysis and modification of materials with fast ions with the energies ranging from few tens of keV to several MeV/amu. The most common application of the so-called IBA (Ion Beam Analysis) methods is measurement of the elemental distribution in the sample. In particular cases, even chemical states could be determined. The most widely used IBA methods are PIXE (particle induced X-ray emission), PIGE (particle induced γ-ray emission), NRA (nuclear reaction analysis), as well as several scattering-based techniques, such as Rutherford backscattering spectroscopy (RBS), elastically backscattering spectroscopy (EBS) and ERDA (elastic recoil detection analysis). Low ion beam intensities in the order of nA result in low and controllable beam damage. In addition, ions with the energy of several MeV penetrate the sample and excite signals below the surface monolayers. IBA could be therefore executed in moderate vacuum conditions and without dedicated preparation of sample surfaces.

PIXE is an established quantitative ion beam analytical method for determination of elemental concentrations in the sample. It is based on the detection of characteristic X-rays, emitted by target atoms after the irradiation with fast proton beam. PIXE en-

ables simultaneous detection of elements in a wide range of the periodic table, starting approximately with Na and going up to heavy U atoms. The energy of Na K_α line is 1041 eV and is detectable in vacuum with most of the standard X-ray detectors, while for heavy elements like U, L lines (E_{L_α} = 13.615 keV) or even M (E_{M_α} = 3.171 keV) lines are used for detection. Large proton range and relatively small spectral background result in high sensitivity of the method for trace elements in the amount of μg per g (ppm). No special sample preparation is normally required and the damage of the specimen, confined to the irradiated area, may be controlled by beam parameters like current, beam diameter and time of the analysis [1].

The RBS and EBS methods rely on the interpretation of the energy spectrum of the projectiles backscattered from the sample. Due to the collision dynamics, the energy loss of the scattered projectile depends on the type of the scattering center, its concentration and on the depth of the nuclei. All types of ions can be used, but as the kinematic factor depends on the ratio between the projectile mass and mass of the target atom, the type of the incoming beam must be carefully chosen regarding the application. When protons are used as projectiles, the cross-section are non-Rutherford and we designate the method as EBS. The EBS technique may be executed in parallel with PIXE [2]. ERDA is a complementary method to RBS. It is based on the energy analysis of ions ejected from the target in the forward direction by fast incident ion that hit the sample under small angle with respect to the surface. It is one of the rare methods for depth concentration profiling of light elements, including hydrogen. The projectile ions and the energies are chosen for the purpose of the application. Ions heavier than protons, such as ^{4}He or ^{7}Li, are used to achieve the desired sensitivity [3]. Impact of ions with the energy of few MeV triggers nuclear excitation in the target nuclei. The nuclear excitation in some cases causes the emission of gamma-rays. The analytical technique employing this phenomenon is called particle induced gamma-ray emission (PIGE) and can be used as a complementary technique to PIXE for detection of light elements with atomic number below Si. The evaluation of concentrations from PIGE measurements is simple in comparison with PIXE, due to very low attenuation of γ-rays in the sample. However, as the method is isotope specific, the result interpretation can be demanding [4]. Incident ions may also induce particle–particle nuclear excitation. Detection of emitted proton or α particle results in a high sensitivity for a specific light isotope. The method is known as nuclear reaction analysis (NRA) [3].

The tandem ion accelerator at the Microanalytical center (MIC) of the Jožef Stefan institute (JSI) offers four beamlines and five experimental stations where most of the above mentioned IBA methods are employed. External beam is used for PIXE, PIGE

and RBS measurements of big or valuable objects that can not be inserted into vacuum [5]. In the microbeam experimental station, ion beam is focused down to a micrometer level and different methods (PIXE, RBS, STIM, ERDA and NRA) are used to determine lateral elemental profiles [6]. Standard PIXE station enables automatized measurements of large series of samples with broad beam PIXE, while ERDA/RBS station is used for the analysis of hydrogen and deuterium in various materials [7]. High-resolution spectrometer mounted at the beamline at -30° is able to resolve features in the X-ray spectra with high resolution [8] and is used for measurements in the atomic physics. It allows also chemical speciation of specific sample types based on the spectral energy shifts [9].

All the available ion beam methods are used for the characterization of various types of samples, however the geometrical structure of the sample plays an important role for the applicability of every individual technique.

The calculation of the sample composition from the yields of characteristic X-rays obtained by PIXE is straightforward in the case of thin homogeneous foils, as well as the flat thick samples. Both types can be analyzed by a variety of methods and such samples are usually used as standard reference materials. In many cases, the distribution of elements in real thick samples is not homogeneous, however this information is not crucial for the analysis. Using broad-beam PIXE, the elemental concentrations are averaged over the area covered by the beam. The technique is used for the analysis of the samples in many fields, one example are objects of the historic or cultural heritage [10] or the objects of the environmental studies like aerosols [11]. In such cases, the broad beam PIXE is sometimes combined with simultaneous PIGE to obtain concentrations of light elements.

Samples, whose lateral distribution of elements is not homogeneous, can be analyzed with μ-beam, where a focused beam is used and a position-selective excitation becomes possible. The nuclear microprobe at Jožef Stefan Institute focuses the proton beam down to 1×1 μm^2 and the scanning possibilities of a high-energy focused proton beam allow to generate two-dimensional maps of elemental distribution in the sample by a conventional X-ray spectrometer [6]. The applications of micro-PIXE with its ability of quantitative elemental mapping are taking place at the fields of biology [12–14], nanotoxicology [15], geoscience [16], space geology [17], environmental sciences [18], medicine [19] etc.

Another type of samples are those with a non-uniform elemental depth distributions, for example layered materials, that can be described as laterally homogeneous but with

the nontrivial elemental depth distribution. To some extent, depth sensitivity can be achieved with PIXE in combination with other IBA techniques, like RBS [20, 21]. This combination is successful, however the obtained information about the composition is limited in depth range. On the other hand, the stand alone differential PIXE method is based on the cumulative effects that occur when incident energy [22], or the proton beam impact angle [23] is changed. A strong dependence of the X-ray ionization cross section with respect to the proton beam energy and correspondingly with the depth at which the X-ray production takes place, forms a basis of this method that became an established tool for quantitative characterization of simple layered structures [24, 25]. However, the corresponding analysis is demanding and difficulties can be encountered in some cases, e.g. when changing the microbeam energy.

The most general object for the analysis would be a "potato-shaped" three-dimensional multi-elemental particle. The quantitative reconstruction of the three-dimensional elemental distribution with a micrometer resolution within a sizable object is a tough challenge for any analytical method. However, depending on the sample size, there are few options. If the size of the particle is smaller then the range of the ion beam, several techniques exist, all of them based on the measurements of the transmitted flux at various sample orientation. In PIXE/STIM tomography, the sample is sequentially rotated and the energy loss of the primary proton beam is measured at each position together with the emitted X-ray spectrum [26–30]. In this way, three-dimensional elemental structure of the microparticle could be determined by a complex numerical reconstruction [31, 32]. This is an upgrade of a standard STIM tomography [33], where only three-dimensional distribution of different densities in the sample can be obtained. The problem of both tomographies is the need of sample rotation around one fixed axis, however the most important disadvantage is the need of the sample inclusion in a capillary, which may not be suitable for all sample types.

Similar information can be obtained with μ-CT [34]. Here, the proton microbeam strikes the monoelemental target creating a point-like X-rays source with lateral area of 1 μm^2. This secondary diverging beam irradiates the sample and an image of the transmitted flux at each angle position is collected by a CCD camera. That way the information is gathered about the average attenuation coefficient along different paths of the sample. The method is similar to standard CT where high energy X-rays ($\sim$ 60 keV) are used and the images reflecting the object density are obtained [35]. When lower X-ray energies that can be selected by the foil type are used, the μ-CT images emphasizing the contribution of specific elements can be taken.

Eventually, the protons from the monoenergetic beam will stop at certain sample depth and emitted X-rays will be completely absorbed after traveling some finite distance in the target. There is therefore an inherent depth range of the IBA methods. While the sample may be too thick to allow the proton or X-ray beam transmission, there is always a possibility to collect the backscattered particles and/or emitted photons and thus gaining at least some depth information about the sample. To achieve three-dimensional resolution in such case, in addition to the micro-probe that provide good lateral resolution, the detector device is needed that collects particles from only small area of the sample and thus providing depth resolution. Regarding the reachable depth of the object, X-rays are more suitable than backscattered projectiles.

For most X-ray spectroscopies, standard solid state detectors are used with relatively broad solid angle. When proton beam strikes the target, protons ionize target atoms along their path. The ionized atoms emit characteristic X-rays along the proton path, however, the standard detector detects X-rays emitted along the way without discrimination, regardless of their point of origin, since the emission time differences are too small to be detected by the electronics. Even though the elemental composition is changing in depth and so the abundance of the emitted characteristic X-rays, the information about the creation points of particular type of X-rays is lost. The way to establish this sensitivity is to isolate parts of the sample and to detect X-rays selectively. In an ideal case, a small (micrometer size or less) collectible areas would be desired, however, this is currently not achievable with a present state of the technology.

A simple way of restricting the detector's field of view is the use of a series of pinhole collimators. Two pinholes with proper separation can create a very small sensitive solid angle. When it is overlapped with the focal "'point"' of the primary beam, a small probing volume is created in the so-called confocal set-up. However the efficiency of such a simple approach would be extremely low and the achieved count rate too small for practical purposes. The restriction must be done in such a way that the collecting solid angle remains relatively large. A possible way to achieve this is the use of an X-ray optic element or a "lens" in front of the detector. An ideal X-ray lens used for this purpose would have to have a small focal size, large collection solid angle, high lateral resolution, the relatively long focal length suitable for the application and high lens transmission.

The field of X-ray optics covers a wide range of X-ray optical elements that exploit diffraction and refraction phenomena as well as the total external reflection phenomena. Among them are various Fresnel optical elements (zone plates), diffraction grat-

ings, natural crystals or artificial heterostructures used for diffraction, Kirkpatrick-Baez mirrors, refractive X-ray optics and also capillary X-ray optics [36]. In the last twenty years all these optical systems have experienced an impressive development in terms of the production quality as well as in the range of applications that go hand in hand with the development of synchrotron facilities and the application of synchrotron light.

Not all the focusing optics is suitable for the discussed applications in the confocal spectroscopy. Fresnel zone plates are highly efficient but small optical systems used mainly for focusing the collimated radiation (from a synchrotron beam) on the sub micron cross-sections [37]. Also an efficient point-to-point imaging is possible, provided the object is not too distant from the lens, whose dimension ranges to a few 100 μm. However, Fresnel lenses feature strong aberration, spherical as well as chromatic [36]. Besides small efficiency, this is the main disadvantage for their use in confocal spectroscopy, where the characteristic X-rays of different energies for a series of analyzed elements would have to be detected simultaneously. Focusing optics, based on a diffraction is again not suitable due to the energy dispersion effects and low efficiency [38]. The reflection optics for X-rays working in Kirkpatrick-Baez geometry is free of astigmatism [39], but it works effectively only at small glancing angles which is again suitable for focusing collimated beams [40]. As a contrast to this mentioned systems, compound refractive multiple lenses (CRLs) are based on refraction of X-ray beam on spherical-shaped holes made inside of solids. The multiple number of "converging lenses" used, reduces the focal distance, which can amount tens of meters if only one such lens is used [41]. Using parabolically shaped structures, the spherical aberrations encountered in such systems can be removed [42]. A particular problem of such lenses is a high absorption and the need of a collimated beam, making CRLs highly effective only for brilliant synchrotron sources.

As it turns out, the only optical elements at the moment, suitable for confocal spectroscopy are special polycapillary arrays with curved or straight channels, namely polycapillary X-ray lenses, half-lenses or a polycapilary conic collimators. X-ray half-lenses use multiple external total reflections in special geometry of a bundle of hollow tubes along which the light is transmitted. The ability to guide X-rays along the slightly bended tube is employed to collect, collimate or focus X-ray light. When such X-ray lens is placed in front of the X-ray detector and the narrow acceptance solid angle of a polycapillary lens with its focal point is aligned with the focus of the proton beam, a confocal set-up is established. This new method, the confocal PIXE, was established according to the analogy of the confocal or 3D X-ray fluorescence method (XRF) that

uses X-rays as a primary beam [43].

In 3D XRF, another X-ray polycapillary is used to focus the incoming photon beam that defines the probing volume together with the polycapillary lens in the detection channel. X-ray focusing at the excitation side can be obtained by other means as well, however the use of the polycapillary lens enables the stability of the set-up, no matter of the energy setting of the primary beam. The CF (3D) XRF method is being developed since 2003 and evolved into analytical tool for in-depth analysis [44, 45]. It may be set in the laboratory environment with X-ray tube sources, but has been proven especially efficient when coupled with intense and tunable synchrotron radiation source. At present, its spatial resolution is limited to about 20 μm in all three directions determined by the polycapillay FWHM-s. As the two polycapillary lenses are used, accurate mechanical alignment is necessary in order to create the smallest possible and well-defined probing volume. As the probing volume is driven through the sample by moving the sample, precise mechanics that control sample holder movement is required. On the other hand, there are several advantages of 3D XRF in comparison with CF PIXE. In principle, the X-rays attenuation length in matter is comparable to the range of a few MeV protons, however the photo-absorption cross-section is not dependent on the path traveled. The yields from the interior of the sample are in general larger than in the case of proton excitation. The energy of the primary X-rays can be tuned in order to emphasize the contribution of different elements and chemical sensitivity is an option if high energy resolution is employed in either the excitation or the detection channel. This feature is not available in the case of the proton beam excitation and can be useful for practical applications. 3D XRF can be set with conventional X-ray sources, thus forming a practical table-top system.

As CF PIXE is created with the focused proton beam, the typical lateral resolution of the method is around 1 μm^2. Scanning possibilities of the microbeam enable fast lateral beam scanning, thus reducing the need of the lateral sample movement. The combination of focused proton beam, application of X-ray polycapillary lens at the X-ray detector and the ability to move the sample in precise micrometers steps in the beam direction enables depth-resolved measurements [46] and the elemental tomography studies of micro-particles [47]. Here, the probing volume from which X-rays are collected is driven through the sample by beam scanning or the sample movement in the direction perpendicular to the incoming beam only. Depth resolution remains in the order of a few tenths of micrometers and strongly depends of the focal size of the polycapillary lens applied. In our first attempts, the reconstruction of depth profiles for several types of samples was performed [46, 48] and in two special cases the

three-dimensional distributions of elements were recovered – a point 3D distribution of aerosols particles on the quartz filter [49, 50] and a general particle, containing only one visible element [47]. As the method developed, there was a growing need to construct a dedicated confocal PIXE set-up, the only existent one at similar ion accelerator facilities worldwide.

Confocal PIXE is being developed at JSI for the last few years since the first experiments in 2006 in collaboration with Technical University, Berlin and the National Center of Scientific Research "Demokritos", Athens. The only other reported confocal PIXE experiment was realized at the external micro-proton beam facility at the AGLAE tandem accelerator at the CNRS laboratory of the Louvre museum in Paris. A setup in air was installed to investigate artistic and archaeological objects [51]. The scientific community showed interest in the development of the CF PIXE. Recently, a research project was launched at ITN, Lisbon, to develop their own confocal PIXE system.

1.2 Aim of the thesis

The first attempts with the confocal PIXE arrangement at MIC were performed at existing X-ray detectors in a vacuum chamber in order to explore the performance and the possibilities of the method. The confocal set-up was obtained by installing polycapillary lens in front of the standard X-ray spectrometers. The polycapillary lenses were taken from 3D XRF and the alignment procedure was introduced to create the smallest possible probing volume. Although it is the most important part of any successful confocal experiment, the alignment was improvised by manually moving the X-ray detector together with the cryostat. Due to the heavy mass of the whole system and without precise mechanism that would allow movements in the direction perpendicular to the detector axis, this task was demanding and time-consuming.

The thesis deals with development of the CF PIXE method that was initiated in our laboratory with the improvised μ-PIXE set-up. The first task was to set up a new dedicated confocal PIXE system that would overcome or ease the problems encountered during the first try-outs of the method. One of the improvements would be to achieve accurate and fast mechanical alignment of the detector. To the purpose a Peltier-cooled silicon-drifted X-ray detector was implemented in order to avoid the use of heavy liquid nitrogen cryostat usually attached to semiconductor detectors for crystal cooling. A precise alignment mechanism was constructed, as well as a holder for eventual ab-

sorber foils and the lens. X-ray polycapillary lens was chosen after an extensive discussion with the manufacturer: during the CF PIXE set-up development, we have tested three different lenses and characterized their properties in the collecting mode. The final goal was to obtain a well characterized set-up with predictable performance that would allow a quantitative CF PIXE analysis. The construction of the system and the detailed characterization of lenses is described in Chapter 2. At the end of Chapter 2, the performance test of the constructed set-up on a standard material is reported.

The application of the confocal PIXE set-up in its various analytical modes and for diverse types of samples are discussed in the doctoral thesis. Depth-resolved measurement of layered target is a relatively straightforward application of CF PIXE. Such measurements in the sample scanning mode were already reported [48], and only a few additional measurements of this kind were repeated. More emphasis was given to the depth-resolving measurements in the beam scanning mode on layered samples (Chapter 3). The main attention was dedicated to the particle elemental micro-tomography. The work done is an upgrade of the two special cases, the reconstruction of the position of aerosol particles in quartz filter and the 3D elemental imaging of a hematite particle, that were measured and analyzed in our previous work [47, 50]. This time, efforts were given to describe deconvolution of signals acquired in a sequence of elemental maps in the case of generalized set-up geometry. Step by step solution to several problems encountered during the procedure related to the two-elemental reconstruction of a gunshot residue microparticle, used as an example, are presented in Chapter 4.

Finally, appendices A.1 and A.2 are added at the end of this work to describe several derivations that are needed for the analysis, but would interfere with the flow in the manuscript. Some of them can really be described in a few lines, however I believe it is fair to the potential reader not to let him/her be surrounded with statements of the type “it is easy to show”... Appendix B deals with the estimation of the secondary fluorescence contribution, that could in particular cases severely complicate the analysis.

Chapter 2

Development of the CF PIXE set-up

2.1 Ion microprobe at JSI

CF PIXE set-up is constructed as an independent detection system at the measuring station with high-energy focused ion beam, that is installed at the 10° exit port of the 2 MV Tandetron accelerator at the Microanalytical center of the Jožef Stefan Institute. The station is equipped with a magnetic quadrupole triplet lens known as OM triplet configuration [52], a motor driven slits, a precise five-axis goniometer and a spherically shaped measuring chamber. Two optical microscopes, two detectors for X-rays, Si detectors for scattered or transmitted ions and nuclear reaction products point to the sample positioned in the chamber's center. The samples are mounted on a movable sample holder. Recently installed load-lock system allows for the fast sample changing without vacuum destruction in the main experimental chamber, dedicated to the insertion of the frozen hydrated biological tissue samples [53].

The proton beam is focused down to a micrometer level by a magnetic quadrupole triplet lens. The two driving currents for the magnetic triplet lens are adjusted to form a beam focus at the focal point of the optical microscope with pixel resolution of 1.2 μm. The focal point coincides with the center of the spherical chamber. Therefore, when the sample is in the focal point of the microscope, the proton beam is focused at the target surface. The depth of field of view of the microscope is stretching over a distance of approximately 20 μm. In the case of target displacement from the beam focus within this distance, the resulting ion beam spread can be neglected. The proton beam current density in the plane that is perpendicular to the microbeam axis can be described by the product of two Gaussian curves. The corresponding beam full width at

half maximum (FWHM) in both perpendicular directions orthogonal to the ion beam is usually set to $1-2\,\mu$m. In the low current mode and with all possible vibration sources turned off, the beam FWHM can drop bellow 1 μm [6], however such circumstances are rarely met during the normal work. The beam diverges outside the focal plane along the beam direction and the two FWHMs are doubled at the distance of $\pm 450\,\mu$m [46]. This distance is much larger than the usual CF PIXE measurement interval. The proton energy used in the experiments is between 0.5 and 3 MeV.

Other types of ion beams used for other IBA applications can also be focused, however not as good as protons. For example, a 4.5 MeV ^{3}He ion beam with 300 pA current can be focused down to $4\times4\,\mu$m^2 [54] due to low available brightness of the ion source and correspondingly, large slit apertures used for the beam formation.

A possibility to deflect charged particle beams by electro-magnetic force enables the beam raster-scanning. In our case, a deflection coil mounted before the triplet lens allows magnetic beam scanning of the target surface over a predefined region of interest. Each detection event at the attached detectors is recorded for its energy and the position. This enables the elemental mapping. An example of elemental maps of P, K and Zn is shown in Figure 2.1 where quantitative elemental maps were obtained by combining the micro-PIXE results with STIM method at MIC [13].

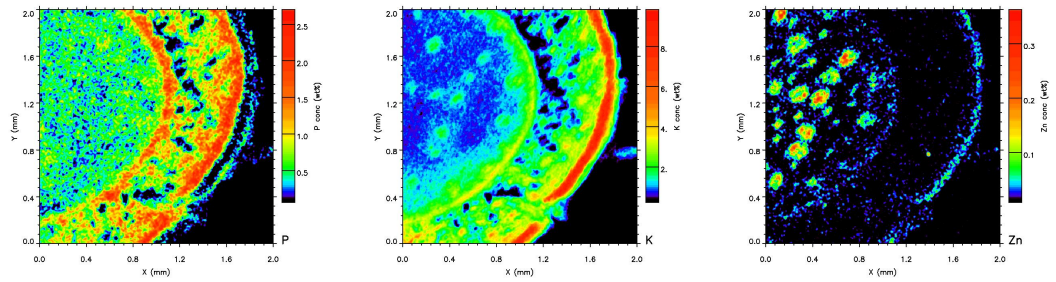

Figure 2.1: Quantitative elemental maps of P, K and Zn of a representative rhizome cross-section of Typha latifolia treated with 250 mM Pb in pots obtained with μ-PIXE method at JSI. Scan size 2×2 mm^2 [13].

An important feature of IBA methods is a possibility to determine observed elemental concentration quantitatively. One of the parameters required for the quantification is the proton dose. In our case, this is done by recording an RBS spectrum of projectiles backscattered from a 1 μm thick gold surface layer of a graphite chopper. The chopper intersects the proton beam with a frequency of approximate 10 Hz. RBS proton yield is recorded in parallel with the other spectra in a list mode. During the off-line data

processing, the spectrum accumulated by the proton beam chopper over the chosen scanning area can be extracted and used for the proton dose determination [55].

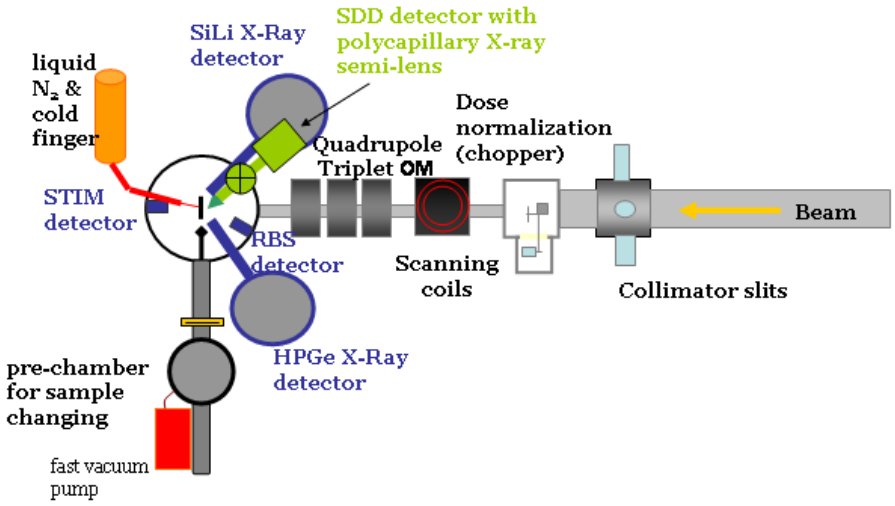

Figure 2.2: Schematic figure of the microbeam experimental chamber with its main parts: collimator slits, Au chopper for dose measurements, scanning coil, magnetic lens triplet for focusing, load-lock pre-chamber for sample changing, sample holder, HPGe and Si(Li) X-ray detectors, RBS and STIM detectors, new CF PIXE set-up and a cryostat with cold finger for frozen hydrated sample mounting.

The microbeam experimental chamber is equipped with a goniometer that allows sample movement in all three directions, as well as rotations in the polar and azimuthal planes. The spectra of X-rays emitted from the sample are measured simultaneously by two X-ray detectors -– a high purity germanium detector (HPGe) and lithium-drifted silicon detector (Si(Li)). The HPGe detector is positioned at an angle of 135° with respect to the proton beam direction and has a 25 μm thick beryllium window with a 100 μm thick kapton absorber in front, that can be changed if required by different applications. HPGe detector is used for the detection of heavier elements with characteristic X-rays with energy above K K_α line. The Si(Li) detector stands at 125° with respect to the beam direction in the horizontal plane and incorporates an 8 μm thick beryllium window. As it is equipped with significantly thinner absorber, it enables detection of low-energy X-rays in the energy region of 0.8 – 5 keV. In addition, a particle detector for backscattered ions is installed at the chamber, as well as a detection set-up for the measurements of the transmitted ion energy, based on the on-off axis geometry [56]. Each detected event by the set of detectors is recorded and saved in a list mode as a

sequence of detection channel, energy and the beam position (x,y) at the moment of the event.

For μ-beam experiments, a high vacuum of the order of 10^{-7} mbar is required. During the venting of the chamber all the detectors can be retracted in the dedicated load-lock systems and kept under vacuum conditions.

A schematic figure of the microbeam experimental chamber with the main instrumentation attached is presented in Figure 2.2. The chamber's position in the accelerator hall and its photograph are shown in Figure 2.3.

Figure 2.3: Photograph of the experimental hall of the Microanalytical centre at JSI with the Tandetron accelerator, four beamlines and five experimental stations. On the right is the closer photo of the microbeam chamber with Si(Li) (in front), HPGe (in the back), SDD and STIM detectors together with the corresponding load-lock systems, microscope camera, the target goniometer and cold arm for sample cooling.

2.2 The confocal PIXE set-up

Detector

In the first CF PIXE experiments, the systematic drift of detector position was observed of about 10 micrometers during a period of a single day due to evaporation of the liquid nitrogen in a cryostat. Also the alignment of X-ray detectors used for micro-PIXE was a complex and time-demanding procedure, as the detector support and its coupling to the chamber was not suitable for precise movement required by the alignment procedure. Therefore, the task was set to install a smaller and lighter detector device. Silicon-drifted Peltier-cooled X-ray detectors (SDD) overcome such limitations. Their operational temperature of around $-20°$C is obtainable with a double Peltier

thermoelectric element and there is no need for liquid nitrogen cooling. The scheme of the detector installed is shown in Figure 2.4. The detection crystal is enclosed in its own vacuum system inside the detector snout and separated from the sample region by an ultra-thin window with Al coating (AP 3.3, composed of MOXTEX polymer, DuraCoat® and aluminium layer). According to the detector technical specifications, it enables detection of Be K_α line at 109 eV with about 10% efficiency [57]. With crystal thickness of 450 μm it is therefore well suited for light element detection, and on the other hand it still provides reasonable detection efficiency at 10 keV. For most of the confocal experiments made, an additional 6 μm thick Mylar coated with Al was used as an absorber. Such a filter ensures 100% absorption of visible light and therefore reduces the noise of that origin.

The active volume of the crystal is 30 mm$^2 \times 450$ μm and is positioned 7.20 mm inside the detector snout. To reach this, the negotiations with the producer were held in order to bring the crystal as near to the edge as possible. The declared energy resolution at 5.9 keV for Mn K_α is 135-140 eV at a count rate of 3 kHz.

As the horizontal plane of the microbeam chamber was occupied with a pair of X-ray detectors for standard μ-PIXE measurements, the new SDD detector was positioned at an inclination angle of 30.3° from the horizontal plane. The azimuthal angle is 35° and the angle between the detector axis and the beam direction is 135° [58].

A set of metallic monoelemental samples were used for characterization of the spectrometer. Figure 2.5 shows one of the spectra measured with the SDD detector. The detector cool-down time after switching on the power is less then 1 min. Its energy resolution is 150 eV for the Ni K_α line at the energy of 7.5 keV. This approximately corresponds to the energy resolution of 142 eV for Mn K_α line.

Mechanical interface

The X-ray detector is installed on the retractable arm with a bellow and a gate valve. The translational mechanics allows translational movement of the SDD in and out of the chamber without the loss of vacuum. Additional support was constructed that allow controlled translations of the detector assembly perpendicular to the main translational axis. In this way, it is possible to position the detector snout with the lens attached to the desired position with a precision of 10 micrometers. This is achieved by four micro-screws attached to the support that is fixed on a detector flange. Each of the four micro-screws move the perpendicular support plane fixed to the detector forward and

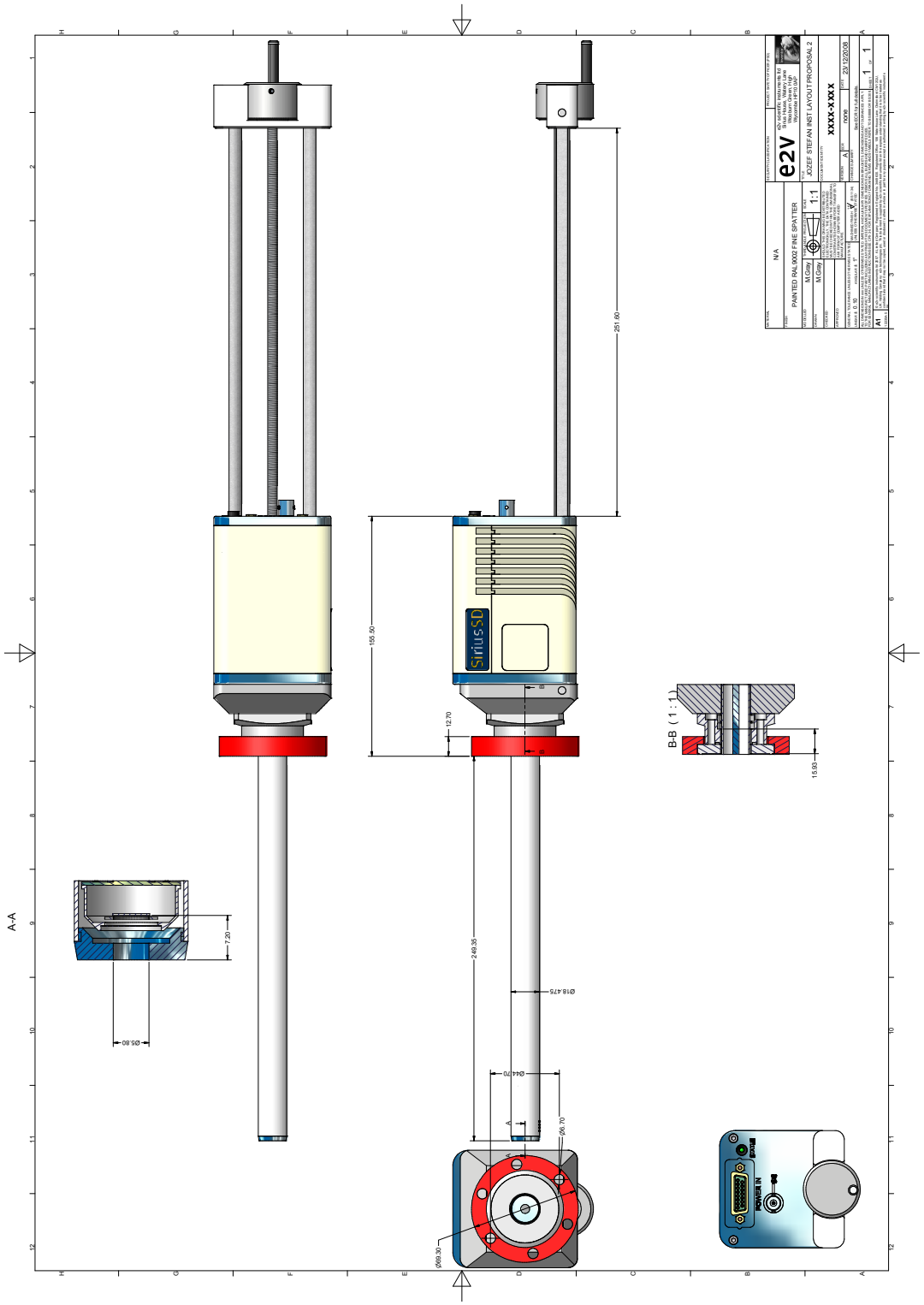

Figure 2.4: A layout of the new silicon-drift detector used in the CF PIXE set-up (technical drawing of e-2v company [59]).

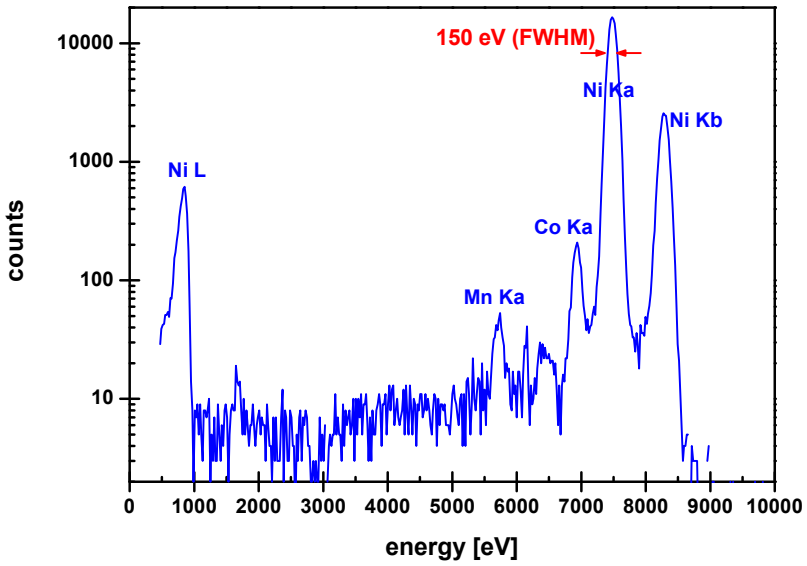

Figure 2.5: PIXE spectrum from 1 μm thin nickel foil measured with SDD detector with 7.5 μm kapton foil and 2 μm Al foil used as absorbers. The detector was approximately 5 cm away from the target. Other parameters were set as in the standard μ-PIXE mode (1.5 μm wide proton beam, 100 pA current etc.). Ni K_α, K_β and L line are visible. The width at half maximum of Ni K_α line at 7.48 keV is 150 eV.

rearward along the detector axis (refer to Figure 2.6 and 2.7 for better description). In this way, very precise movements of the detector snout in all four directions can be achieved. The mechanical stress during the alignment is relieved by a vacuum bellow.

The detector snout with the lens attached is retractable and can be kept in a vacuum when the experimental chamber is vented.

The X-ray lens is mounted on the snout of the detector. A special lens holder and the absorber support was designed for this purpose. As we will see further on, each of the tested lenses has different physical size. The lens holder is hosting a threaded aperture, which fits to any of the three lenses tested. The holder has a cylindrical shape with a side screw to tighten it to the detector's snout. It is designed in order to allow for a simple lens mounting and unmounting as well to enable venting of the experimental chamber without air pressure stress to the delicate window of the detector. The lens holder is shown in Figures 2.8 and 2.9. The detailed construction of the polycapillary frame and holder is unavailable for publication due to the request of the manufacturer.

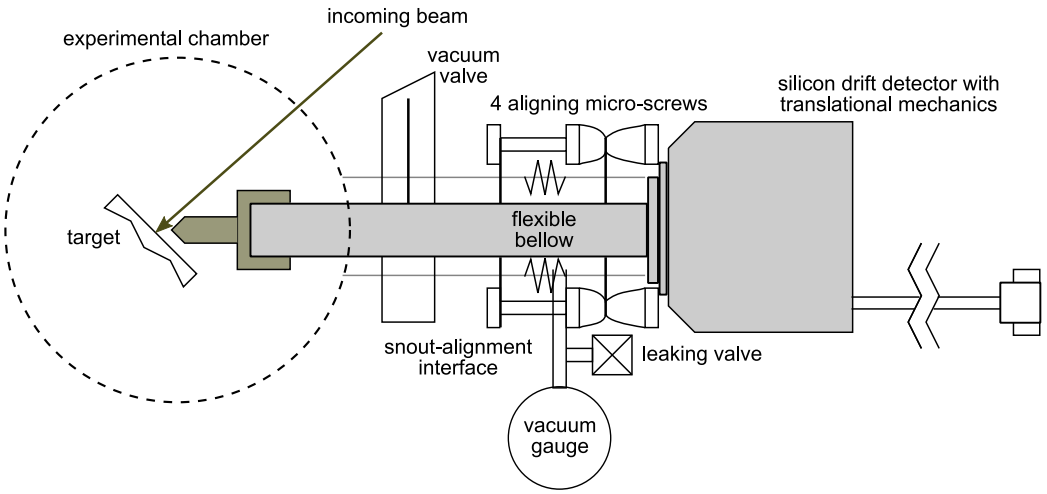

Figure 2.6: Scheme of the new confocal set-up at JSI. It is composed of a silicon drift detector, an X-ray lens, a snout-alignment interface and a load-lock system.

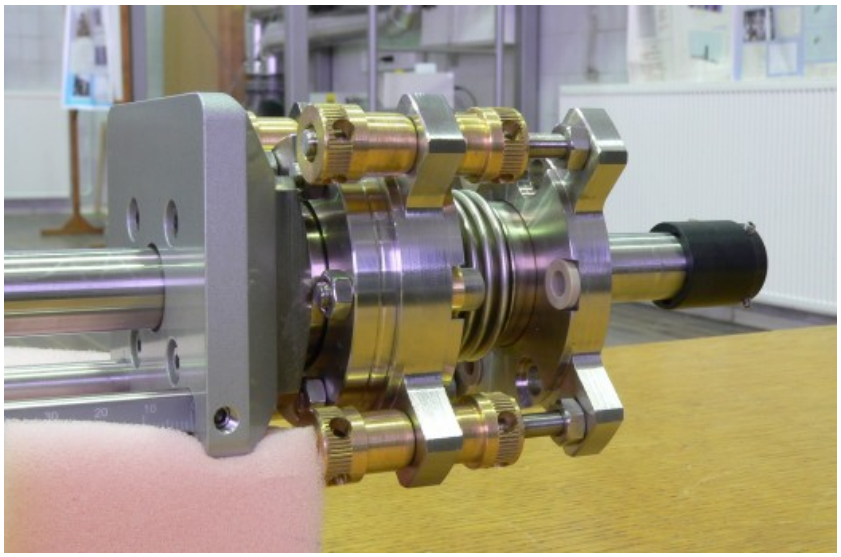

Figure 2.7: Photograph of a mechanical interface for CF PIXE supporting SDD detector. A snout-alignment interface with four micro-screws, bellow and the detector's snout is visible.

Tested lenses

The description of the lens proprieties and their characterization is described later on, however as the optics attached to the detector is the crucial part of the set-up, the three tested lenses and their specified properties are listed below.

There are three major producers of polycapillary X-ray lenses, LENP, China [60], XOS, USA [61] and IfG, Germany [62]. We were unable to establish a contact with the first producer and due to the results published in [63], where properties of several lenses from different producers were examined, the contacts with XOS and IfG were established. Since the depth resolution of CF PIXE is dominantly determined by the size of the lens acceptance volume, we were looking for a lens with the smallest possible transverse FWHM and long enough focal distance to set up the confocal geometry. XOS was unable to fulfill some of the requests, therefore the intensive discussions with IfG engineers followed. Due to the special application of the optics, three different lenses were produced at IFG for testing and for the potential use in our confocal PIXE set-up: the polycapillary half-lens 58mkl14 (lens A) was followed by the polycapillary conic collimator CN01_PCCC (polyCCC), and after consideration of previous results and in the framework of the existing lens-production technology, the polycapillary semi-lens 119mmkl03 (lens B) was delivered a year later (Figures 2.8 and 2.9). Specified properties of all three lenses are described below. The resume of specified technical characteristics provided by the manufacturer for the three X-ray optical elements tested at confocal PIXE setup is given in tables 2.1 and 2.2. The description of physical dimensions is presented at Figure 2.10.

Of the two semi-lenses, lens B features a smaller acceptance aperture of 1.2 mm and smaller focal distance of 3.5 mm with respect to lens A (1.75 mm and 4.9 mm). This leads to a smaller FWHM of the focal spot for lens B. The manufacturer measured the focal spot size in the focusing mode using a 50 μm Mo X-ray source. The source was positioned at the larger aperture of the lens (where the capillaries are parallel), and a 5 μm pinhole was translated through the focal plane on the opposite side of the lens. The resulting FWHM for lens A was 23 - 24 μm for X-rays in the 5-10 keV energy range. At energies above 20 keV, the reported focal size was 13 μm. The FWHM values for lens B were 13 μm for the X-ray energies between 5 and 10 keV and 9 μm above 15 keV. The lens intensity gain was defined by the manufacturer as the ratio of the X-ray intensity passing through a 5 μm pinhole placed at the lens focus with and without the lens installed. The reported values were 460 and 1050 for lens A and B, respectively, at the energy interval from 7.5 - 10 keV.

The polyCCC is a monolithic polycapillary cone designed to collect the X-ray radiation from samples irradiated by a broad primary beam [64]. The polyCCC characterized here is 2.5 mm long, with a focal distance of 1.45 mm. The manufacturer determined the FWHM of the focal volume by moving a 10 μm stripe through the focal plane and reported a value of 20 μm.

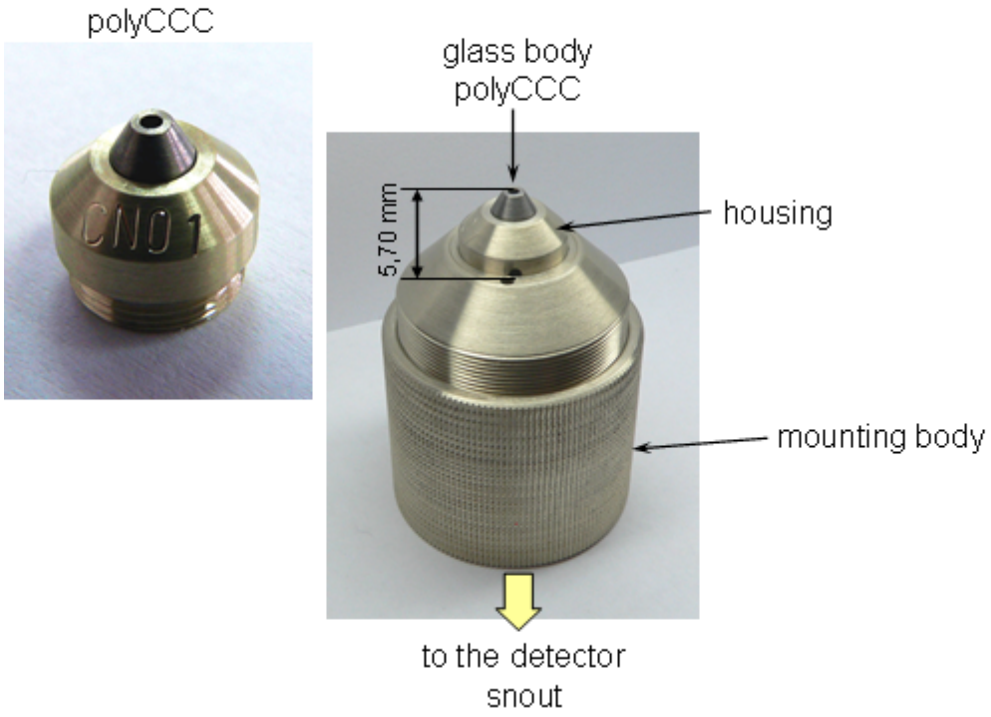

Figure 2.8: Photograph of the polycapillary conic collimator (left) and the polyCCC mounted at the lens holder (right).

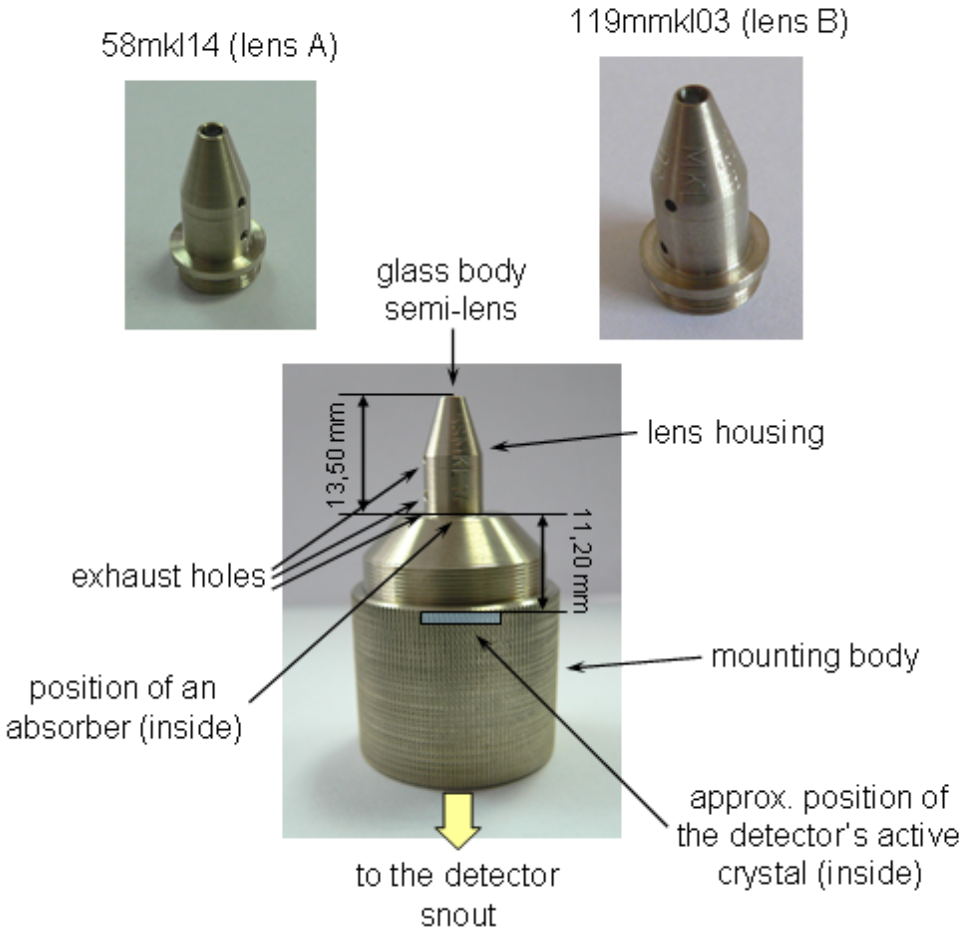

Figure 2.9: Photograph of lenses A and B (up). Bellow is the photo of the lens mounting body and holder.

2.3 Polycapillary X-ray lens

The theory of the interaction of X-rays with matter and on the total external reflections in the capillary optics is described elsewhere [65–67]. In this chapter, we briefly introduce the main concepts that are relevant to understand the lens performance. We identify and analyze lens properties that are important for the CF PIXE method and later on, elaborate on a method for lens characterization.

2.3.1 Principles

X-rays occupy electromagnetic spectrum in the wavelength region between 0.01 and 10 nm corresponding to energies in the range from a few to several hundreds keV. The index of refraction of all materials for X-rays is slightly less than in-vacuum value[1] of 1 and this fact determines behaviour of X-rays under reflection and refraction. The total reflections of X-rays thus occurs at the borderline from vacuum (air) to matter. Due to the absorption, the index of refraction $\tilde{n}$ is in general a complex number. The real part of $\tilde{n}^2$ can be labeled as

$$\text{Re}\,(\tilde{n}^2) = 1 - \delta, \tag{2.1}$$

and δ can be associated with the angle of total reflection θ_c [66, 67].

$$\theta_c = \sqrt{\delta} \tag{2.2}$$

Due to the dispersion, θ_c is inversely proportional to the energy of guided X-rays [65, 67]. In principle, the higher the energy, the smaller the reflection angle:

$$\delta = \frac{Ne^2\lambda^2}{4\pi^2\epsilon_0 mc^2}, \tag{2.3}$$

where e stands for the elementary charge, N represents the electronic density in matter, ϵ_0 the vacuum permittivity and λ is the wavelength of the reflecting radiation that is connected with the energy by the known relation $E = \frac{hc}{\lambda}$.

The angle of total reflection for X-rays is small – typically several mrad at X-ray energies of several keV. A single reflection of an X-ray beam falling at grazing incidence

[1] example: real part of the index of refraction for Mo K_α line (17.48 keV) in quartz glass (ρ = 2.65g/cm^2) is $1 - 1.8 \cdot 10^{-6}$ [68]

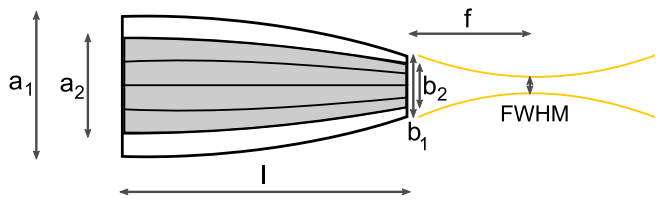

Figure 2.10: A scheme of a polycapillary X-ray lens used with its physical parameters: length (l), entrance and exit size (b_1 ,b_2 ,a_1 ,a_2), focal distance (f) and the size of the focal point (FWHM).

parameter	lens A	lens B	polyCCC
length [mm] (l)	13.1	13.5	2.5
sample-entrance (focal) distance [mm] (f)	4.9 ± 0.1	3.5 ± 0.1	1.45
entrance size (cover) [mm] (b_1)	1.75	1.4	1.2
entrance size (structure) [mm] (b_2)	1.2	0.97	
exit size (cover) [mm] (a_1)	3.42	3.45	2.5
exit size (structure) [mm] (a_2)	2	2.85	
capture angle [deg.]			37

Table 2.1: Geometrical parameters of both tested semi-lenses A and B and a polyCCC as specified by the manufacturer.

energy [keV]	3-5	5-7.5	7.5-10	10-15	15-20	20-25	25-30
FWHM (lens A) [μm]	23	24	23	19	14	13	13
FWHM (lens B) [μm]	12	13	13	12	9	9	9
FWHM (polyCCC) [μm]		20					
intensity gain (lens A)	43	451	458	430	312	113	20
intensity gain (lens B)	228	1090	1048	968	696	238	37

Table 2.2: Parameters for tested lenses as specified by the manufacturer. The FWHM of the focal size was determined by using a 50 μm Mo source and scanning over by 5 μm pinhole. Intensity gain was defined as the intensity measured through 5 μm pinhole at lens focus divided by the intensity of direct beam through 5 μm pinhole with the lens working in the focusing mode. The spacial resolution of polyCCC was obtained by a cross-scanning of the focal plane with a 10 μm metallic stripe.

onto a smooth surface changes its propagation direction. This change is very small because it does not exceed $2\theta_c$. The main idea of the capillary optics is to use multiple reflection of X-ray beams on specially curved surfaces [65]. As a result of N subsequent reflections, a beam can be reflected to a relatively large angle of the order of $2N\theta_c$. Unfortunately, due to the absorption, the number of reflections N can not be arbitrarily large, but is preferably maintained below 20 or 30 [65]. When using a bunch of hollow bent capillaries as in the case of an X-ray polycapillary lens, an X-ray deflection angle can exceed several degrees. It is easy to imagine that such systems can be applied for collecting, guiding and focusing X-ray radiation.

A typical X-ray lens contains a large number of specially arranged individual capillaries. The entrance side of the channels is directed toward an X-ray source that can be either a point-like (Figure 2.11 b,c) or a parallel beam (Figure 2.11 a), while the exit part of capillaries can be either directed toward the exit focal point or set into mutually parallel set. In the point-to-point case, divergent radiation from the source is captured and concentrated on a small spot at the exit. This is known as a polycapillary "full lens" or "lens" only. The other lens type, a so-called "semi-" or "half-lens" is used either to focus (2.11 b) or collimate (2.11 c) the light. In the first case, a half-lens accepts a parallel beam and concentrate it in the focal point (focusing mode), while in the second case a divergent beam from the source is transformed into a quasiparallel one (collecting mode).

Both types, full- and half-lenses, are nowadays widely used. Full-lenses were the first to be intensively studied and characterized, as this type was used to capture and focus the radiation from an X-ray source. The availability of intense beams of monochromatic X-ray radiation from synchrotron light sources has induced an interest in confocal spectroscopies and half-lenses are gaining in importance. Dependent on the type and even on the mode used, definitions of lens characteristics may vary. In the case of a half-lens, data on the focusing proprieties determined by different methods in the focusing mode could not be accurately applied to the collecting mode, as the differences can be significant [69]. Therefore, careful inspection of lens properties and characterization of each individual lens is of high importance.

2.3.2 Properties

Several properties of polycapillary X-ray lenses (PCXRL) and half-lenses (PCXRHL) are of interest. These include, among others, the intensity distribution of the transmit-

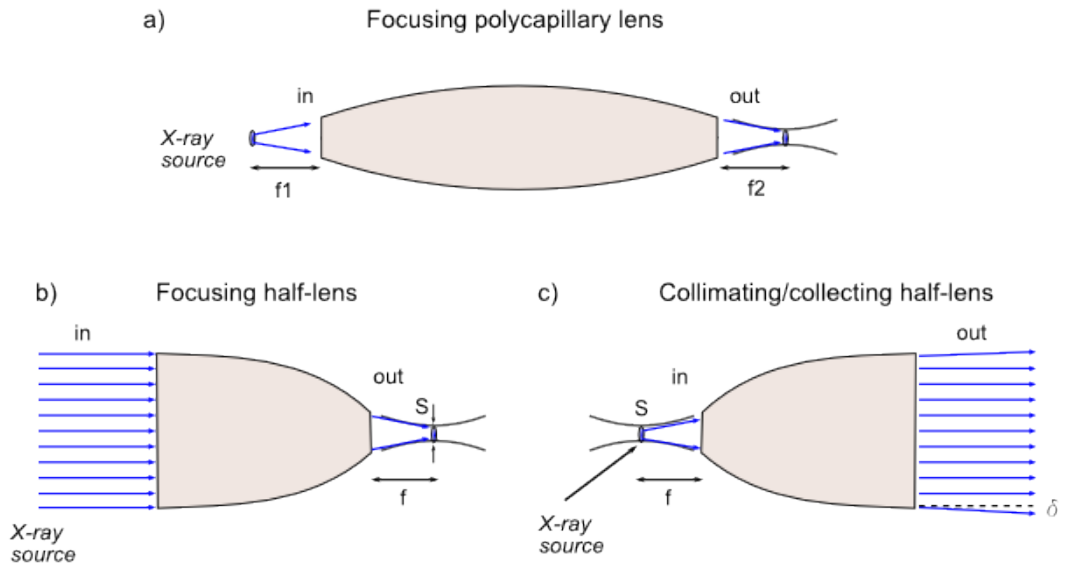

Figure 2.11: Two types of polycapillary X-ray optics, a standard polycapillary full lens (a) and a half-lens in focusing (b) and in collecting mode (c). Focal distance(s), the lateral beam profile in the focal point and the divergence are shown.

ted X-ray flux, the focal point size and its dependence on the X-ray energy, the shape of the acceptance volume, focal distance, the X-ray intensity gain and other effects, such as a "halo" effect or the background increase in the X-ray spectra.

The main property that dominantly influences the ability of the method, is the shape of the acceptance (if working in collecting) or transmission (if working in focusing mode) volume. The intensity profile of the envelope of the collected/transmitted rays in plane perpendicular to lens axis can be described reasonably well with an axially symmetric Gaussian function. Detailed analysis shows minor discrepancies from a single Gaussian curve, however it presents a good approximation for the experimental conditions that apply for a standard confocal PIXE measurements [48]. The "spot" size is most commonly described by full width at half maximum (FWHM), however some other definitions (full width at tenth maximum, sigma) are sometimes used. The lens FWHM is changing along the lens axis. The envelope of the incoming (or outcoming) rays near the focal point has a shape of a paraboloid [50]. At certain distance from the tip of the lens it reaches its minimum and the corresponding point on the axis is defined as a lens focal point and the distance from the lens as a focal length. In addition, FWHM depends on photon energies transmitted by the lens due to the dependence of the angle of total reflection on the energy of X-rays (Equation (2.3)). On the other hand, the focal distance remains more or less fixed for different X-ray energies.

The intensity gain and the transmission efficiency are two parameters that are often used to describe polycapillary lens. For a standard full lens that acts as an X-ray concentrator, gain is reasonably defined as an intensity increase in the focal spot of the lens relative to the intensity of the direct beam passing though the fixed pinhole [36, 70]. The intensity of a point-like X-ray source falls with the square of the distance to the source. The full X-ray lens transfers the X-ray intensity from the source to another position with a much smaller loss compared to the loss of the solid angle when the radiation is freely propagating in space, even when photon absorption losses in the lens are taken into account. The full-lens gain defined in this way is in the range from a few tenths to several thousands [71–73].

For half-lenses in the focusing mode, the gain may be defined in a similar way, as the lens in this mode also acts as an X-ray concentrator. However, for a PCXRHL working in the collecting mode, which is of a main interest here, such gain definition is of limited use. Mounting the lens in front of the detector necessarily results in an increased working distance of the X-ray detector, in this way diminishing the detector acceptance solid angle. The application of the lens in the collecting mode necessarily results in an intensity reduction and the "gain" as defined above is below 1.

The transmission efficiency is used instead to quantitatively describe X-ray transmission through the lens in the collecting working mode. For a point-like X-ray source the transmission T is defined as the ratio of the X-ray intensity transmitted through the lens to the X-ray intensity arriving at the lens entrance [74]. T then equals the ratio of the X-ray intensity I_{lens} detected with the half-lens versus the X-ray intensity I_{pin} detected without the half-lens but with the pinhole inserted in front of the detector:

$$T = \frac{I_{lens}}{I_{pin}} \frac{\Omega_{pin}}{\Omega_{lens}}. \tag{2.4}$$

To obtain T for a given source position the intensity ratio I_{lens}/I_{pin} (normalized to the same dose) must be corrected by the ratio of the pinhole solid angle Ω_{pin} versus the lens acceptance solid angle Ω_{lens}.

Since the Kumakhov report on early design of the polycapillary X-ray lens in 1990 [65], a comprehensive number of papers were published dealing with characterization of the physical properties of these X-ray lenses. The properties of a PCXRL, that focuses the radiation from a diverging X-ray source (X-ray tube) onto the target, were intensively studied by different groups, mostly in collaboration with the three lens manufacturers. A review article about the status of polycapillary X-ray optics at that time,

the types and application of the lenses together with some properties were described by Kumakhov in 2000 [75]. Wang et al. developed a geometrical optics simulation program and compared the results with the measurements, mostly in the hard X-ray range from 10 up to 80 keV. Focal sizes and the behaviour of transmitted rays at different energies and at different distances from the end of the lens and the transmission efficiency were investigated [76]. Gomley et al. reported a detailed characterization of one particular lens and described the discrepancies found between the measured and calculated values [71]. In 2003 Gao and Ponomarev continued the discussion by describing the status of manufacturing PCXRL and the means of their characterization [77]. Standard properties like the focal spot size at different energies were presented, but also the divergence effect, transmission efficiency and intensity gain. Discussed were also the effects of different technological solutions and/or characterization techniques on the lens measured performance. Haschke and Haller examined several different PCXRL from three major lens producers and showed how the manufacturing procedure and the control over capillary shape or geometric parameters influence the lens properties [63]. They did not focus only on the intensity gain and on the spot sizes but also on other parameters, such as the energy dependence of the spot size and of the transmission efficiency. Their influence to the measured transmitted spectrum is studied as well. The main goal was to characterize the lenses used in different versions of micro-XRF spectroscopies.

On the other side of the world, Sun and Ding from LENP [60] published a series of papers dealing with the characterization of full lenses, from the focal spot size, output focal distance to the transmission efficiency and "halo effect" [74, 78, 79]. Both, the focal size and the transmission efficiency were found to be energy dependent as already reported, however even the change of the lens focal distance with energy was detected that amounted to several tens of micrometers in the energy range from 7 to 15 keV. Europe did not stay behind, as several PCXRL characterization of lenses produced by IFG were reported [73, 80, 81]. Several theoretical approaches were also presented and ray tracing simulation is now accepted as a method of choice for estimating or designing the properties of X-ray lenses [82, 83].

Most of the presented articles are dealing with full lenses. Half-lenses are usually used in the focusing mode and are applied in micro-XRF set-ups for focusing the incoming quasi-parallel X-ray beams onto the sample. Characterization is performed for each individual lens and many application were reported [43, 70, 72, 73]. The focusing properties of the half-lenses are usually determined by the knife-edge method, where an object with a sharp edge, either a thin mesh or a small pinhole, is translated perpen-

dicularly to the beam direction and the transmitted X-rays are detected at each object's position in front of the lens.

In the collecting mode, X-rays from a (point) source or from a confined area of the sample are collected and collimated before impinging on the sensitive area of an X-ray detector. The manufacturers usually test the half-lenses in the focusing working mode. However, due to the different physical conditions present in the collecting mode, data on the focusing properties determined by the knife-edge or pinhole method could not be directly applied to the collecting mode, as the differences can be significant [69]. The characterization of half-lenses to be used in the collecting mode should ideally be made in the collecting working condition of the lens. The most convenient way to perform such characterization is to explore the lens transmission for X-rays that are emitted from a movable micrometre-sized source, created by the intersection of a charged particle beam with a thin metal foil. For that purpose either focused electron beams or proton beams were found suitable. The former approach may be realized by an electron microscope set-up equipped with an energy dispersive X-ray spectrometer [69, 84] and the latter is provided by the proton μ-probe [50, 69, 85, 86]. A half-lens characterization in the collecting mode by a pre-focused photon beam was also reported [87].

The polycapilary conic collimator is much more rarely used device and therefore much less work on the characterization of polyCCC was reported. Since the first description in 1998 [64], reporting the focal size, focal distance and resolution achieved with polyCCC, only a few papers dealing with the properties of polyCCC were published [88, 89].

2.3.3 Characterization

We want to explore in detail the effect of a half-lens placed between the source and the X-ray detector when X-ray radiation is generated by a microprobe. The rest of this chapter reports on the characterization of two types of polycapillary X-ray lenses and of a polycapillary conic collimator, manufactured and delivered by IFG, to be used at a new confocal PIXE set-up.

Based on the results of earlier experiments, the lens transmission function could be described by

$$T\left(\vec{r}'', E\right) = T_0(E) \exp\left[-\frac{(x'')^2 + (y'')^2}{2\sigma^2\left(z'', E\right)}\right]. \tag{2.5}$$

The transmission depends on the X-ray energy E and on the X-ray source position ($\vec{r}''$). In Eq. (2.5) the position is entered in the detector coordinate system S'' (discussed in detail in Section 2.4). The standard deviation σ measures the transverse width of the source volume transmitted by the lens and is related to the FWHM as $2\sigma\sqrt{2\ln 2}$. In general, σ is dependent on the position z'' of the transverse plane along the lens axis and on the X-ray energy. $T_0(E)$ is the maximum transmission of the lens, applying to an X-ray source with energy E, positioned exactly at the lens focal point.

The lenses were tested in the collecting mode with a 3 MeV proton micro-beam having a cross sectional diameter of about 1.5 μm. Passing the target, the protons ionized atoms that relaxed by X-ray emission. If the targets were thin, a well localized X-ray source was created that has a weak continuous (bremsstrahlung) spectral component. The source's shape was elongated along the path of the proton beam in the sample, when thicker samples were used. Although the proton beam significantly spreads out at the end of the range [90], the X-ray production cross section is negligible at low energies and the effective X-ray source could be regarded as of cylindrical shape. The cylinder diameter could be taken to match the proton beam diameter and its effective length calculated from the proton stopping power, the energy dependence of the ionization cross-section and the absorption cross section of the sample for the observed X-ray radiation. Typically, for 3 MeV protons and thick targets, the length of the cylinder was a few tens of micrometres in low-Z materials and decreased to about ten micrometres for mid-Z metals. By choosing an appropriate set of samples, including thin metallic foils, lens properties over a wide range of X-ray energies could be investigated

All three X-ray optical devices were separately mounted in front of the snout of a thin-window silicon-drifted (SDD) X-ray detector, protected by a 6 μm mylar foil coated with 100 nm of Al. After the lens installation, the vacuum chamber was evacuated at a rate that was below 1 mbar/s to avoid detector window rupture. A two-step alignment procedure followed, consisting of an optical alignment with a phantom, followed by a precise alignment with the proton beam scanning over a 2×2 millimetre area of a 1 μm thick nickel foil. The detailed alignment procedure is described in the following page (page 50).

The surface of monoelemental reference targets was scanned with the 3 MeV focused proton beam and in each position the emitted X-ray spectrum was recorded. Only photons from a limited target volume were transmitted through the lens (refer to Fig. 2.13a on page 52). The X-ray intensity at each target point changed due to the variable transmission of the lens, governed by Eq. (2.5). By fitting a functional form to the

measured signal for different targets and different target positions, we could extract the FWHM of the lens acceptance volume for a given X-ray energy and a given distance from the focal point. The position of the focal point was defined as the position with the minimum value of FWHM.

We measured the lens transmission using different thin sample foils, positioned in the focal plane of the lens. The detector was first equipped with the X-ray half-lens, and second with a corresponding pinhole collimator as required in Eq. (2.4). Two types of measurements were made – a standard one in the beam scanning mode and one where transmission was measured with the proton beam parked in the centre of the focal volume and the target positioned in the focal plane. Both measurements yielded similar results, as will be discussed below. From these measurements the dependence of the T_0 on the energy was determined for lens B.

Some additional lens properties were studied as well, such as the effect of the half-lens on the background in the measured X-ray spectra. This is an important aspect, as any increase of background deteriorates the elemental sensitivity of PIXE. The "halo" effect that many authors observed and affects the lens performance for high energies was also checked. Some other characteristics of the lenses such as the total transmission or the intensity asymmetry in the observed maps are also reported.

Alignment procedure

To achieve the best resolution it is essential to align the focal region of the proton beam with the lens focus. In this way, we can ensure the smallest possible probing volume and achieve its translation through the sample by a mechanical movement of the sample or by beam scanning.

In the alignment procedure we create a confocal set-up and bring together the probing volume obtained and the target. The reference plane in the experimental chamber is determined by the field of view of the optical microscope. The proton beam is first focused by minimizing the beam size at the scintillator screen by minute changes of the two currents applied to the magnetic lens. In the second step, beam size is additionally minimized by scanning the beam over micrometer size meshes. During the beam-size optimization, the scintillator screen and the reference meshes are positioned in the focal plane of the optical microscope. The undeflected proton beam direction defines the reference point in the reference plane. To position the lens to view the reference point, we first align the detector direction with a lens mock-up mounted on its snout.

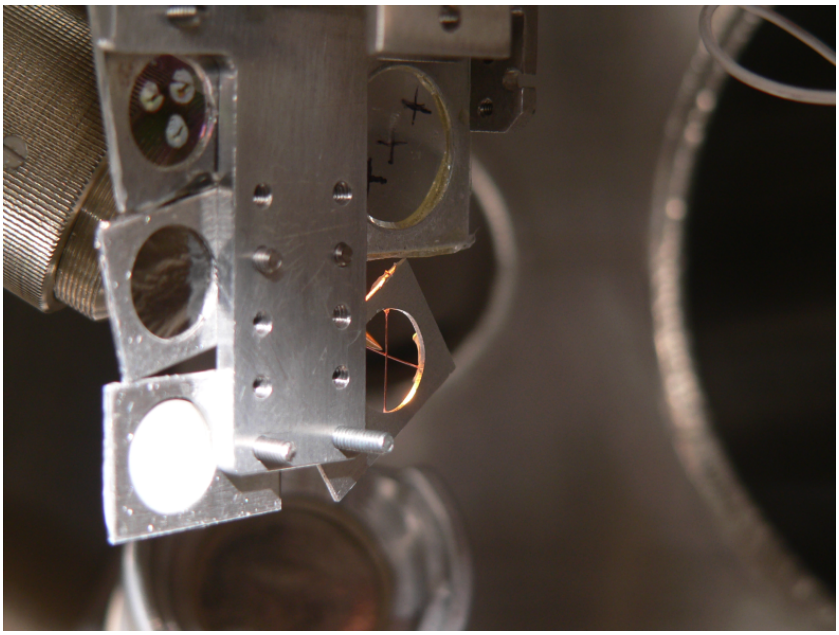

Figure 2.12: The interior of the experimental chamber, with the lens mock-up at the end of the detector snout and a target on the target holder with the cross used at the first step of the alignment procedure.

The lens mock-up has the same dimensions as the semi-lens, including a pointing tip which marks the focal point of the lens. This tip is brought to a marked area at the target, which is positioned in the focal plane of the optical microscope. The design of the lens mock-up and the photograph of this procedure is shown in Figure 2.12. Since the axis is oriented in the same way as the lens axis, we can achieve alignment with a precision of a few hundreds of micrometers. The alignment interface of the new system is of crucial importance here, since the whole detector can be easily moved by precise steps.

In the next step, the real lens is mounted on the X-ray detector. When the high vacuum is achieved, we continue with the alignment of the confocal system with the proton beam turned on. Thin monoelemental foil is positioned in the focal plane of the microscope and scanned by the beam over a square-shaped region. The positioning include controlled shifts by the alignment interface in the direction perpendicular to the detector axis as well as shifts along the detector axis by the translational mechanics. The detector's snout must be iteratively positioned in order to obtain the smallest possible FWHM of the signal area that is positioned at the center of the map. An example of X-ray map of the Ni K_α line emitted from the 1 μm thick Ni foil is presented in Figure 2.13a. The obtained curve of FWHM measured at different positions from the focal

point looks similar to the one in Figure 2.17. When its minimized size coincides with the focal plane of the optical microscope, the confocal set-up is aligned.

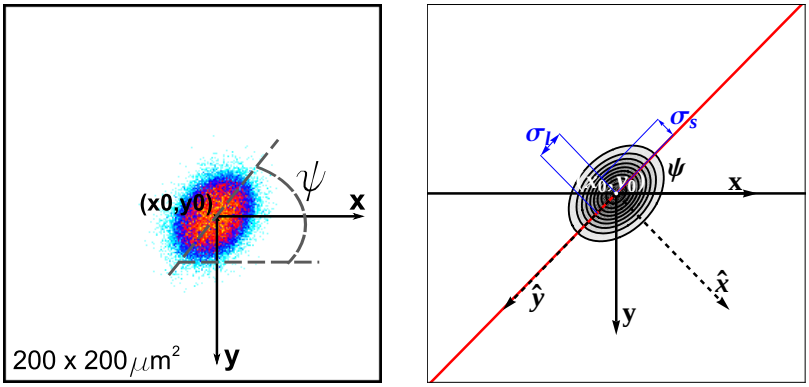

(a) Measurement (b) Calculation

Figure 2.13: a) Map of Ni K_α X-rays with energy 7.48 keV measured from a 1 μm thick nickel foil with the lens B near the lens focus. As the lens intensity profile has a 2D Gaussian shape and due to the geometrical conditions, its projection on the (x,y) plane is ellipsoidal. Analysis of this map gives $\sigma_s = (10 \pm 0.5)$ μm, $\sigma_l = (14.1 \pm 0.5)$ μm and $\psi = 50° \pm 3°$.
b) Calculated map of a thin foil in the confocal position: $z_0 = 0$, $\alpha = 0$, $\varphi = 35°$, $\theta = 30.3°$. The centre of the ellipse is at (0,0) as calculated, σ is taken to be 9.6 μm, which is the minimum that we found from the measurements of Ni foil. The size of both frames is 200×200 μm^2.

2.4 Geometry

The geometry of the JSI confocal set-up was partially discussed in at the beginning of this chapter and is presented in more detail in Fig. 2.14. The angle between the detector and the proton beam axis is 135°. The surface of the target is scanned by a microbeam. Due to the "skewed" geometry the accumulated intensity profile in general exhibits the form of an asymmetric 2D Gaussian distribution (Fig. 2.13a). To extract the size and shape of the lens acceptance volume from the shape of the measured distribution, we explored the influence of the experimental geometry on the dimensions of the observed spot.

The acquisition set-up writes the data acquired in the proton beam coordinate system S, where the point coordinates are given by (x, y, z). In the case of target rotation out of the perpendicular xy plane, the location of the irradiated spots with respect to the target reference does not coincide with the coordinates of the acquisition system and therefore we introduce the target coordinate system S' with a set of coordinates (x', y', z'). As already mentioned, we also employ the lens coordinate system S'' with its z-axis

aligned along the lens (detector) axis with corresponding coordinates (x'', y'', z'') (Fig. 2.14).

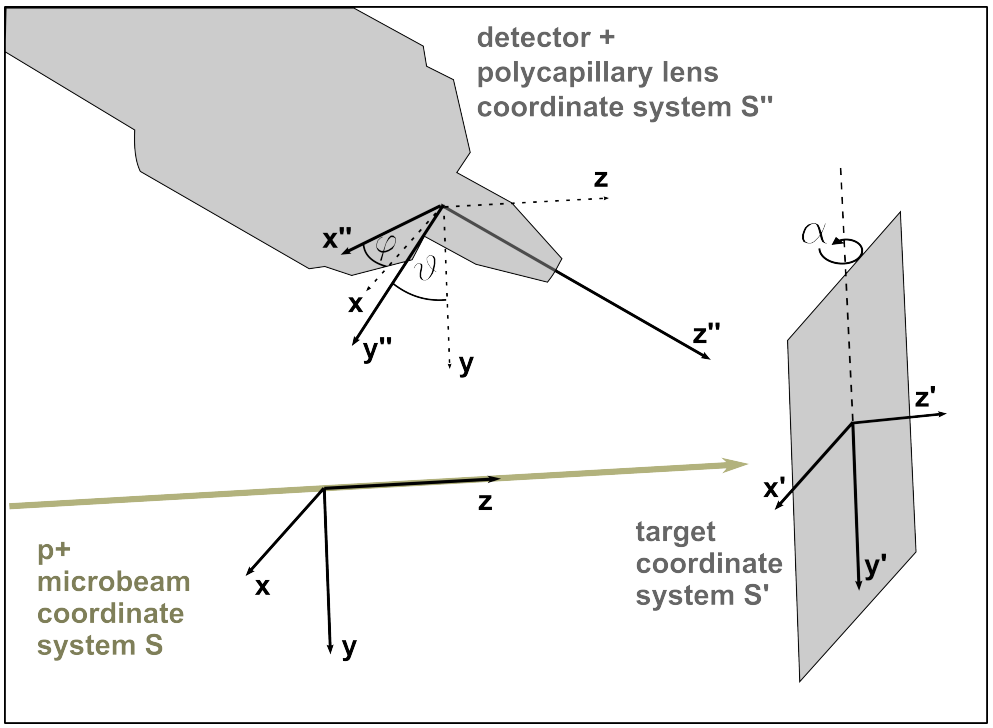

Figure 2.14: Geometrical conditions in the μ-PIXE chamber prepared for the confocal set-up. Three coordinate systems are shown: $S(x, y, z)$) – the system of microbeam that describes the measured maps, $S'(x', y', z')$ – the system bind to the target and S'' – the system that describes the detector and the lens position in space.

The microbeam position varies during the measurements and is given by coordinates (x,y). In the confocal set-up, the focal points of the microbeam ($z = 0$) and of the polycapillary lens ($z'' = 0$) coincide. For measurements we may employ target rotation around the vertical axis (y) for an angle α and translation out of the confocal position for a distance z_0 along the microbeam axis z. When $\alpha = 0$ and $z_0 = 0$, the coordinate systems S and S' coincide. The coordinates of the system S are readily expressed in S' as:

$$\begin{bmatrix} x \\ y \\ z \end{bmatrix} = \begin{bmatrix} \cos\alpha & 0 & -\sin\alpha \\ 0 & 1 & 0 \\ \sin\alpha & 0 & \cos\alpha \end{bmatrix} \begin{bmatrix} x' \\ y' \\ z' \end{bmatrix} + \begin{bmatrix} 0 \\ 0 \\ z_0 \end{bmatrix}. \tag{2.6}$$

The third coordinate system S'' is the reference frame of the detector. S'' is obtained by first rotating S around the y axis by an angle φ and then the intermediate coordinate system $\tilde{S}$ is rotated along $\tilde{x}$ axis by an angle ϑ clockwise. The transformation into the

system S'' can be represented by the product of two rotational matrices:

$$\begin{bmatrix} x'' \\ y'' \\ z'' \end{bmatrix} = \begin{bmatrix} 1 & 0 & 0 \\ 0 & \cos\vartheta & -\sin\vartheta \\ 0 & \sin\vartheta & \cos\vartheta \end{bmatrix} \begin{bmatrix} \cos\varphi & 0 & \sin\varphi \\ 0 & 1 & 0 \\ -\sin\varphi & 0 & \cos\varphi \end{bmatrix} \begin{bmatrix} x \\ y \\ z \end{bmatrix}. \tag{2.7}$$

It is assumed that σ changes only along the lens axis ($\sigma = \sigma(z'')$), but this dependence is usually weak near the focal point and is neglected for now. If thin foils are used, we can safely neglect the source thickness, so that $z' = 0$, and the irradiated point is represented by the S-coordinate: $(x, y, x\tan\alpha + z_0)$. The transmission of points through the lens is given by Eq. (2.5) and is therefore described as:

$$T(x', y', z') = T(x, y, x\tan\alpha + z_0) = T_0 \exp\left[-\frac{Q(x,y)}{2\sigma^2}\right], \tag{2.8}$$

where the expression in the numerator of the exponent can be arranged into the quadratic form:

$$\begin{aligned} Q(x,y) &= (x\cos\varphi + \sin\varphi(z_0 + x\tan\alpha))^2 + (y\cos\vartheta + x\sin\varphi\sin\vartheta - \cos\varphi\sin\vartheta(z_0 + x\tan\alpha))^2, \\ &\equiv A_1x^2 + 2A_2xy + A_3y^2 + 2A_4x + 2A_5y + A_6. \end{aligned} \tag{2.9}$$

The coefficients A_i are known functions of angles α, ϑ and φ and of the foil displacement z_0:

$$\begin{aligned} A_1 &= \cos^2\varphi + \sin^2\varphi\sin^2\vartheta + 2\cos\varphi\sin\varphi\tan\alpha - 2\cos\varphi\sin\varphi\sin^2\vartheta\tan\alpha + \\ &+ \sin^2\varphi\tan^2\alpha + \cos^2\varphi\sin^2\vartheta\tan^2\alpha, \\ A_2 &= \cos\vartheta\sin\varphi\sin\vartheta - \cos\varphi\cos\vartheta\sin\vartheta\tan\alpha, \\ A_3 &= \cos^2\vartheta, \\ A_4 &= z_0(\cos\varphi\sin\varphi - \cos\varphi\sin\varphi\sin^2\vartheta + \sin^2\varphi\tan\alpha + \cos^2\varphi\sin^2\vartheta\tan\alpha, \\ A_5 &= -z_0\cos\varphi\cos\vartheta\sin\vartheta, \\ A_6 &= z_0^2(\sin^2\varphi + \cos^2\varphi\sin^2\vartheta. \end{aligned} \tag{2.10}$$

The quadratic form (2.9) is a general description of a rotated and displaced ellipse. The 2D transmission spot in the X-ray map therefore assumes the form of an exponentially

attenuated (Gaussian) elliptical profile. The form can be written also as:

$$Q(x,y) = a(x-x_0)^2 + 2b(x-x_0)(y-y_0) + c(y-y_0)^2. \tag{2.11}$$

Coefficients a, b and c, can be directly associated to A_1, A_2 and A_3, while x_0 and y_0 represents the position of the center of the spot. This and the orientation of the elliptically elongated spot, as well as the two dispersions along the two main axes can be calculated if A_i are known. The centre point coordinates are proportional to the displacement z_0:

$$\begin{aligned} x_0 &= \frac{A_4A_3 - A_5A_2}{A_2^2 - A_1A_3} = -z_0\frac{\cos\alpha\sin\varphi}{\cos(\alpha-\varphi)}, \\ y_0 &= \frac{A_4A_2 - A_5A_1}{-A_2^2 + A_1A_3} = z_0\frac{\cos\alpha\tan\vartheta}{\cos(\alpha-\varphi)}. \end{aligned} \tag{2.12}$$

In the confocal position ($z_0 = 0$), the ellipse lies in the centre of the coordinate frame. By moving the target backwards and forwards, the centre travels along a line that can be described by the equation $y = kx$, where the inclination k equals

$$k = \frac{y_0}{x_0} = -\frac{\tan\vartheta}{\sin\varphi}. \tag{2.13}$$

Equation (2.12) also shows that for the angle $\vartheta = 0$, when the detector lies in the horizontal plane, the centre travels along the x-axis, which is consistent with our previous calculations [50].

Both dispersions from the accumulated map, shorter σ_s and longer σ_l, are elongated due to geometrical effects. An additional rotation of the beam coordinate system S around the z-axis is required to calculate the elongation. We give such rotated coordinate system label $\hat{S}$, with coordinates $(\hat{x},\hat{y},\hat{z})$, where $\hat{z} = z$. The ellipse tilt angle ψ is given by

$$\psi = \frac{1}{2}\left(\arctan\frac{2A_2}{A_1 - A_3}\right). \tag{2.14}$$

Now both σ's measured along the direction of the large (σ_l) and the small (σ_s) axis of the ellipse in the measured map can be expressed by the original σ of the polycapillary

lens in the following way:

$$\sigma_s = \frac{\sigma}{\sqrt{A_1 \cos^2\psi + A_2 \sin 2\psi + A_3 \sin^2\psi}}, \tag{2.15}$$

$$\sigma_l = \frac{\sigma}{\sqrt{A_1 \sin^2\psi - A_2 \sin 2\psi + A_3 \cos^2\psi}}. \tag{2.16}$$

In the present experiment, $\alpha = 0$, $\varphi = 35°$ and $\vartheta = 30.3°$. Therefore

$$\psi = 44.5°,\ k = -1.02,\ \sigma_s = \sigma \quad \text{and} \quad \sigma_l = 1.414\sigma.$$

Fig. 2.13b shows the calculated response of the detector-lens system after scanning a thin target by the microbeam. With thick targets, the shape changes slightly, since the signal does not come only from the target surface, but also from the depth. A homogeneous thick target could be considered as composed of a number of thin slices, each at slightly different positions along the beam axis. Due to proton stopping, the ionization cross-section changes in every slice, while X-ray absorption on the other hand diminishes the number of transmitted photons created deeper in the target. Every virtual layer under consideration yields a two-dimensional Gaussian, with the same orientation as the previous one, but the intensity of each is weighted with a constant that takes into account the processes that govern the photon yield. By the standard PIXE equation, discussed in detail on page 70, the photon yield is proportional to the density of the element in the layer and to the probability that a photon created in some particular layer dz survives the way toward the surface (Equation (2.17)). All other experimental parameters that contribute to the quantitative description of the photon yield are not important for now and are constant for the same target-detector combination.

$$N \propto n_{at} \int_0^R \underbrace{\sigma_i(E(z))e^{-\mu l}}_{\zeta_i} dz, \tag{2.17}$$

where N is the number of measured X-ray photons, n_{at} the lateral atomic density in the target, σ_i is the energy dependent ionization cross-section and factor $e^{-\mu l}$ describes the X-ray attenuation. Proton energy is dependent of the position where the interaction takes place and is governed by the proton stopping power [1, 90].

In order to get the contribution from different layers of the monoelemental target, only factor ζ in the equation (2.17) is relevant. From the stopping power, proton energy at different depths can be calculated and the ionization cross-section determined. This has

to be multiplied by the probability that describes the transmission of photons created at the depth z in the target. The length l those photons travel is dependent on geometry and for $\alpha = 0$, $l = \frac{z}{\cos\varphi\cos\vartheta} = 1.41z$ (Appendix A.2). For nickel K_α line the values for ζ_i are presented in Figure 2.15. If we sum the contributions from all slices, the total yield is obtained.

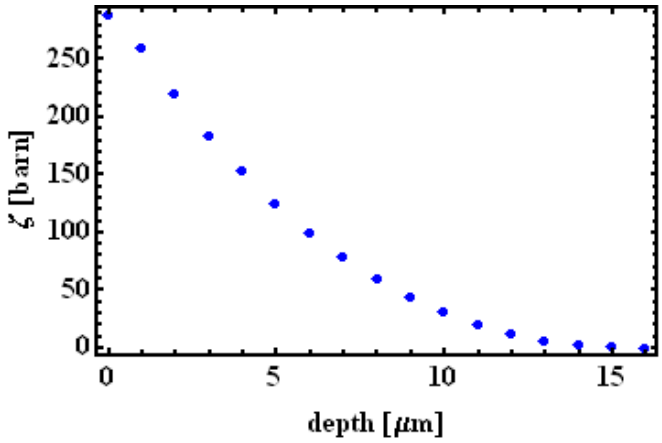

Figure 2.15: Calculated partial photon yield (ζ_i) for Ni K_α line from different slices of the thick nickel target.

The centre of the cloud moves along a line with slope ξ that can be calculated from Eq. (2.13), where $k = \tan\xi$. At the same time, the ellipse is rotated by the angle ψ (Eq. (2.14)) which depends on the set-up angles θ, φ and α. For $\alpha = 0$, Eq. (2.14) takes the form:

$$\tan 2\psi = \frac{2\cos\theta\sin\varphi\sin\theta}{\cos^2\varphi + \sin^2\varphi\sin^2\theta - \cos^2\theta}. \tag{2.18}$$

Since

$$\tan 2\psi = \frac{2\tan\psi}{1-\tan^2\psi},$$

one obtains a quadratic equation for $\tan\psi$ which has two solutions:

$$\tan\psi_1 = -\frac{\tan\theta}{\sin\varphi}, \tag{2.19}$$

$$\tan\psi_2 = \frac{\sin\varphi}{\tan\theta}. \tag{2.20}$$

The first solution is exactly the same as the expression in Eq. (2.13), while the second is valid for a $\pi/2$ larger angle. Therefore, if $\alpha = 0$, the slope of the centre movement and the inclination of the ellipse coincide ($\xi = \psi$). Thick targets lead to larger σ_l. Its value increases, due to the cumulative signal from different slices. An example for

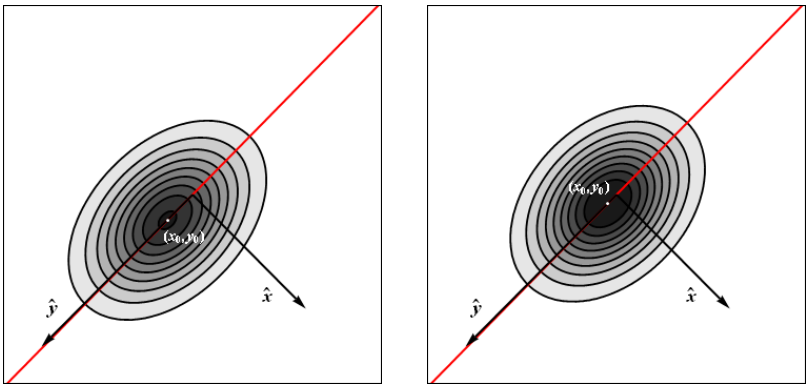

(a) (b)

Figure 2.16: a) Calculated map of a 20 μm thick nickel target in the confocal position with the target surface at the lens focal point and with $\alpha = 0$, $\varphi = 35°$, $\theta = 30.3°$ and $\sigma = 9.6$ μm. No proton stopping or X-ray absorption were considered and it was taken as every layer contributes to the total yield the same amount. The center of the spot was moved at the point (-6.65,-6.78) due to the finite thickness.
b) Calculated map of a 20 μm thick nickel target with the same parameters as in a). Beam stopping, the change in the ionization cross-section and the photon absorption was taken into account. The center of the spot lies at the point (-2.30,-2.35), therefore the resulting shift is smaller in this case. The size of both frames is 100×100 μm^2.

20 μm thick nickel target is presented in Figure 2.16.

There is another change in both "apparent" σ's; if the target is thicker then 50 - 100 μm, then the transverse change of the lens acceptance volume ($\sigma(z'')$) should be taken into account. This means that the resulting distribution originating from deeper virtual layers will be slightly larger than the distributions from the layers closer to the target surface. This effect is important only when considering heavier trace elements in a very light matrix. For thick metal samples, the effect of thickness is weak. The only effect of such targets was to enlarge the dispersion along the longer axis of the ellipse.

If $\alpha \neq 0$, ψ is also dependent on α, while ξ is not and in this case a thick target directly changes both σ values. For the purpose of our measurements we did not tilt the target holder ($\alpha = 0$).

2.5 Results of lens characterization

The tests were performed with a set of standard reference materials for PIXE or μ-PIXE method. The set includes thin monoelemental metal foils of Al, Ni, Cu, Ag and Au, with a thickness of around 1 μm, allowing measurement of a lens FWHM in a

reasonable time period ranging from a few minutes to one hour. Other samples were thin evaporated layers on nuclepore filters [91] with known areal density of selected elements (Mo, YF_3, Ge, In, GaAs). As the elemental areal densities in these samples are of the order of 50 micrograms per cm^2, the data had to be collected for several hours. The third type were bulk flat metal targets, including Ti, Cu, Naval Brass NIST 1107, Fe/Cr/Al alloy, Mo and Rh. The energy of the proton beam was 3 MeV for all measurements reported and the microbeam size was kept below 2 μm^2.

2.5.1 FWHM along the lens axis

By moving the target along the beam direction, we investigated the size of the lens acceptance volume and measured the FWHM(E_{const}, z'') dependence at the selected X-ray energy E_{const}.

For lens A, the measurements give a minimal FWHM value of around 31 μm for the Ni K_α line (7.48 keV). Fig. 2.17 demonstrates the dependence of the FWHM on the distance from the lens. We can see a strong increase of FWHM out of the focal plane and a considerable region around the focal plane with rather weak dependence on z''. For lens B, the measured FWHM of the Ni K_α line was significantly smaller at the focal point and amounted to 22.5 μm (Fig. 2.17). The difference in FWHM between the lenses A and B of approximately 30% corresponds to the difference in the focal distances and reflects the interdependence of the two properties. The dependence of FWHM(z'') obtained for lens B was again parabolic, but the dependence on the position z'' was much stronger (Fig. 2.17). As expected for a lens with a shorter focal distance, the increase in FWHM at a distance of ±200 μm from the focus was approximately twice as large for lens B as for lens A.

In our earlier work exploring another type of X-ray lens [46], we observed a negligible change of FWHM in the interval of approximately 100 μm around the focal point. This property was very convenient for application in tomography experiments. For the lenses A and B discussed here, this interval is much smaller (50 μm) and accurate alignment is required to optimally restrict the detector solid angle.

The measured FWHM of the polyCCC in the collecting mode was 25 μm for the Ni K_α line. The extremely short focal distance of 1.45 mm made work with the polyCCC extremely demanding. We also observed a non-Gaussian two-dimensional intensity distribution outside the focal point (section 2.5.3) which prevented us from parameterizing the results with Eq. (2.5).

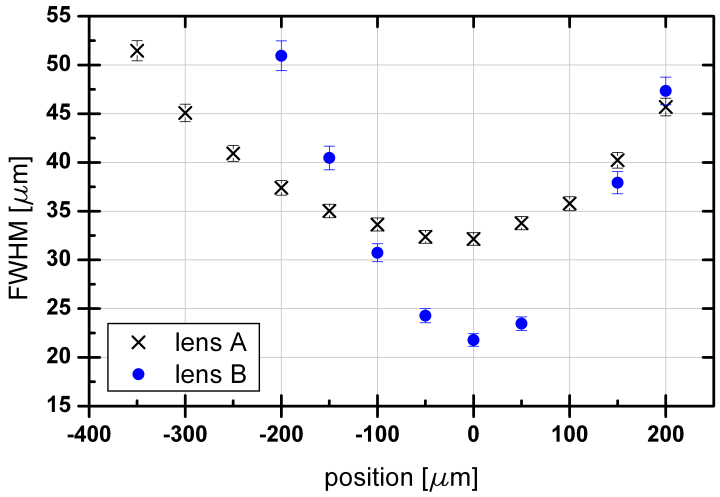

Figure 2.17: FWHM of the K_α line of nickel, obtained by scanning a 1 μm thick Ni foil at different positions along the lens axis. The result for both half-lenses is shown. Zero marks the position of the focal point.

2.5.2 Energy dependence of the FWHM

An ideal X-ray lens for confocal PIXE measurement would maintain a small focal size regardless of the X-ray energy. However, the expected energy dependence of the FWHM for polycapillary lenses derived from the total reflection law follows the $1/E$ law [65]. The measured energy dependence of the FWHM for lenses A and B and for the polyCCC placed at the focal point are shown in Fig. 2.18.

Our observations show an almost linear dependence of FWHM on X-ray energy in the 4 - 8 keV energy interval. For higher X-ray energies of up to 22 keV, the FWHM does not appear to change significantly. At low energies the FWHM drops again after exhibiting a local maximum at about 3 keV. The observed trends are in line with the results of Rackwitz et al. [84] and of Wolff et al. [69], except that in the later case, the authors did not report the results for X-ray energies below 3 keV. The reason for the observed FWHM reduction at low energies probably lies in the uneven absorption of the low energy photons that pass the lens capillaries with different curvatures. In this case the X-rays with higher impact angles on the walls of the external channels exhibit more total reflections and their absorption probability increases, which consequently reduces the FWHM of the lens acceptance volume.

In Fig. 2.18 we also report the certified FWHM values provided by the manufacturer for the focusing mode of operation, gathered in Table 2.2. The discrepancies between

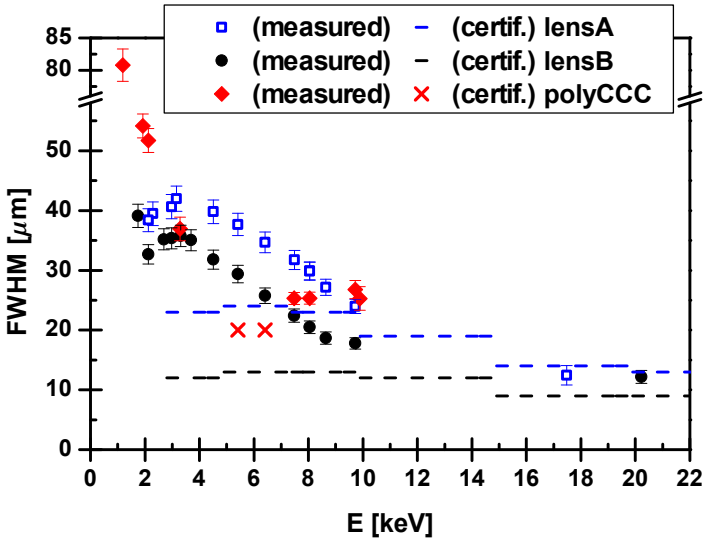

Figure 2.18: FWHM dependence on X-ray energy for the three tested X-ray lenses. Certified values for lens A and B are presented with dashed lines. The two crosses represent the specified values for the polyCCC.

the manufacturer's data with the data measured in this work are considerable for X-ray energies below 5 keV. Above 10 keV, the certified FWHM values for the focusing mode of operation overlap reasonably well with our data obtained in the collecting working mode. Evident discrepancies in the measured sizes of the focusing volume for the same lens working in the collecting or in the focusing mode have been observed earlier [36, 69]. This was explained by the divergence effect, i.e., the beam to be focused did not consist only of parallel X-rays that are most efficiently focused by the lens, but on the other hand, the divergence of the incoming beam was much smaller than that of the point-like X-ray source used for the characterization of the collecting half-lens. The manufacturer tested the lenses in the focusing mode with an X-ray source whose size (50 μm) was much smaller than the entrance (wider) diameter of the lens. Obviously, smaller X-ray sources placed at the same distance from the lens would result in a smaller spot size for the half-lenses working in the focusing mode, since the outer channels may not contribute to the transport of X-rays at all. The rather weak energy dependence of the certified data in the focusing mode proves this. The same effect lowers lens transmission at higher X-ray energies. In our case, with a point-like movable X-ray source in front of the conical end of the lens, the light is transmitted through all lens channels to generate the final map image. This results in a relatively

larger spot size and its stronger energy dependence.

The energy dependence of the FWHM for the polyCCC can be well described by the $1/E$ law up to the X-ray energies of 6 - 7 keV (Fig. 2.18). At X-ray energies above 9 keV the halo effect broadens the acceptance volume (Section 2.5.3).

2.5.3 Asymmetry and the "halo" effect for polyCCC

A short working distance limits the applications of a polyCCC in the confocal set-up. In addition, we observed unexpected intensity profiles of the measured acceptance volume cross-section far from the focal point, as shown in the profiles in Figure 2.19. Its shape resembles a comet and a 2D Gaussian function is obviously not a suitable profile approximation. When the foil was brought into a focal plane, the image was symmetric again. Therefore, we do not show the change of FWHM for different distances along the polyCCC axis. Another observation regarding the polyCCC is the strong halo observed at energies above 9 keV, that broadens the acceptance volume. The halo comes from X-rays that are not guided through the channels, but are transmitted directly through the lens material. An example of this effect is shown by image of Y K_α (14.88 keV) in Figure 2.20.

2.5.4 Total lens transmission

The total number of photons collected by the lens for a homogeneous planar target remained practically unchanged for a relatively broad interval of source-lens distances. Figure 2.21 shows the total Ni K_α yield, taken with lens B and the polyCCC at different positions of the Ni foil from the focal point. The integrated counts from the X-ray map were normalized to the same proton dose and divided by the total yield measured at the focal point. The observed dependence is linear; however the scaling coefficient is extremely small and the whole intensity does not change more than 5% in the $\pm 100\mu$m interval around the focal point. As the FWHM of the lens changed significantly in the range of the source-lens distance examined (Fig. 2.17), the 2D Gaussian distribution became broader, but its volume (the integral counts in the X-ray map) was approximately conserved. This conclusion is, among others, important in the depth profiling of layered samples in the scanning beam mode ([85] and chapter 3), where the only change of elemental concentrations is along the direction perpendicular to the sample surface. By knowing that the total transmission is independent of z'', a complete qualitative analysis of such samples can be made.

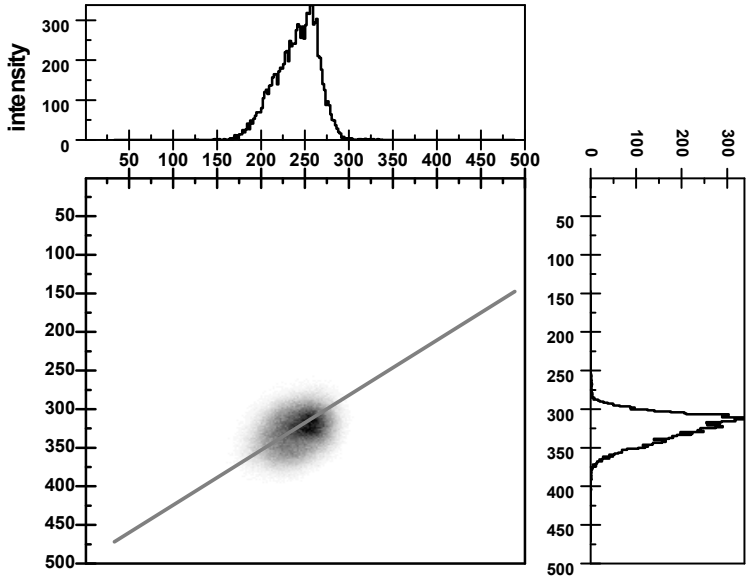

Figure 2.19: Image of Au M line, obtained from a 2 μm thick Au foil, measured with the polyCCC approx. 100 μm from the focal plane. Asymmetrical intensity profiles show up that cannot be described by a Gaussian function.

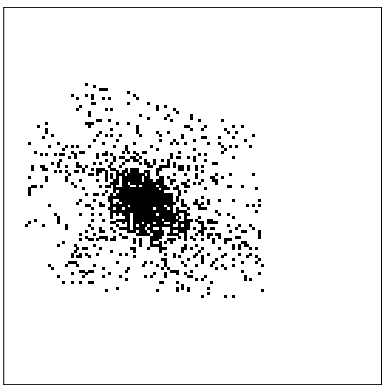

Figure 2.20: Map of Y K_α line (energy of 14.96 keV) from YF_3 deposited on a thin nuclepore polycarbonate aerosol membrane measured with the polyCCC. A strong halo is observed around the otherwise typical "cloud". The size of the scanned area is 500×500 μm^2.

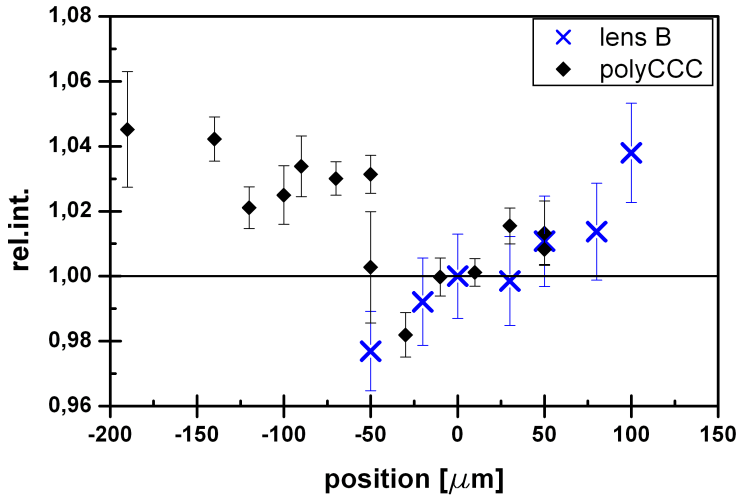

Figure 2.21: The relative total transmitted intensity of the Ni K_α line measured with lens B (crosses) and the polyCCC (diamonds).

2.5.5 Lens transmission efficiency

According to Eq. (2.4), the lens transmission efficiency T is obtained as the ratio of X-ray intensities measured with and without the lens attached. Without the lens the field of view of the X-ray detector was restricted with a pinhole of 1 mm radius, positioned 11 mm in front of the detector crystal. This was done to prevent intensity losses due to the finite detector crystal size. We assumed that, with and without the lens, the illuminated detector area has about the same size and does not extend outside the sensitive area of the detector crystal. The solid angle ratio $\Omega_{pin}/\Omega_{lens}$ in our experiment with lens B was about 16%. To determine Ω_{lens}, we took into account the fact that lens B has a 230 μm thick outer glass wall between the cover and the collecting structure, which does not contribute to the X-ray transmission.

Since the local transmission of the lens is governed by Eq. (2.5) and since the FWHM is now known, the only remaining parameter required to complete the lens description is T_0. In principle, T_0 is proportional to the detected X-ray intensity with the half-lens mounted and with the point-source placed at the lens focal point. To avoid its dependence on source brightness, we prefer to report T_0 divided by the X-ray intensity recorded without the lens and corrected for the solid angle ratio, as required by Eq. (2.4). The same result can obviously be obtained from the measured confocal X-ray map if the maximum number of counts in the map at the centre of the 2D Gaussian intensity distribution (recorded with the proton beam positioned at the lens focal point)

is divided by the average number of counts in the rather homogeneous X-ray map recorded in the pinhole experiment.

The measured T_0 dependence on X-ray energy is presented in Fig. 2.22. It was extracted from the measurements of Al K_α, Mo L_α, Ti K_α, Ni K_α, Cu K_α, Zn K_α, Ga K_α and As K_α lines. The energy dependence and the maximum transmission have similar trends to those reported in [69] and [84] for a different lens. At its maximum the transmission reaches around 17% for X-ray energies of 7 - 9 keV and drops rapidly at lower and higher E. At energies lower than 2 keV the maximum lens transmission is less then 1%. This could represent a major restriction on confocal PIXE when measuring very light elements in small concentrations, for example in biological samples. The "fitted" line presented in Figure 2.22 represent only a tentative trend of T_0 dependence on energy, since we did not derive any physiscal model to describe this dependency. For a given source type, positioning and experimental geometry, the data in Fig. 2.18 and Fig. 2.22 can be used to predict the confocal X-ray intensity map if the X-ray intensity of the same source obtained without the lens is known.

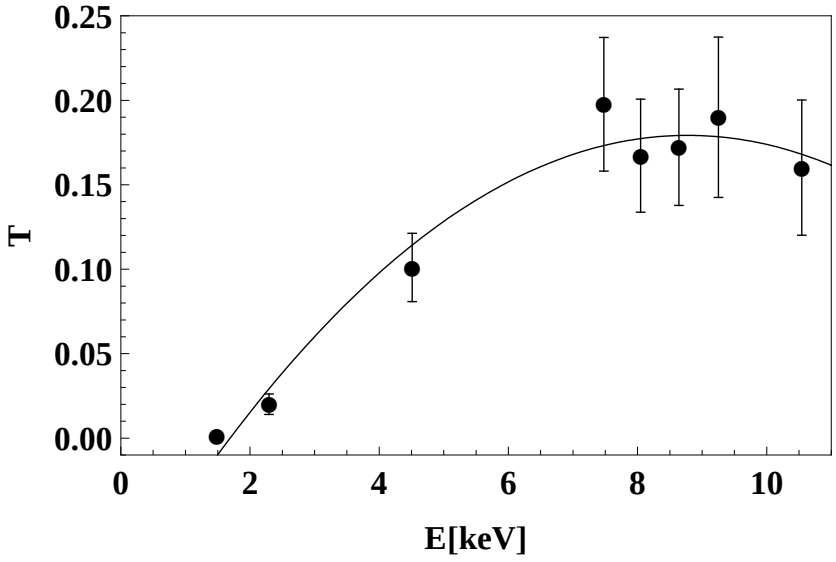

Figure 2.22: Energy dependence of the maximum lens transmission at the central point of the lens acceptance volume (lens B). The line represents the polynomial trend of the measured data. The transmission has a maximum at an X-ray energy of around 8 keV. A strong reduction of the transmission at low energies is seen. For energies above 9 keV, the transmission slowly decreases again.

The main error here comes from the exact determination of the pinhole-source distance. Much care was given in order for the detector with the collimator to be placed at the exact position of the detector with the lens. We estimated this distance to (17 ± 1)

mm. This gives around 6% of the relative error for this parameter. The lens-source distance is naturally the focal distance, that the manufacturer determinates with 0.1 mm tolerance, or 3%. Since we were measuring in the focal position and there is only about 10-20 μm possible misalign as described previously, no additional error is added. The aperture tolerance for a pinhole is around 5%. The entrance aperture of the lens is more tricky one to estimate. When taking into account the outher walls, the diameter of the inner aperture of the glass body is about 1 mm with ±0.05 mm error. Therefore, the solid angle ratio is determined with about 20% uncertanty. The statistical errors in the analysis of both intensities are connected with the number of counts in each line. The light elements have larger uncertanties, due to a stronger absorption. We conclude that for the strongest lines like in Ni K_α, Cu K_α, Zn K_α or Ti K_α, the uncertanty of the calculation is around 20%, while for Al K_α, Mo L_α, and GaAs (both K_α) it is higher.

When discussing lens transmission, two main types of losses are responsible for X-ray absorption. The first type corresponds to the direct losses in the walls of the individual capillaries. The second type of the absorption that happens at each total reflection due to the imperfect reflection. One can estimate whether the measurements described above are approximately correct.

The half-lens is composed of a bundle of small capillaries. For lens B, a single capillary inner diameter amounts to 1.3 μm. The intermediate space is filled with glassy material. The packing of the capillaries can be described by a simple honeycomb model, where the distance between the centres of two neighboring capillaries is 2.2 μm [92]. With such a hexagonal packing model of empty capillaries surrounded by glass walls, the ratio of the empty surface versus the total lens entrance surface is about 1/3. If X-rays hit the wall, they are practically completely absorbed. This effect diminishes the true lens acceptance angle so that the ratio $\Omega_{pin}/\Omega_{lens}$ should in fact be increased by a factor of three. The transmission trend in Fig. 2.22 remains unchanged, but all the data points should be scaled by a factor of three. Therefore, T_0 for energies around 8 keV increases to 50 - 60%. The only losses included in such scaled transmission values are those due to imperfect transmission of X-rays inside empty capillaries via total reflections. The intensity loss at each reflection is governed by the absorbing index β of the material and the reflection index is in reality always slightly smaller than 1 [66]. If we assume the intensity losses at each reflection equals few percents and additionally consider about 10-15 reflections as argumented before, then we can approximately explain the obtained transmission value T for lens B.

2.5.6 Spectral effects

At this point, we have empirically determined all the parameters of Eq. (2.5). We should be able to use this knowledge in analysis of the measurements made by the confocal PIXE method and an example with the quantification is a part of the next section 2.6. The effect of the lens energy dependent parameters can be seen in the PIXE spectra emitted from a homogeneous reference material. To understand these effects, we first compare the two spectra taken with and without the lens, and later, the spectra taken with the same lens with the point source at different positions with respect to the lens focal point. As evident, two effects are noticeable: the difference in the low energy part of the PIXE background and the different intensities of the characteristic spectral lines.

Fig. 2.23 shows the spectra measured for a 1 μm thick nickel foil with and without the optics. First, the spectrum was collected with the X-ray optics attached and the foil positioned in the focal plane. After that, the lens was removed and replaced by a collimator described in section 2.5.5 without changing the detector and the target positions. Both spectra were normalized to the most prominent line (in this case Ni K_α), since we are not interested in the full transmission of the lens as this was already debated, but only on specific effects on the spectra. Obviously, due to its very poor transmission for low X-ray energies, lens B (red line) cuts the normally occurring PIXE background (Figure 2.23, black solid line). Detailed analysis shows a small additional background at energies above 3 keV up to 5.5 keV. When comparing the point scans in the centre of the transmission function with and without the lens, only a reduction of the low energy part of the spectra is seen, but otherwise no change in the background appearance is observed.

The polyCCC lens, on the other hand, adds significant background to the spectra (blue line). The polyCCC covers a considerable solid angle and is hit also by the backscattered protons. Bremsstrahlung from the ejected electrons in the lens and the emission induced from the glass material are more easily transmitted through the straight channels, which may explain the additional background.

Fig. 2.24 exploits different regions of the map in terms of the spectral composition measured with lens B. Our reference this time was a GaAs nuclepore standard, with a nominal areal thickness of 184 μg/cm^2. The spectra associated from two distinct map areas are shown. The black line represents the spectrum of the central area of the Ga K_α map. This area encloses an ellipse defined by its origin in the spot centre and with σ_s and σ_l of the Ga K_α transmission function as minor and major semi-axes. The blue

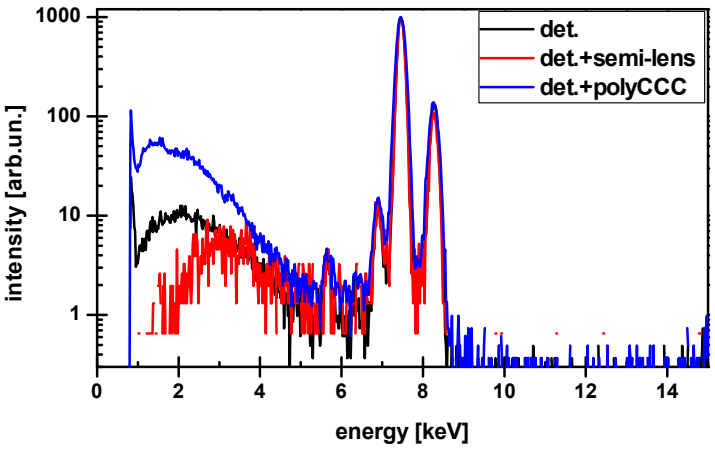

Figure 2.23: Three different spectra, taken from the same sample – a 1 μm thick Ni foil. The black line is the X-ray spectrum from the SDD detector with no lens. The blue line represents the SDD spectrum with polyCCC mounted. The red line shows the SDD spectrum recorded with lens B. Both lenses were always in their focal positions, while the detector-sample distance without the optics was the same as in the case of the measurements with the semi-lens B. In all three examples, the filter in front of the detector was 6 μm mylar coated with Al.

line represents the spectrum composed of counts outside this central area. The spectra are normalized to the Ga K_α line and large differences between the two spectra can be observed. The main two are the change in relative intensity of the characteristic As lines and the PIXE background that is about ten times higher at the edge area than in the centre.

Fig. 2.25 shows the calculated X-ray energy dependent ratio of X-ray intensities recorded at the central point of the 2D Gaussian distribution and the point at the minor semi-axis of the ellipse, separated from the centre for σ_s of the Ga K_α line, which is 7.8 μm. Both spectra are scaled to the same value at the Ga K_α emission energy (9.25 keV) to match the previous experimental example. The calculated ratio deviates from 1 due to FWHM and T_0 dependence on the X-ray energy. The measured relative intensity change of As spectral lines is therefore explained by our transmission model, while the measured relative background ratio in the low-energy part is much higher than the calculated value. It seems that transmission of X-rays via the outermost capillaries induces an additional low-energy background that is effectively transmitted through the lens. Another explanation could be purely geometrical; the backscattered protons and induced X-rays "see" more lens material when they are emitted from the outer points.

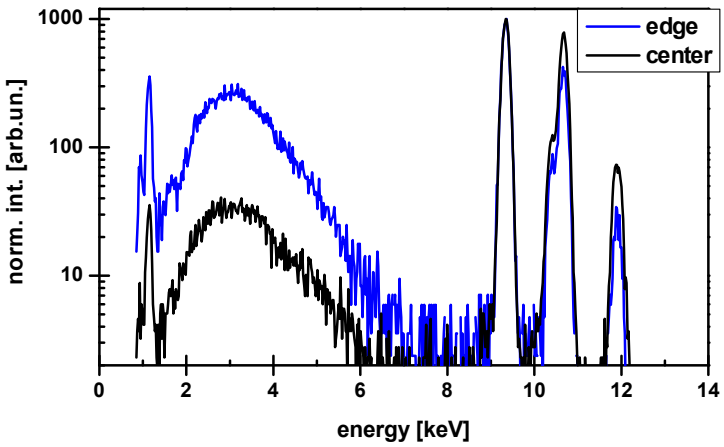

Figure 2.24: Two X-ray spectra, measured from a GaAs nuclepore standard, with the semi-lens B, normalized on the Ga K_α line. The black line represents the spectrum from the central area of the measured spot, extracted from the map scan in the interval of $\pm\sigma_{Ga}$ (7.8 μm) around the central point. The area outside this interval (whole map – 2σ) is represented by the blue line. The difference in the background from the two areas is significant. We can also observe an energy dependence of the transmission from different parts of the map.

2.6 Test of the set-up

Due to the well known processes of the proton-atom collision in the form of ionization cross-sections and stopping of protons in the sample, it is possible to determine elemental concentrations quantitatively by PIXE without the need of certificated standards. The ionization cross-sections were measured by several groups and are now compiled in databases and analytical softwares. The uncertainties in those collections vary between 5 to 20% and many times represent the major error in the resulting concentration values. Proton stopping powers are calculated in [90], ionization and production cross sections can be found, for example, in tables of Paul, Gardner or Chen [93–95], while X-ray fluorescence yields and photoabsorption cross sections are again available in dedicated databases, i.e. [68, 96, 97].

In principle, by counting the numbers of photons transmitted to the detector at individual energy, one can calculate atomic concentration of the corresponding element via equation (2.21), that relates photon yield to atomic density [1]. For quantitative calculation not only the atomic processes must be known, but also the experimental parameters: the detector efficiency, solid angle, the transmission of eventual absorbers

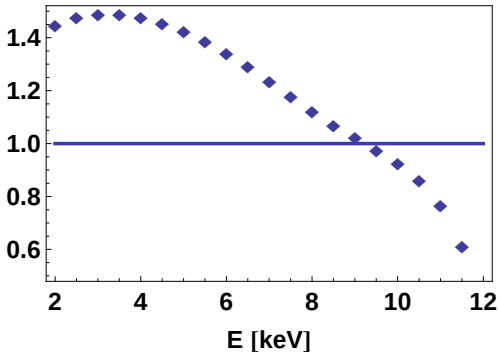

Figure 2.25: The difference between the intensities of an X-ray spectrum, taken at the central point of the lens acceptance volume and at the constant distance of 7.8 μm along the short axis of the ellipse, that corresponds to σ_s of Ga K_α line. Shown is the ratio between the intensities at the point $(0, \sigma_s)$ and $(0, 0)$.

and the beam current.

The yield Y^e of photons detected in the X-ray detector corresponding to the K emission lines of the element e of interest can be written as:

$$Y^e = N_p \, n^e_{\text{at}} \, \frac{\Delta\Omega}{4\pi} \, \eta^e \, \epsilon^e \, \omega^e \, b^e \int_0^R \sigma^e_i(E(x)) \, \exp\left(-\mu^{e\,f} \, l\right) dx. \tag{2.21}$$

The upper equation holds for the homogeneous distribution of element e in the flat thick sample. The individual parameters in the Equation (2.21) are: N_p is the incoming number of the projectiles, n^e_{at} is the unknown atomic density of the element e in units [at/cm^3], $\Delta\Omega$ is the detector solid angle, η^e describes transmission probability of absorbers for the characteristic X-rays of element e, ϵ^e is the efficiency of the detector at the energy of characteristic X-rays, ω^e is the fluorescence yield, b^e is a branching parameter describing a fraction of K X-rays of element e that appears in the K_α line, $\sigma^e_i(E(x))$ is the ionization cross section for K shell of the element e at the energy E, while $\exp(-\mu\, l)$ describes the attenuation of emitted characteristic photons of element e in the target, and f marks all other elements in the sample that contribute to the X-ray absorption. The distance that emitted X-rays travel in the specimen on their way to the detector is denoted by l. The expansion of photon yield from shells L or M is more complex due to many transition possibilities in the L or M shell. However, the photon yield of any characteristic radiative transition is proportional to the atomic concentration n^e_{at} of element e. Several software packages are available for the analysis of PIXE spectra, such as GUPIX [98, 99] or GeoPIXE [100, 101] code. The later is used for the analysis of micro-PIXE data recorded in the mapping mode.

If an X-ray lens is placed in front of the detector, the number of photons detected is diminished due to the absorption in the lens. The transmission probability of photons through the lens, described by Equation (2.5), is considered as an additional absorber in the Equation (2.21). If the average elemental concentrations are sought or homogeneous samples studied, then the average transmission through the lens provides a sufficient input at selected X-ray energy. For more demanding applications, it is necessary to take into account a lateral variability of the lens acceptance profile. At this moment, no software is capable to include such complex "absorber" in the analytical process, so the computational approach has to be adopted for each specific code or application separately.

2.6.1 Nickel standard

As an example of the CF PIXE performance, we tried to determine the concentration of Ni in the Ni foil, used as a standard. This is routinely done in PIXE analysis: several targets with known elemental concentrations (standards) are measured at the same conditions and analyzed to the exact efficiency and/or the detector solid angle. In this section, we want to explore similar procedure to test the ability of CF PIXE as a tool for quantitative analysis.

The photon yield of Ni standard is described by the Equation (2.21) with the additional term from Equation (2.5) that describes the lens transmission. The standard is approximately 1 μm thick (the detailed thickness was determined by the RBS method and is described later on), so we can safely neglect the beam stopping and photon absorption. The 3 MeV proton beam loses 58 keV, about 2% of its energy in 1 μm of metallic nickel. At such small energy change the ionization cross-section does not change for more than 4% and could be considered constant [93]. The transmission of Ni K_α photons that are emitted from the deepest layer on the foil is 95% [68] so that target absorption can be neglected as well. The photon yield from Eq. (2.21) for such a thin target can then be expressed as:

$$Y^{Ni} = N_p \, n_{\mathrm{at}}^{Ni} \, \frac{\Delta\Omega}{4\pi} \, \eta^{Ni} \, \epsilon^{Ni} \, \omega^{Ni} \, b^{Ni} \, T^{Ni} \, \sigma_i^{Ni}(E_0) \, d(Ni), \tag{2.22}$$

where Y^{Ni} is the number of Ni K_α photons detected, n_{at}^{Ni} is the atomic density of Ni in units of at/cm^3, T^{Ni} the lens transmission function for Ni K_α photons, E_0 the initial beam energy and d(Ni) the thickness of the foil. In databases the ionization cross section is given in barns (= 10^{-24} cm^2). We are looking for the areal density of nickel

atoms, expressed in the units of at/cm^2.

The solid angle of the lens $\Delta\Omega = 0.06$ is calculated from the lens specifications. σ_i (3000 MeV) = 288.4 barn, fluorescence yield of Ni K_α photons is 0.41 [102], while the branching ratio b of Ni K_α line is calculated taking into account different intensities of three possible sub-lines composed in a K line ($K_{\alpha\,1}$, $K_{\alpha\,2}$ and K_β). As we do not resolve $K_{\alpha\,1}$ and $K_{\alpha\,2}$, the branching parameter b is calculated as [4]:

$$b = \frac{1}{1 + \frac{K_\beta}{K_\alpha}}. \tag{2.23}$$

The value for the parameter b for Ni is 0.9 [97]. The detector efficiency ϵ is almost 1 for such high energies and the ultra-thin window placed in front of the detector transmits practically 100% of 7.48 keV photons. The transmission of the mylar absorber with added Al is 98% as calculated from [68].

The proton dose is extracted from the number of protons backscattered (BS) from a golden layer of chopper, as described in section 2.1. The number of BS protons is directly proportional to the total number of protons. The proportionality constant is a dose normalization factor, that is in principle dependent on many factors like type of accelerated ions, their energy and charge state etc. Therefore it has to be determined for every type of ions from many measurements of standard material at different energies. As the chopper is positioned before the microbeam chamber (Figure 2.2), the proton beam does not interfere with the detectors in the chamber, so we keep the normalization factor the same for all. The factor is $3.71 \cdot 10^{-6}$ μAs/count for 3 MeV protons. For Ni measurement, the proton dose of 0.19 μAs applies for the whole X-ray map, which means $7.3 \cdot 10^7$ protons (N_p) for each pixel of 128×128 pixels in 250×250 μm^2 map. The total number of protons in the map is therefore $1.2 \cdot 10^{12}$.

Transmission function T_{Ni} can be composed with Equations (2.8) and (2.11). For Ni K_α the maximum transmission $T_0 = 0.17$ and $\sigma = 9.4$ μm (sections 2.5.2 and 2.5.5).

There is around 70 counts per pixel in the maximum of the measured map and the total yield is 13640 counts. We have now defined the model that can be compared with the measurements. If we start with the simplest analysis, we can calculate the unknown parameters $n_{\mathrm{at}}^{Ni}\ d(Ni)$ of the Equation (2.22) for each pixel. We get a simple concentration map presented in Figure 2.26. The axis z this time labels the values of areal number density $N_{at} = n_{\mathrm{at}}^{Ni}\ d(Ni)$ of Ni atoms. As the sample is homogeneous and the lens sees only part of the foil, the profile projected on x or y axis should be a rectangular function, however the problem represents statistical fluctuations at the

edges of the spot that are visible on the map and on the profiles. They arrive from the areas that should have very small transmission probability as determined by the Gaussian profile. However, we did measure one or two counts at some of that pixels and this leads to huge statistical errors. As the solution, we artificially suppressed the values in most those pixels to 0, however some peaks remained as seen on Figure 2.26. Discrepancies from the central map area are again connected with statistical fluctuations from the theoretical smooth Gaussian function used for the calculations.

Taking those fluctuations into account, the concentration distribution function is almost flat. The average height is $9.18 \cdot 10^{18}$ cm^{-2}. To check the performance, we calculated the concentrations also from the central maximum only and we got $1.12 \cdot 10^{19}$ cm^{-2}.

Another approach is to use the total K_α X-ray yield accumulated over the whole map area. This time, the whole proton dose must be used and the transmission is averaged over 128×128 pixels. The Ni concentration obtained by this approach amounts to $1.04 \cdot 10^{19}$ cm^{-2}.

To verify the results, the thickness of Ni foil was checked with RBS method and calculated using the SIMNRA code [103, 104]. The resulting area density for our Ni sample was $9.5 \cdot 10^{18}$ cm^{-2}. This is in a reasonable agreement with our results obtained by CF PIXE. We are therefore a step closer to quantitative analysis with CF PIXE, at least for heavier elements. For light elements one needs an accurate detector description which has not been specified yet for the new SDD. However, as mentioned in section 2.5.5, low X-ray energies undergo strong absorption in the lens, so they are not of our interest at the moment.

2.6.2 Titanium thick standard

The next example was titanium thick target. Again, the target is assumed to be composed 100% of Ti and we want to reproduce the concentration with the CF PIXE measurement. The procedure is very similary as with Ni foil, appart that here the signal is originating also from deeper layers of the target and this has to be taken into account. A partial yield of Ti K_α photons from layer at taget depth z and thickness dz is:

$$dY^{Ti} = N_p \, \frac{\rho^{Ti} \, N_A}{M^{Ti}} \, \frac{\Delta\Omega}{4\pi} \, \eta^{Ti} \, \epsilon^{Ti} \, \omega^{Ti} \, b^{Ti} \, T^{Ti}(x, y, z) \, \sigma_i^{Ti}(z) \, \exp(-\mu^{Ti} \, l(z)) \, dz. \quad (2.24)$$

The ionization cross section σ_i is energy dependent and since the proton energy is diminishing with z, σ_i^{Ti} is dependent on z as well. The part of Equation (2.24),

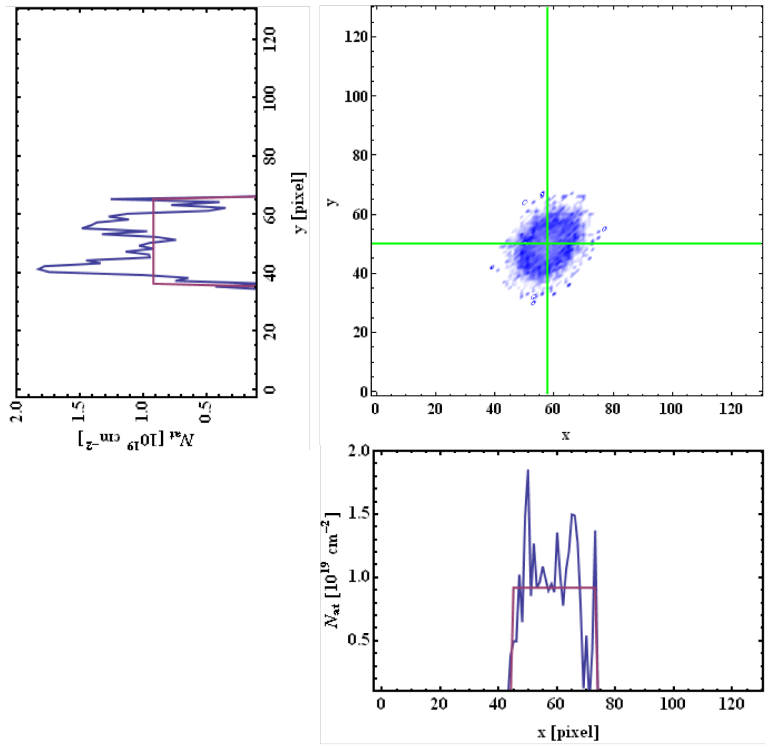

Figure 2.26: Calculated concentration map of nickel foil, reduced only to the detectable area. The origin was taken from measurements and is at (58,50). Profiles at $x = 58$ (left) and at $y = 50$ (below) present calculated concentration profiles (blue) and their real trend (purple). The discrepancies appear from the statistical fluctuations. x and y axis are presented in pixel units and the physical size of the frame is $200 \times 200\ \mu m^2$.

$\exp(-\mu^{Ti}\, l(z))$, describes photon attenuation, μ^{Ti} is the attenuation coefficient for Ti K_α photons in Ti sample and l denotes the path those photons travel in the sample and equals $\frac{z}{\cos\vartheta \cos\varphi}$. It is changing with depth z, at which the emitted photons are created (Appendix A.2, Eq. (A.8)). M^{Ti} is the molar mass of Ti, the rest of the parameters have the same meaning as before, valid for Ti K_α photons with the energy of 4.51 keV. For this measurement, the number of protons impinging at the whole sample frame is $1.8 \cdot 10^{11}$, the solid angle is the same as for Ni target, the detector efficiency equals 1, the absorption of Ti K photons in ultra-thin window is neglected, while the absorber transmission is 94%. Fluorescence yield of Ti K is 0.214 and the parameter b 0.91.

With thick targets, the partial yield from Equation (2.24) had to be determined for every layer dz and then the signal summed over all target layers. First, the depth z(E) is obtained from the knowledge of stopping power [90] for some small amount of dE. For our calculations, the energy step dE was taken to be 100 keV and the associated

range dz (layer thickness) of protons for each proton energy E was determined. Then, the ionization cross-section for each energy in the center of dE interval was extracted from [93]. The absorption was calculated for each sample thickness $z_i + dz$. The lens transmission was again calculated using parameters from lens characterization. In addition, T^{Ti} was taken to be z dependent and $\sigma = 13.2$ μm. In accordance with the section 2.4, the total yield is obtained by multiplying all factors from the second part of the Equation (2.24) $\left(T^{Ti}(x, y, z)\ \sigma_i^{Ti}(z)\ \exp(-\mu^{Ti}\, l(z))\ dz\right)$ for each z. This was then multiplied by other remaining factors, independent of z and after that each dY was summed together. Using the total measured yield, the model gives 120% concentration of Ti. Since the uncertanty of T_0 was estimated before to be around 20% and there are also expected errors regarding tabulated values of ionization cross-sections or attenuation coefficients and finite precision in determining the proton dose, the level of agreement is plausible. Since 5% error is normally encountered with PIXE measurements of standards, we can conclude that the quantifiction of CF PIXE with the presented lens description works satisfactorily for heavier elements.

Chapter 3

Applications of CF PIXE: Depth-resolved measurements

After presenting the CF PIXE set-up and a detailed characterization of the polycapillary lenses, the next step of the thesis is to apply the method for depth- or three-dimensionally resolved elemental microscopy. First, we briefly demonstrate the ability of the confocal PIXE for the analysis of layered samples.

3.1 Principles

Measurements with CF PIXE can be executed in several measurement modes. In the sample scanning mode, the proton beam is kept at the given position while the target is shifted along the beam direction (Figure 3.1 left). If a homogeneous thin target is hit, the measured photon yield is proportional to the lens transmission along the beam direction. For layered samples, the target movement brings successive layers into the "sensitive" volume and the measured photon yield reveals elemental concentrations in different layers. However, the signal is affected also by the stopping power and X-ray transmission of the layers positioned closer to the detector. The signal from the sample scanning mode is sensitive to the sample thickness, density, layer position or elemental concentrations – in addition, all this informations can be extracted by careful data analysis [46, 48, 66]. In the beam scanning mode (Figure 3.1 right), the proton beam scans the stationary target as in the standard μ-PIXE method – the measured map contains information on the target area crossed over by the acceptance volume of the lens. Using it with the layered sample, dislocated elemental "clouds" are obtained at

the positions where the beam position overlaps with the lens acceptance volume. In this way, the elemental depth distributions of layers can be obtained within a single beam scanning of the sample. The beam scanning mode is extremely useful in the alignment procedure and is used to characterize the X-ray lenses. As presented, it can be also used for depth-resolved measurements.

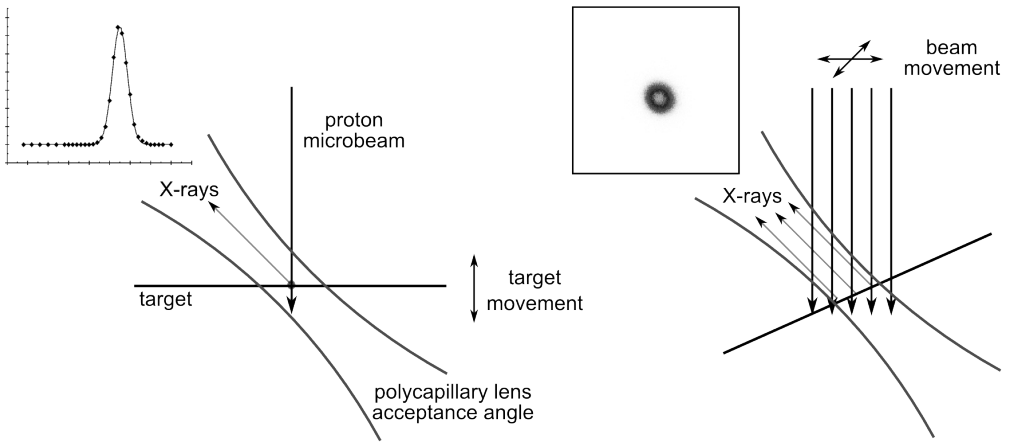

Figure 3.1: The sample (left) and beam (right) scanning mode in confocal PIXE.

3.2 Analysis of layered samples

Depth-resolved measurements of layered material represented the first application of CF PIXE [46, 51]. By "layered material" we describe laterally uniform samples with non-uniform depth elemental distributions. Such samples can be measured with both measurement modes shown in Figure 3.1. The confocal PIXE in the sample scanning mode can very well distinguish between thick and thin targets, since for thick targets the photon yield curve spreads and the position of its maximum moves (Figure 2.16b). For targets with homogeneous layers, element composition of individual layer can be investigated (keeping in mind the absorption of individual element X-rays in upper layers) together with its thickness and position. The analysis is limited to the local target area defined by the beam position. When such analysis is sequentially executed at several points of the sample, it provides a detailed characterization of the target.

Depth profiling with sample scanning mode was extensively studied in our first CF PIXE experiments [46, 48]. Layered samples of cultural heritage and car paint layers were measured and a model for quantitative analysis of such measurements was developed. As the subject was already described in detail, even though the measurements

were not performed with the new CF system, we did not elaborate in details on the topic in the scope of this thesis. An example of depth-resolved measurements in the sample scanning mode with the new system is presented in Figure 3.2a. The sample consists of two thin (1 μm) Ni foils separated by 25 μm of kapton. A considerable gap remained in between the foils after the evacuation of the chamber. Exact interspacing distance between the two nickel foils was therefore not known.

The sample was measured with lens A. The simple fit revels two Gaussian profiles centered at the sample displacement along the beam direction of (-3.1 ± 0.7) μm and (-305.4 ± 1.6) μm measured from the confocal reference point. The second peak has lower intensity due to the absorption of Ni K photons in kapton and the first Ni foil. The displacement of the two peak centroids give us the geometrical separation of the two foils. The resulting geometrical distance between the two Ni foils equals (302.3 ± 2.3) μm. The foil distance may vary from point to point due to the variation of the gap thickness.

An even simpler and quicker way for layered material analysis that can give information on the number of layers, their elemental composition and thickness, is provided by the beam scanning mode (Figure 3.1 right). Very similar characteristics of multilayered targets can be deduced from both measurement modes described in Figure 3.1, as long as the right deconvolution of maps for identical elements is possible. In most of cases, beam scanning mode can be used for successful depth profiling and that means we get depth elemental concentration profiles from just one lateral scan. An example is again a stack of two Ni foils separated by 25 μm of kapton measured by lens A. With the beam scanning of the sample in one position, we could distinguish the two Ni layers and calculate the difference between the two clouds on the map to be $d = (290 \pm 5)$ μm. As observing angle of detector with the lens is 45 degrees (angle between vectors $\vec{z}$ and $\vec{z}''$, see appendix A.1) and the distance between foils (D) can be calculated as $D = \frac{d}{\tan 45^\circ}$, this transfers directly into distance between foils, $D = (290 \pm 5)$ μm. No further analysis was made at this point, however, this showed the possibility to deduce depth information from a measurement at fixed sample position. One should again stress the fact, that for this kind of measurement, the sample should be composed of homogeneous plane layers at a scale of at least few hundred μm extent.

Another example of an elemental depth profiling in the beam scanning mode is presented in Figure 3.3. The sample was copper metal coated with a layer of tin. Stripe of copper was first cleaned and etched in HCl acid. Copper stripe was then dipped

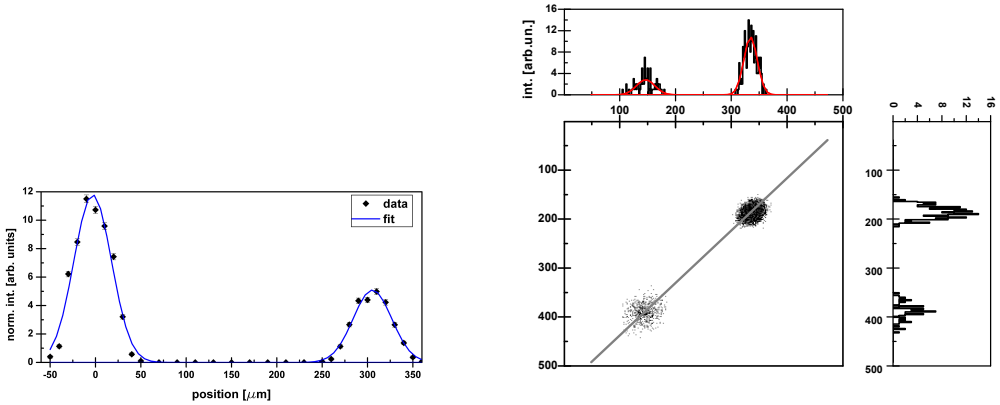

(a) Sample scanning mode (b) Beam scanning mode

Figure 3.2: Depth profile measurements of an artificially made layered sample, consisted of parallel and homogeneous Ni/kapton/Ni foils. The image was measured with a polycapillary half-lens A in sample scanning (a) and beam scanning mode (b). From both measurements we can deduce the information about the number of layers (2), their composition (pure Ni) and relative position with no numerical analysis at all. The size of the frame of the example b) is $500 \times 500\ \mu\text{m}^2$.

in molten tin and slowly extracted in order to form a tinned silver-like surface. In Figure 3.3 the maps of Cu K_α (b) and Sn $L_{\alpha\,1}$ (a) lines are shown. Detailed analysis shows that the displacement of two spots is indeed observable, the centers are apart for $7.9 \pm 1.0\ \mu$m. This is in good agreement with RBS measurements in air, where the thickness of Sn layer was determined to be $8.3\ \mu$m with a roughness of $2.7\ \mu$m [105].

When the coated layer is too thin, the CF PIXE method fails, even with a better lens. One example is a Au plated commemorative medal. RBS measurements show that the medal is made of brass (a mixture of Cu, Zn and Ni) with an extremely thin golden layer of around 50 nm [106]. With CF PIXE (lens A) we detect strong Cu signal (Figure 3.4a). Other elements presented in brass were detected but are not presented here. The golden peak can be detected also with the lens (Figure 3.4b), however the yield is too low and the spot displacement to small to resolve any depth distribution of elements.

Several other applications of depth profiling with CF PIXE are possible and the examples given have only demonstrated the efficiency of the method. The emphasis of the thesis was given to 3D analysis, described in the next chapter.

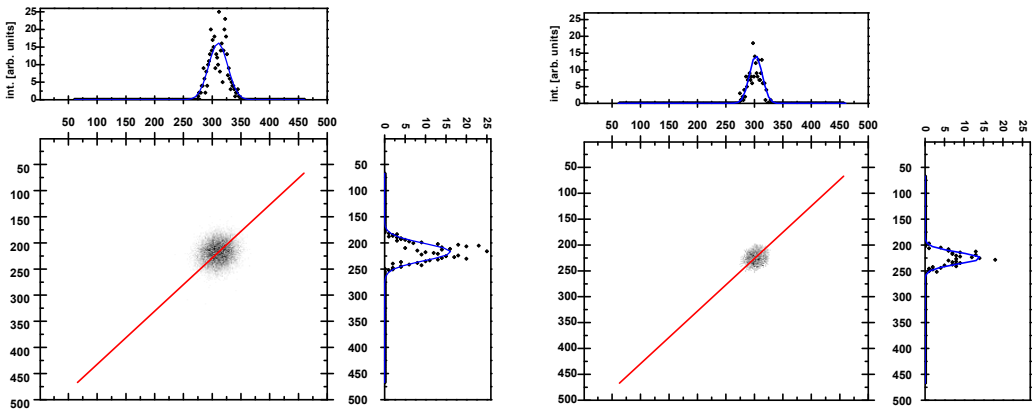

(a) Sn (b) Cu

Figure 3.3: Depth profile measurements of a tinned copper sample, consisted of Sn layer on Cu substrate. The elemental maps were obtained by the polycapillary half-lens A in beam scanning mode. We can deduce the physical separation of both composed elements from the center position of two elemental maps – Sn (a) and Cu (b). The dislocation of the two centroids indicates the depth distribution of elements. The size of the frame is $500 \times 500\ \mu m^2$.

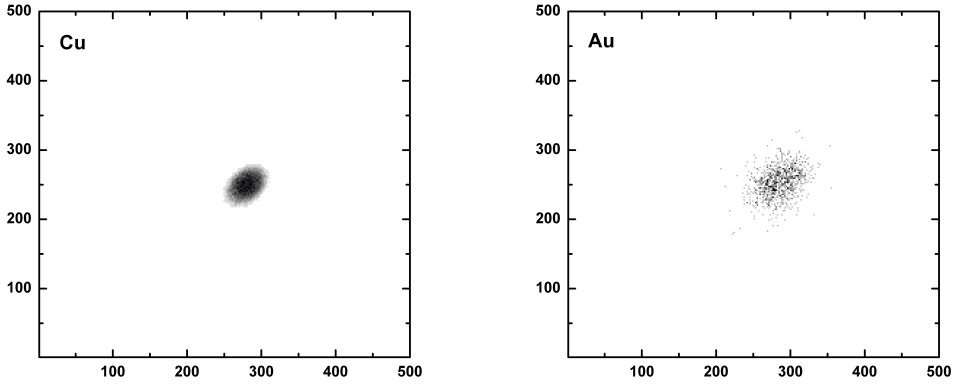

(a) Cu (b) Au

Figure 3.4: Depth profile measurements of a plated commemorative medal, consisting of thin Au layer on brass substrate. The elemental maps were obtained by the polycapillary half-lens A in beam scanning mode. Strong Cu signal from the brass was measured (a) together with other elements (Zn, Ni, Fe), while the upper gold layer gave extremely small yield (b). There is no visible dislocation of the two centroid positions. The size of the frame is $500 \times 500\ \mu m^2$.

Chapter 4

Applications of CF PIXE: 3D-resolved analysis

The final goal of the CF PIXE experiments is to develop an analytical protocol for complete 3D elemental analysis, also referred to as elemental tomography, combining restricted volume sensitivity of the confocal set-up with proton beam scanning and controlled sample movement. We demonstrate the applicability of the approach by the reconstruction of Ti and Zn distribution in gunshot residue particle.

4.1 Principles

The combination of the beam- and the sample-scanning modes, both described in Chapter 3, is required to obtain the information on three-dimensional elemental sample composition. The tomography measurements are executed as a sequence of scans measured at different positions of the sample along the z axis of the coordinate system *S* (Figure 4.1). Without the X-ray lens attached, the elemental maps acquired by the X-ray detector would be identical. However, due to the restricted field of view, achieved by the lens, each X-ray map is different and the collected information allows for the extraction of concentrations beyond the microbeam 2D resolution. In such approach to the elemental tomography, no special sample preparation is required. In addition, there is a possibility to obtain a certain grade of 3D information even if the sample is so thick that the protons are not transmitted. In such a case, the information is obtained only from the fraction of the sample close to the surface, but this may still mean a considerable sample depth, depending on the element specific information depth in every

individual experiment.

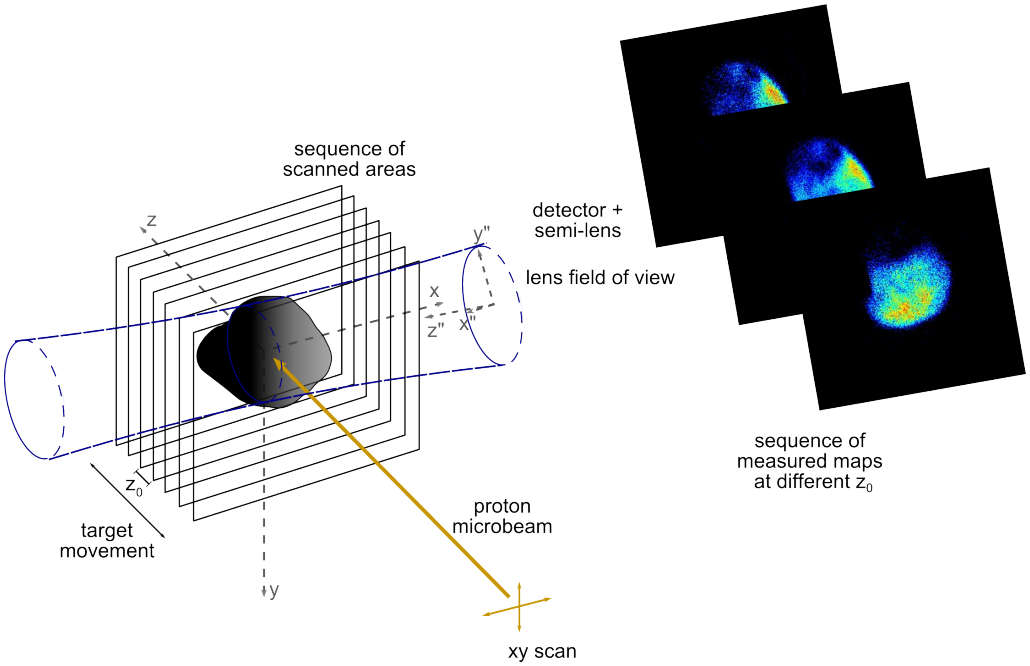

Figure 4.1: Tomography measurements with CF PIXE. The sample is translated along the beam axis (z) in equidistant steps z_0. At each position, X-ray mapping takes place by a fast proton beam scanning over a selected area in the xy plane.

With 3D CF PIXE measurements, a series of maps of a given object is recorded as seen on Figure 4.1. Each map represents the detected photon yield sorted according to pixels denoting a particular lateral beam position (x,y). The number of detected photons at each pixel is dependent on the probability that atoms along the proton path would be excited to emit characteristic X-rays and also on the probability that emitted photons would survive their way to the detector. The pixel X-ray yield depends on the type and amount of atoms along the proton path, as well as on the sample composition along the corresponding path toward the detector. In order to reconstruct a 3D elemental distribution of an object from a series of CF PIXE maps, the space is divided into unit cells. Regardless of division, the cell is assumed to hold a constant concentration n_{at}^{e} (in units atoms/cm^3) of each element e in question and it is the value of n_{at}^{e} for each unit cell to be determined by the analysis. If the cell volume is large, the division is coarse and the spatial resolution is poor. On the other hand, if we work with very small cells, the reconstructed three-dimensional distribution would resemble the real ones in more details. The decision would go in favor of the smallest cells possible, however the reasonable division density is determined by the experimental parameters, such as the lens FWHM, the size of the proton beam, the sample translation interval

z_0 and the geometry of the set-up, so a compromise has to be taken. The shape of the cells is governed mainly by two parameters, the direction of protons in the sample and the detector (lens) axis. A detailed discussion of the possible cell's shape was given in [50], however the general three-dimensional nature of the set-up was not considered. In the previous improvised set-up, the detector with the lens as well as the other detector used for monitoring purposes laid in a horizontal plane. As the microbeam scans the sample surface with a horizontal (x) series of vertical (y) scans, and the beam penetrates the sample along z direction, all photons emitted toward the detector laid in the same horizontal plane, characterized by fixed y coordinate along the vertical beam direction. In this case, the three-dimensional problem can be relatively easy decoupled into a series of two-dimensional problems, since the relevant processes that determine the PIXE yield occur in the horizontal plane. In other words, the lines (x, fixed y) in a sequence of maps recorded at different sample position z contained all the information about elemental concentrations in (x, fixed y, z) plane of the sample [47]. In general situation that applies for the present set-up, this is no longer true. We can still find a target plane defined by both crucial directions – the proton path and the photon detection path, however its projection onto the lateral X-ray map is not horizontal any more. The reconstruction therefore begins by indicating pixel lines that lie on the common excitation-emission plane of the sample.

As the beam sweeps the sample, the "row" (x, fixed y) in the measured map represents one horizontal plane xz and the "column" (fixed x, y) represents one vertical plane yz. The protons in the position (x, y) travel along the z axis and looses their energy along the path. The energy of the proton beam in a particular cell (x, y, z) is dependent on the concentration of all elements in the previously passed cells $(x, y, z - N\Delta z)$, where N counts these cells and Δz the cell size along z axis. The ionization cross-section for a particular element in the cell is also determined by the proton beam energy in the cell. Photons are emitted into the full solid angle, however only those are measured that arrive to the detector. On their way some of them are absorbed by the sample, and the absorption is described by the attenuation coefficient for each element/material. Therefore, the number of photons created in the cell (x, y, z) in the laboratory frame that survive their journey toward the detector is related to the cell occupancy along their way out of the sample along the $-z''$ axis in the lens frame (section 2.4). Even though one would "naturally" divide the sample into regular cubic cells with edges aligned to the three vectors $\vec{x}, \vec{y}, \vec{z}$ that spans the beam coordinate system S, such a division is not practical for the reconstruction process. The absorption effect in such cell division is fairly difficult to describe, as the photon path would have to be calculated for each cell

individually and the concentrations weighted accordingly.

To overcome this difficulty, another coordinate system Σ is introduced, with axes along the three linearly independent vectors $\vec{\varsigma}, \vec{\tau}$ and $\vec{\upsilon}$. These vectors are expressed by the previously introduced vectors,

$$\vec{\varsigma} = \vec{z}, \quad \vec{\tau} = \vec{y} \quad \text{and} \quad \vec{\upsilon} = \vec{z}''. \tag{4.1}$$

Such a coordinate system is still positively oriented, however it is not orthogonal any more (Appendix A.1). The space is now divided into cells in a form of a parallelepiped, each with the edges aligned along three vectors $\vec{\varsigma}$, $\vec{\tau}$ and $-\vec{\upsilon}$. One such cell is presented in Figure 4.2. The length of the cell edges are $\Delta\varsigma = \Delta z$, $\Delta\tau = \Delta y$ and $\Delta\upsilon = \Delta z'' = \frac{\Delta x}{\cos\vartheta \sin\varphi}$. The volume ΔV of each cell is determined by the triple product of the normalized vectors $\vec{\varsigma}, \vec{\tau}$ and $-\vec{\upsilon}$ which gives $\Delta x \Delta y \Delta z$.

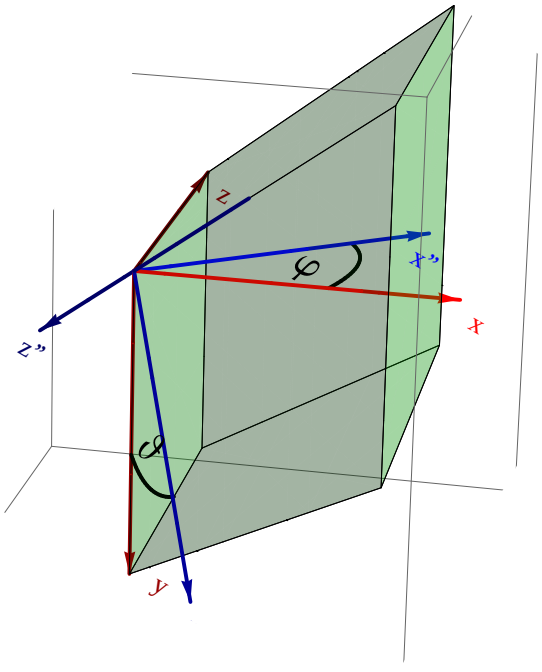

Figure 4.2: Basic cell for the 3D reconstruction with edges along vectors $\vec{\varsigma}, \vec{\tau}$ and -$\vec{\upsilon}$.

As the space division is discrete and all cells have the same size, we define three numbers i, j, k ($i, j, k \in \mathbb{Z}$) that count cells along x, y and z axis. The cell centers

have therefore coordinates $\left(\Delta x(i-\frac{1}{2}), \Delta y(j-\frac{1}{2}), \Delta z(k-\frac{1}{2})\right)$. In the coordinate system Σ the numbers $\tilde{k}, \tilde{j}, \tilde{i}$ are introduced that count cells along ς, τ and υ. Since $\varsigma = z$ and $\tau = y$, the numbers k and j coincide with $\tilde{k}$ and $\tilde{j}$ for $z'' = 0$. In all other cases we will have to keep the distinction. The cell centers in Σ are then at coordinates $\left(\Delta\varsigma(\tilde{k}-\frac{1}{2}), \Delta\tau(\tilde{j}-\frac{1}{2}), \Delta\upsilon(\tilde{i}-\frac{1}{2})\right)$.

In figure 4.3 the relation between the space division in described cells and the pixels from each map is presented. In the coordinate system S the connection is simple. Each pixel (x, y) can be described on the measured map with a pair of indexes (i, j) (Figure 4.3a (upper part)). If the origin of the coordinate system is taken at one corner of the map, the centers of each pixel have coordinates $\left(\Delta x(i-\frac{1}{2}), \Delta y(j-\frac{1}{2})\right)$. The number of counts in each pixel represents PIXE yield acquired at this particular beam position. In order to associate the map measured with the cells determined in the coordinate system Σ, the planes $\varsigma\upsilon$ have to be identified. In figure 4.3a (lower part), and more detailed in figure 4.3b, we can see, that strips of pixels $(i + a, j + b)$, where $a = b = 0, 1, 2, 3, \ldots$, are lying on a specific $\varsigma\upsilon$ plane. In the new presentation on Figure 4.3a pixel notation (i, j) is transformed into $(\tilde{i}, \tilde{j}) = (i, j - i)$ (refer also to Figure 4.11 on page 99).

The photon yield of each element in the spectrum is governed by equation (2.21). The photons emitted from each cell are summed over the whole proton path and weighted with the probability that they are transmitted to the detector. A lens field of view and its transmission function must be considered. The lens probing volume size (FWHM from the equation (2.5)) determines the area that can be seen by the detector while the absorption proprieties are described by the transmission efficiency T^e. The normalization of maps is performed by dividing each pixel with the corresponding number of Au counts from the RBS spectrum of the chopper (N_{ch}), as will be described in more detail further on (page 98). Such a reduced number of photons from each pixel $(\tilde{i}, \tilde{j})$ from each map, can be written as:

$$\frac{N^e(\tilde{i},\tilde{j})}{N_{ch}(\tilde{i},\tilde{j})} = \overbrace{\frac{K}{e_0}\frac{\Delta\Omega}{4\pi}\eta^e\,\epsilon^e\,\omega^e\,b^e}^{F^e}\sum_{\tilde{k}}\Big[T^e(\tilde{k},\tilde{j},\tilde{i})\,n^e_{at}(\tilde{k},\tilde{j},\tilde{i})\,\sigma^e_i(E(\tilde{k},\tilde{j},\tilde{i}))\cdot \cdot \exp\left(\sum_{\tilde{i}>\tilde{i}}\sum_f -\mu^{e,f}(\tilde{k},\tilde{j},\tilde{i})l(\tilde{k},\tilde{j},\tilde{i})\right)\Delta z\Big]. \tag{4.2}$$

In the equation (4.2), a superscript e refers to a particular element e which we analyze, while f denotes all other elements present in the sample that affect the proton stopping and photon absorption probability. K is the dose normalization factor. All other pa-

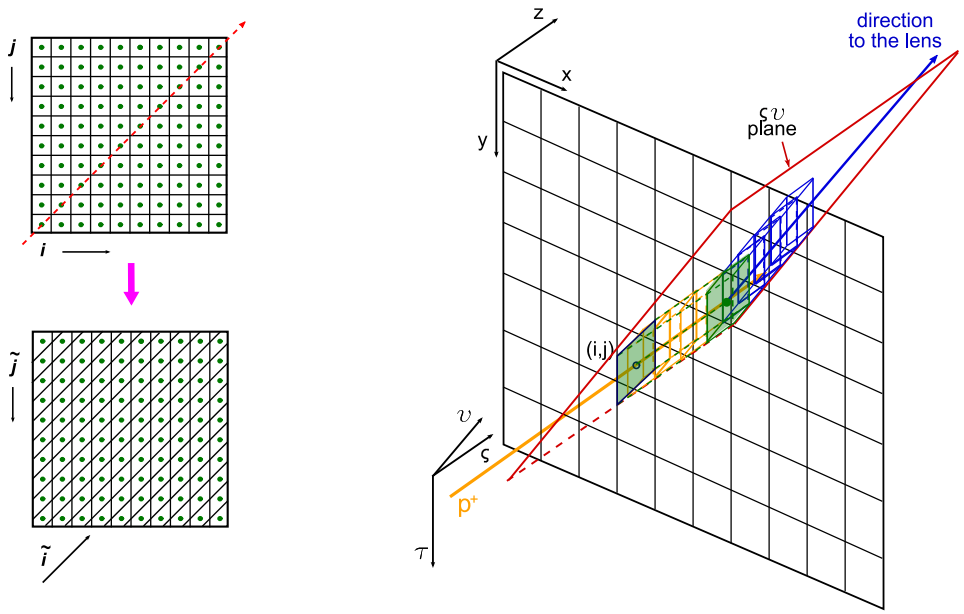

(a) Map pixels

(b) Cells in 3D

Figure 4.3: (a) An example of pixels (i,j) on the X-ray map. In the lower image, the same map is presented, however pixels are now counted by the pair of indexes $(\tilde{j}, \tilde{i})$. The shape of newly formed "pixels" corresponds to the projection of unit cells on the xy plane.
(b) Realistic situation of the unit cell positions in system Σ. An example of a standard "map" consisting of pixels is shown, with selected unit cell in space together with its projection (green). A $\varsigma\upsilon$ plane is presented in red, while some of the unit cells along the proton beam direction are depicted yellow, the ones in the direction of the detector with blue.

rameters were previously introduced at the page 70. An abbreviation F^e is introduced in the equation (4.2) for all factors that are constant for a particular element e.

Equation (4.2) looks like a standard PIXE equation where the pixel yield is calculated from particular sample division into unit voxels. There is however an additional term T that describes the probability that a photon from $(\tilde{k}, \tilde{j}, \tilde{i})$ cell is transmitted through the lens. The transmission function assumes different values for every cell $(\tilde{k}, \tilde{j}, \tilde{i})$.

The system Σ was introduced to ease the description of X-ray absorption along $-\vec{v}$. Its implementation requires to write the lens transmission function in the coordinates of Σ

(refer to the appendix A.1):

$$\begin{aligned} T(x'', y'', z'') &= T_0 \exp\left(-\frac{(x'')^2 + (y'')^2}{2\sigma^2}\right) \\ x'' &= \varsigma \sin\varphi, \\ y'' &= \tau\cos\theta - \varsigma\cos\varphi\sin\vartheta, \\ &\Rightarrow \\ T(\varsigma, \tau, \upsilon) &= T_0 \exp\left(-\frac{(\varsigma\sin\varphi)^2 + (\tau\cos\theta - \varsigma\cos\varphi\sin\vartheta)^2}{2\sigma^2}\right). \end{aligned} \tag{4.3}$$

When all quantities are described in the coordinate system Σ and the cell division of the space established, the principle of reconstruction is similar as the one introduced in [47]. The reconstruction of each sample slice $\varsigma\upsilon$ is performed independently. We begin with the column at fixed $\tilde{j}$ and fixed $\tilde{i}$ at the far edge of the particle being the closest to the detector with the lens. There, the signal is not affected by the sample absorption and the yield at that pixel depends solely on the composition of cells along ς. We calculate the concentrations for all elements in the column under this pixel by fitting the model function (4.2) to the measured yield at each target position. We then move along the row into pixel denoted by $(\tilde{i} - 1)$ at the same value of $\tilde{j}$. The yield at this pixel depends also on the cell occupation in the previous column $\tilde{i}$. Since these quantities are already known, a search for concentrations in the column under pixel $(\tilde{j}, \tilde{i} - 1)$ can take place. We continue along $\vec{v}$ until the edge of the particle is reached and then we move into the next row denoted by $\tilde{j} - 1$ were the procedure is repeated.

4.2 An example – gunshot residue particle

Model for the reconstruction of three-dimensional elemental composition was applied on a gunshot residue micro-particle. The sample was chosen due to its specific shape and size, as well as because it is dominantly composed of only two elements visible in PIXE spectra. To obtain more knowledge about the sample, we gain some basic information from the field of forensics.

The relatively complicated process of shooting a bullet with a high velocity out of a firearm allows for the indication of the shooter specifics from the investigation of the gunshot residues. After the arm is fired, the firing pin strikes the primer cup and the primer mixture is ignited. This rapidly increases temperature and pressure within the cartridge and the primer mixture melts. The supersaturation cause vaporized particles

to condense back onto the liquefied primer surface as droplets. The primer mix ignites the propellant powder and new rapid increase of pressure and temperature occurs and the bullet is expelled from the firearm barrel. After that the temperature and the pressure drops. Rapid cooling causes the liquid droplets to solidify. Gunshot residue (GSR) is therefore principally composed of burnt and unburnt particles from the explosive primer, the propellant, as well as components from the bullet, the cartridge case and the firearm used [107]. When a firearm is discharged, these microscopic particles of GSR are deposited on the hands, clothing, skin and hair of the shooter and are used in police work to prove that someone had fired a gun. GSR particle diameters are usually from few microns to several tens of microns. Gunshot residue particles are routinely examined in the forensic work by SEM together with the EDS method, however several attempts have been made so far in order to use XRF or PIXE method as well [108].

In the traditional ammunition, lead styphnate or lead azide is used as a primer mix together with tetracene or similar organic compounds, nitrocellulose is used as a propellant powder (known as "guncotton"), the oxidizer is most often barium nitrate or strontium nitrate, while for the fuel, antimony sulfide or lead thiocyanate is used. This "traditional" gunshot residues were always composed of lead, strontium and antimony and those three elements were used to characterize GSR [107]. However, in recent years, many manufacturers have turned toward the production of the so called lead-free ammunition, since the health hazard of indoor shooters came in focus. Namely, long training time with traditional ammunition causes severe increase of lead and other toxic heavy metals in the particulate matter in air. Numerous inorganic compounds are now used as a substitution for lead and barium substances and this complicates the characterization of GSR in the forensic science [109]. Our measured particle came from a type of Sintox ammunition, developed by Dynamite Nobel AG, collected from shooters as a research samples in the University of Lausanne. The primer is composed from DDNP (diazodinitrophenol) and tetracene as primary explosives, ZnO_2 as oxidizer [110] and nitrocellulose and Ti metal powder as propellants [111]. The GSR from such ammunition can be composed of some organic compounds, but the majority of the matrix is built from compounds containing Ti and Zn, which are also the only two elements visible by PIXE method (refer to Figures 4.5 and 4.7).

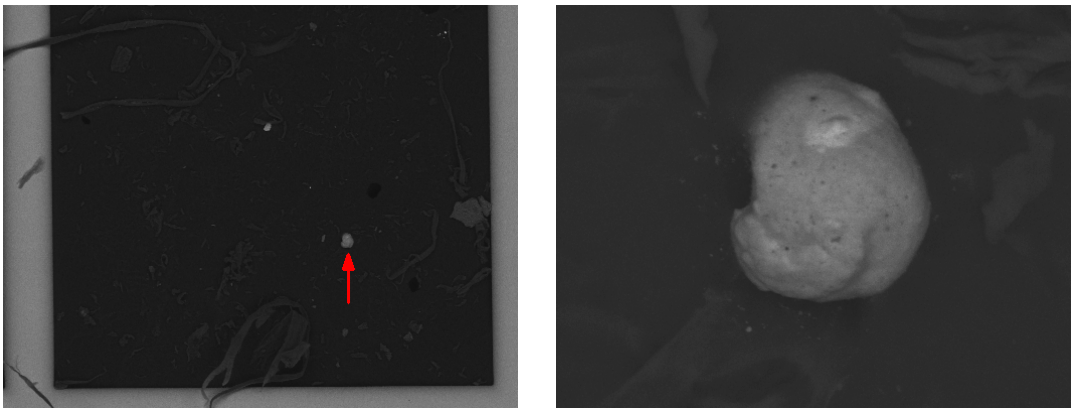

Figure 4.4: SEM images of analyzed particle S14P1. The left one shows the D4 box in copper grid and the particle is identified with red arrow. The magnification was 189x and the image size is approximately 1.4×1.1 mm^2. The right image of the particle was taken with increased magnification of 2840 times and the image size is 92×72 μm^2. Both images were generated by Matteo Donghi from Arma dei Carabinieri, Italy.

4.2.1 Measurements

CF PIXE measurements of a GSR particle were done with the new confocal system using 3 MeV proton beam. GSR particles sit on the SEM stubs with the carbon substrate and a Cu particle finder grid placed on top of the stubs. We constructed a special sample holder to hold the stubs in the microbeam chamber. After the confocal set-up was established and several standards checked, the stub was placed into the confocal set-up and large sample areas of 2×2 mm^2 were scanned and observed by HPGe detector. When individual particles were identified, the holder was brought into position of the selected particle and the whole particle was again scanned over with larger magnification. The particle selected was S14P1 (stub 14, particle 1) from grid box D4. The image taken with SEM is presented in Figure 4.4. The μ-PIXE spectra with strong Ti K_α and Zn K_α line were measured by HPGe detector (Figure 4.5). Corresponding Ti K_α and Zn K_α maps are shown in Figure 4.7.

Before we continued with CF PIXE experiments, we started with a simple analysis of the gunshot residue particle with GeoPIXE software package [101]. Listmode files from HPGe detector were introduced in the code. Before the analysis, the dose normalization factor was obtained for the new retracted position of germanium detector by analyzing the standard samples (Ni, Ti and naval brass targets). This detector was kept about 10 cm away from the standard μ-PIXE measurement position for the majority of CF PIXE experiments in order to keep the count rate of the whole system at a reasonable level of about 500-800 Hz. Several files that represents measurements at different

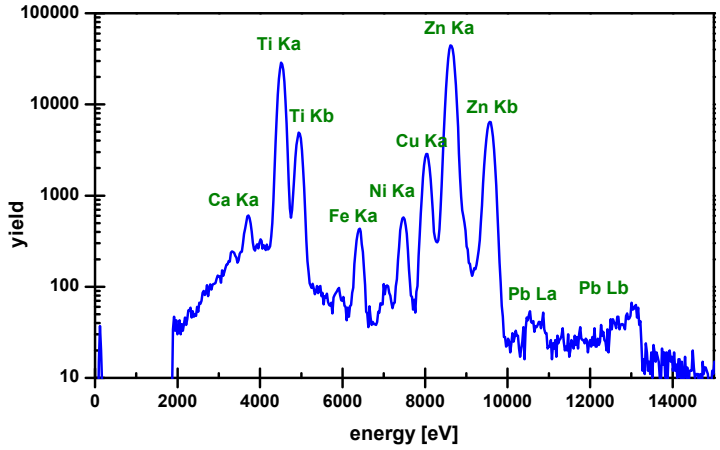

Figure 4.5: Spectrum of GSR S14P1 particle accumulated from the whole $80 \times 80\ \mu m^2$ map measured with HPGe detector. Lines from Ti and Zn are the most prominent spectral features. Pb is also in the sample, but in very small amounts. Fe K_α is induced by Zn X-rays and originates from the chamber walls since for the purpose of this measurements HPGe detector was retracted for 10 cm. Ni K_α originates from fluorescence induced in Ni collimator inside the detector as a parasitic peak, while the signals from Ca and Cu are mostly from the substrate, as they appear scattered around the substrate area.

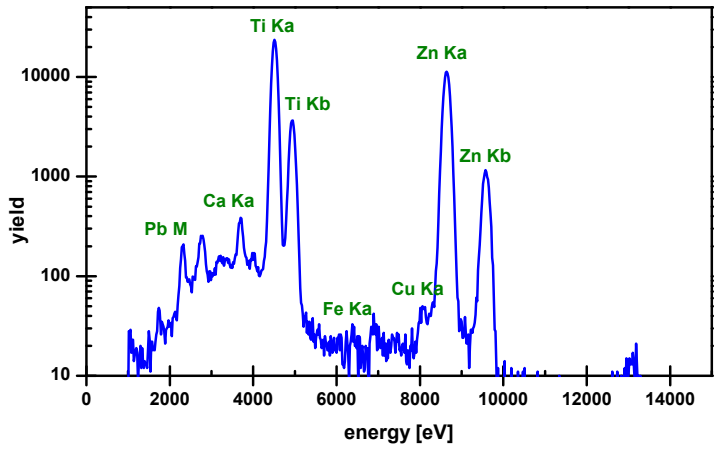

Figure 4.6: Spectrum of GSR S14P1 particle accumulated from the whole $80 \times 80\ \mu m^2$ map measured with SDD detector with lens B. This time, Pb M can be observed. Even if T_0 is smaller for Ti then for Zn, the lens acceptance volume is smaller for Zn and the total accumulated yield for Ti is higher. Lines at 2.8 and 6.9 keV are two Si escape peaks from Ti K_α and Zn K_α lines, and do not represent elements in the sample.

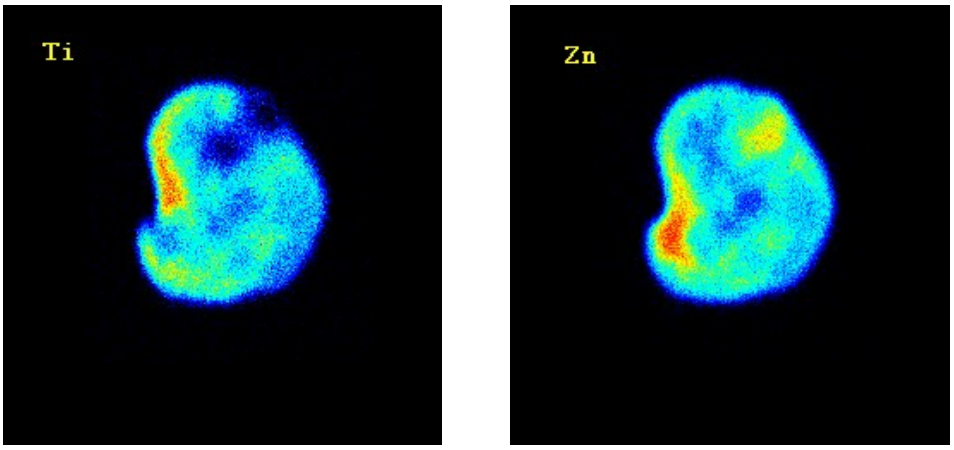

Figure 4.7: Maps of Ti K_α and Zn K_α line from the GSR particle S14P1 measured with germanium detector. Scan size was $80 \times 80\ \mu m^2$.

target positions were analyzed. The corresponding proton dose for measurements were between 0.1 and 0.59 μAs for the whole map. GeoPIXE can calculate lateral elemental concentration distribution from dynamic analysis matrix, however it can't handle three-dimensionally structured samples. Therefore, all samples are treated as flat (with possible surface roughness) and the obtained results are correct only for the considered geometrical case. Results from all three analyzed files were very similar as expected. Matrix was first chosen to be composed of Ti and Zn in 50-50 amount and was later iterated with partial results. Thickness was first set to be 100 μm and later corrected to 30 μm as the calculation of yield in such matrix features very fast decrease at the depths larger than 15 μm. Ti and Zn concentration maps calculated with geoPIXE are shown in Fig. 4.8. Table 4.1 contains the average geoPIXE results from the analysis of S14P1 GSR particle. As expected, the most prominent elements are Ti and Zn, there is also a small amount of Pb. Ca is a contamination since it originates from several areas from the map and not only from the particle.

GeoPIXE analysis yields (12 ± 0.5)% of Ti and (36 ± 1)% of Zn. If we refer to [111], both elements should be in the form of oxides, however, as the ZnO_2 is an oxidant, we can assume it is transformed into the more stable form of ZnO. Molar mass of TiO_2 is 80 and of ZnO 81. Densities are 4.26 g/cm^3 and 5.6 g/cm^3 respectively. In TiO_2 there is 61% of Ti and in ZnO the amount of Zn is 80%. If we assume $1 \times TiO_2 + 1 \times ZnO$ composition, the procentage of Ti atoms in such a mixture is 26%, while of Zn is 45%. The standard μ-PIXE gives smaller amount of both elements. There is a possibility of other organic compounds to exist in such a sample. The smaller concentration may be a result of porosity and un-compactness. The mismatch might came from the geoPIXE

analysis, were the density of pure Zn was used for the matrix density. As this is higher than the densities of both TiO_2 and ZnO, the estimated stopping power and absorption rate are higher then real ones. The assumption of uniformly distributed elements in depth may also bring a wrong result. Another technique must therefore be used to estimate the amount of Ti and Zn in the particle.

As the standard μ-PIXE analysis can only treat a particle by assuming homogeneous in-depth distribution, we applied the CF PIXE method to obtain additional information on its 3D composition. Fifteen 80×80 μm^2 maps of Ti K_α and Zn K_α X-ray yields acquired by the SDD detector and the lens B attached were measured, each at 15 different target positions taken, by the consecutive 10 μm steps along the beam direction (Figure 4.1). Ti and Zn were the only elements to give enough X-ray yield after passing through the lens (Figure 4.6). The whole particle was larger than the lens acceptance volume at both characteristic energies, however this was much more evident with Zn. At first, only the signal from the lower part of the particle was measured. The sequences for Ti and Zn of particle S14P1 are presented in Figures 4.9 and 4.10. Here, the original measured 256×256 pixel maps are already merged into 64×64 pixels and normalized by dividing each new pixel in each map with the corresponding integral number of Au in the RBS chopper spectrum.

Later the target was moved for approximate 20 μm in the $\vec{y}$ direction and the same sequence of maps was measured also for the upper part. However, due to massive shifts of the particle and other problems with data acquired, this sequence was not used for the analysis. This problem, along with others encountered during the applications of CF PIXE method, will be described at the end of this chapter.

4.2.2 Part by part reconstruction

After fifteen X-ray maps were recorded at different sample positions along the beam axis, the signal originating from 4×4 pixels was merged to improve the statistics. In the next step, each pixel was divided with the corresponding Au counts from the chopper to normalize measurement. By checking the map of backscattered particles acquired from the chopper, we proved the assumption that the proton dose areal density does not vary over different regions of the map. Au counts per pixel can thus be acquired by dividing the whole number of Au counts with the number of pixels. The normalized X-ray maps are presented in Figures 4.9 and 4.10. For the quantification purposes, the number of Au counts is multiplied with the dose normalization factor K, obtained from

element	concentration [in mass%]
Ca	400 ppm ± 50 ppm
Ti	12.5% ± 0.5%
Zn	36% ± 1%
Pb	0.17% ± 0.05%

Table 4.1: Averaged elemental concentrations in GSR particle analyzed by GeoPIXE software. The sample is treated as flat.

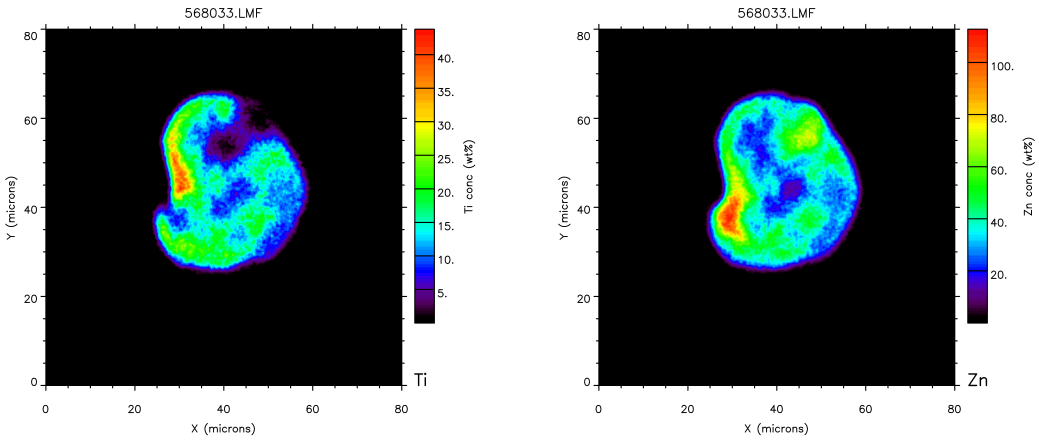

Figure 4.8: Lateral distribution of Ti (left) and Zn (right) concentration in the GSR particle S14P1 as calculated with geoPIXE software from the X-ray map, measured by the germanium X-ray detector. The particle is assumed to be flat and depth distribution of elements is assumed homogeneous. Scan size is $80 \times 80\ \mu m^2$.

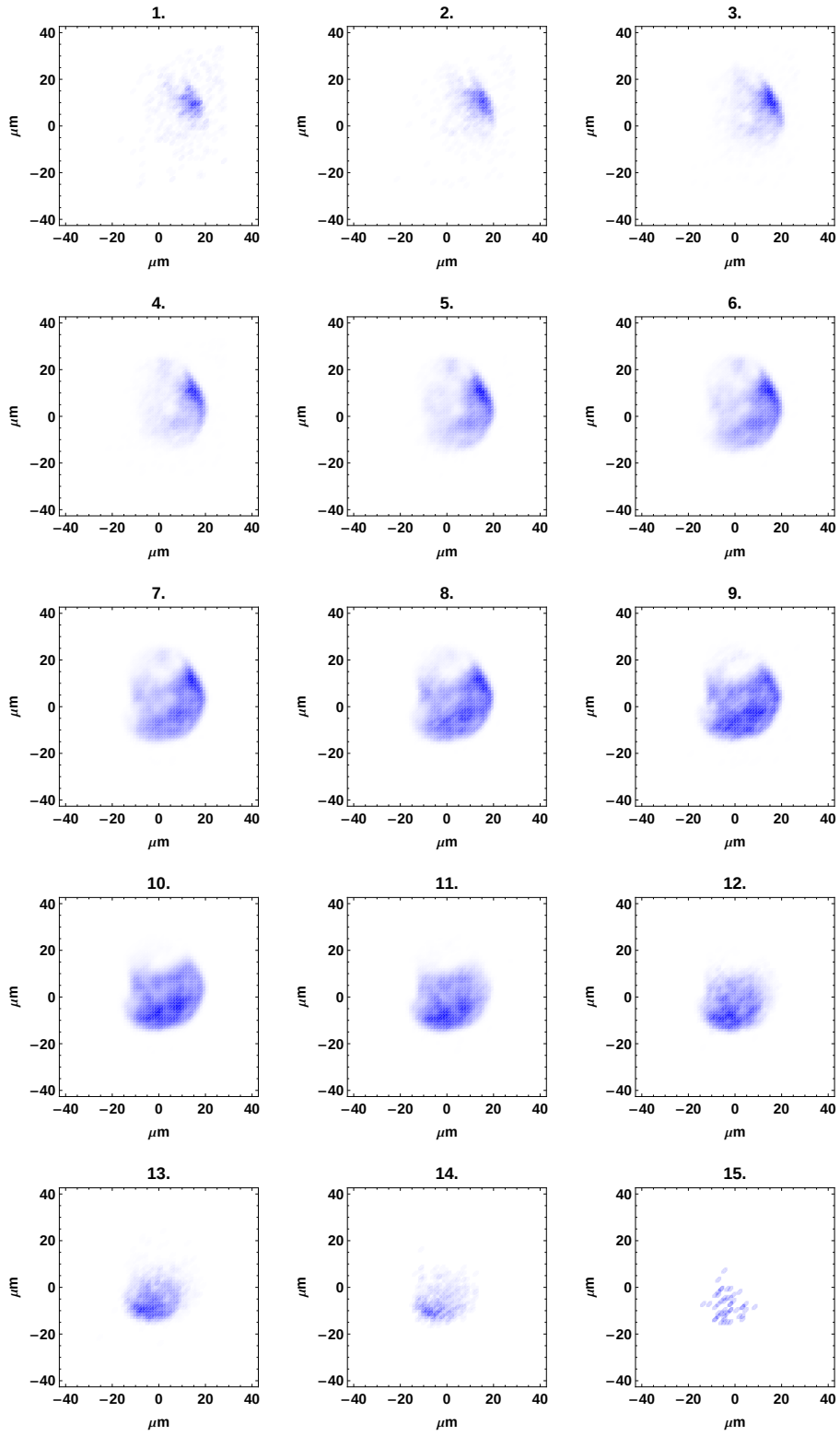

Figure 4.9: A series of Ti maps of a GSR particle S14P1 measured at 15 equidistant target positions along the proton beam. The original 256 × 256 pixel maps is merged into 64 × 64 pixel map to reduce the statistical uncertainty.

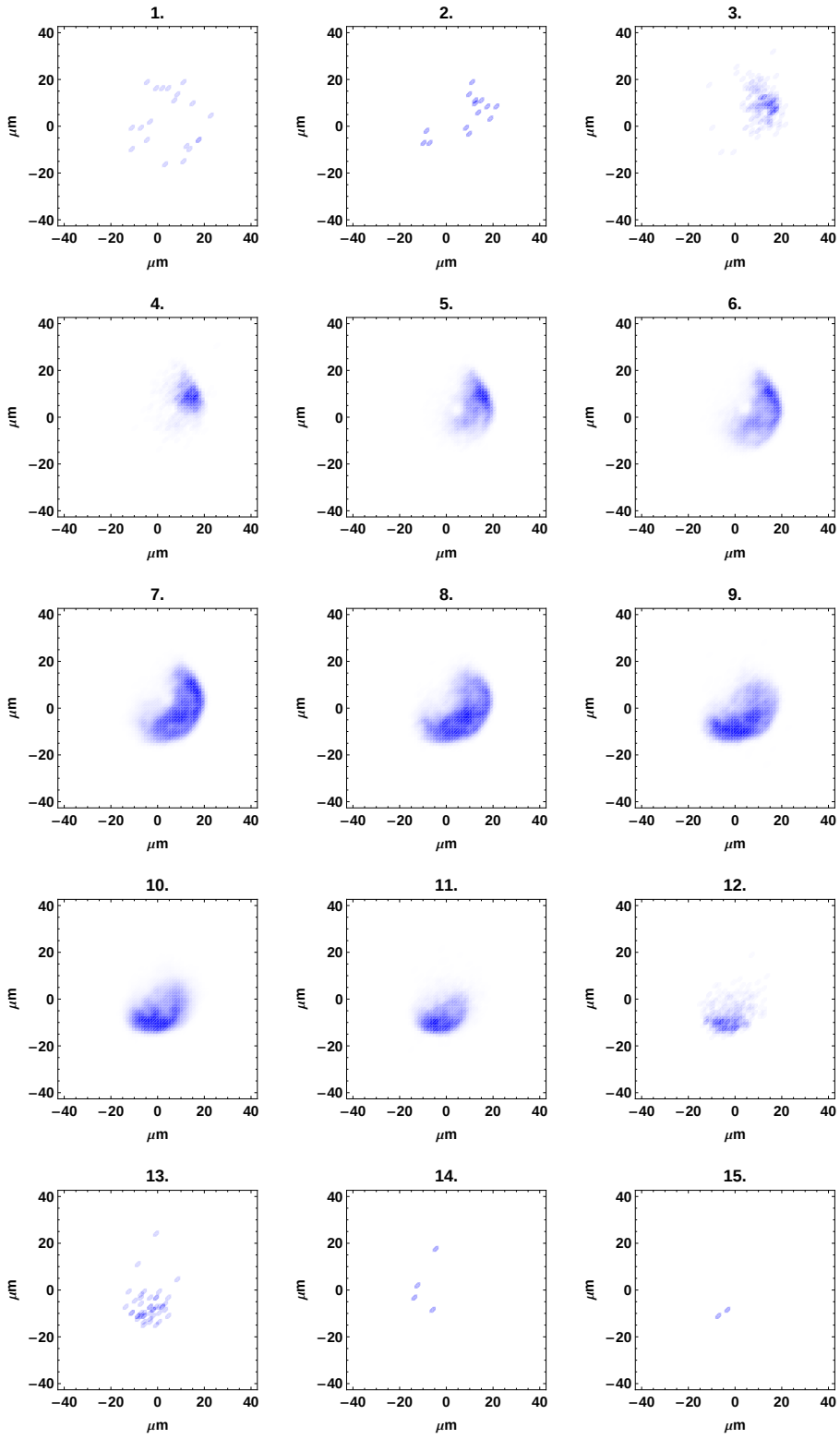

Figure 4.10: A series of Zn maps of a GSR particle S14P1 measured at 15 equidistant target positions along the proton beam. The original 256 × 256 pixel maps is merged into 64 × 64 pixel map to reduce the statistical uncertainty.

measurements of the standard material to get the proton dose in units of As .

The next step was to identify pixels that lie on the same planes $\varsigma\upsilon$ described before. New maps were constructed taking the diagonal lines from the normalized measured maps. The procedure was described on page 88 and the realistic example for one map is demonstrated in Figure 4.11. The first map (4.11 a) presents the eighth normalized map in the particle measuring sequence. The pixels on the diagonals that lay in the same $\varsigma\upsilon$ plane are extracted and the new map is constructed (4.11 b). The origin of the newly introduced index $\tilde{i}$ is still at $j = 0$ (red dashed line) and so in the new map $\tilde{i} = i$, while $\tilde{j}$ runs from 0 to $2j$. The pixel previously marked (i, j) now has the label $(\tilde{j}, \tilde{i}) = (j - i, i)$. To diminish the size of the matrix that describes the map, we removed the first 30 and last 27 empty rows and such truncated maps are then ready for further use (Figure 4.11 c).

Fifteen maps for both Ti and Zn present PIXE yield at fifteen different sample position. For simplicity we can assume that the sample stays fixed at one position and the detector with the lens is moving in parallel to the beam (z) axis. After the space volume is divided into voxels, the particular values of the transmission function are applied for each cell that depends on cell position from $\vec{v}$. As the detector is moving, these values change for every voxel and the yield at each pixel is governed by Eq. 4.2. We can combine all measured maps for a given element in a single 3D matrix, where the two coordinates present x and y, and the third dimension represents the target position in a sequence of moves along the beam. When original maps are transformed into new ones with diagonals as rows (Fig. 4.11), the same type of matrix can be composed as well. In figure 4.12 one horizontal plane of such a 3D matrix is presented for fixed $\tilde{j}$ index ($\tilde{j} = 30$). Rows in this map represent diagonals from the original image that are lying on the mentioned $\varsigma\upsilon$ plane and index $\tilde{i}$ counts pixels in one particular row. Different rows are combined from different measurements obtained at each detector position and are numbered by index n (altogether n=15 target moves were made). If we take a column for a pixel with fixed $\tilde{j}$ and $\tilde{i}$, the two-dimensional graph of normalized photon yield versus the target position is generated – the same as we would obtain from the point scan measurement. One example is in figure 4.12 right, where the graph for pixel $(\tilde{j} = 30, \tilde{i} = 40)$ is presented. The signal depends on cell concentrations of each element in tunnel of cells along ς and on concentration in cells previous to it looking from the lens detector side. It is this sequence of measured yield for every pixel that has to be fitted in course of the reconstruction procedure by Eq. (4.2) with cell element concentrations as free parameters.

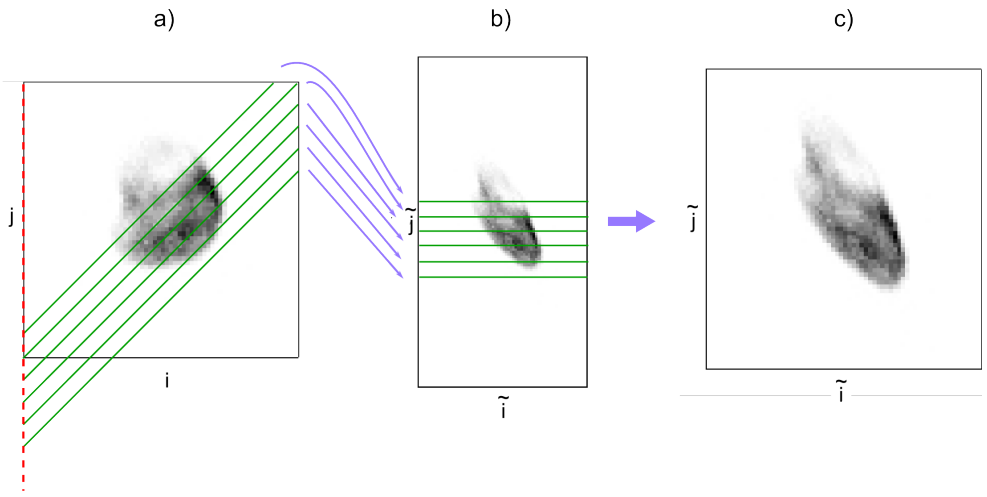

Figure 4.11: A comparison of new maps (b) made of diagonal pixels from original maps (a). Maps, used in the analytical processes (c) are obtained only by removing several empty rows at the beginning and the end of the map.

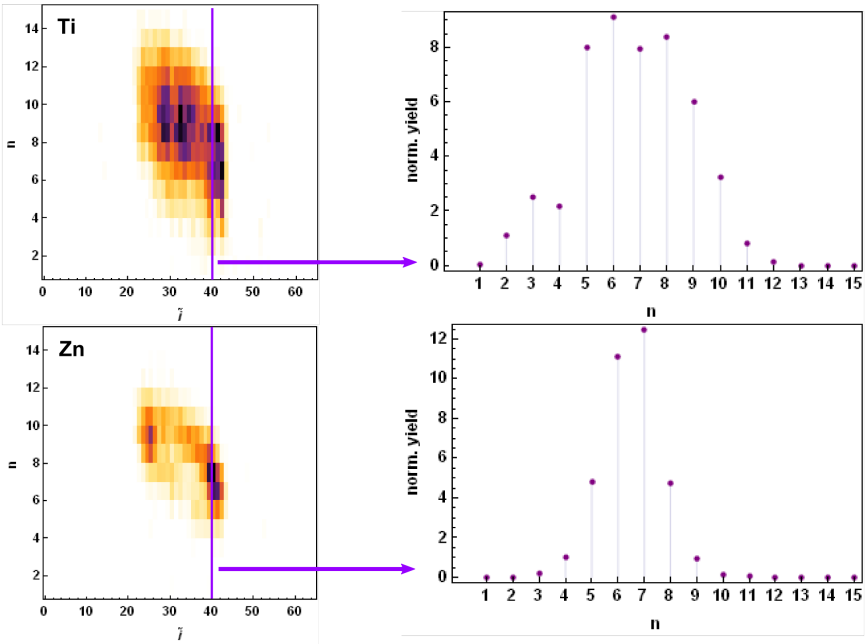

Figure 4.12: Measurements of Ti (above) and Zn (bellow) from the new constructed matrices for different sample positions at one fixed $\tilde{j} = 30$. On the right a column at fixed $\tilde{i} = 40$ is extracted and this data are fitted as described further.

Before the reconstruction, several issues had to be addressed, namely the correct description of energy loss, sample absorption, the lens transmission efficiency and the effect of the secondary fluorescence in the multielemental target within our set-up.

Energy loss

So far we did not look in detail at the energy loss of protons striking the sample. The proton stopping is described by the stopping power or the stopping force $\frac{dE}{dz}$. Apart from the type of the projectile, stopping power depends on type and density of the material, the initial velocity of the projectiles and the binding of electrons encountered along the projectile trajectory [112]. Stopping powers were measured for many different projectiles at different energies for various materials and the data can be found in databases such as the SRIM code [90], which we used in section 2.6. The output of the code is the variation of the stopping power with energy $\frac{\Delta E}{\Delta z}(E)$ for individual elements. The code deals with the compounds too, however in our case, the composition is not known in advance. For compounds and mixtures, a reasonable approximation can be obtained by Bragg's rule, where $\frac{dE}{dz}$ for each element in the compound is weighted by the fraction of electrons belonging to that element [112]. Thus

$$\frac{1}{\rho}\frac{dE}{dz} = \sum_e \frac{w_e}{\rho_e}\left(\frac{dE}{dz}\right)_e, \tag{4.4}$$

where w_i are the fractions by weight of element e in the compound and ρ and ρ_e are densities of the mixture and its fractions respectively. In our case, we have two elements in the sample, Ti and Zn, that contribute the most to the stopping power. They are probably in the form of oxides (Table 4.1), but we do not know for sure in what exact form and of which amount. It is the scope of the analysis to determine the amount of Ti and Zn in the cells. According to the Bragg's rule (4.4), the energy loss of protons in our sample can be therefore written as:

$$\frac{1}{\rho_{\text{full}}}\left(\frac{dE}{dz}\right)_{\text{full}} = \frac{m_{\text{Ti}}}{m_{\text{full}}}\frac{1}{\rho_{\text{Ti}}}\left(\frac{dE}{dz}\right)_{\text{Ti}} + \frac{m_{\text{Zn}}}{m_{\text{full}}}\frac{1}{\rho_{\text{Zn}}}\left(\frac{dE}{dz}\right)_{\text{Zn}}. \tag{4.5}$$

This is rewritten as:

$$\left(\frac{dE}{dz}\right)_{\text{full}} = n_{\text{at}}^{\text{Ti}}\frac{M_{\text{Ti}}}{N_A}\frac{1}{\rho_{\text{Ti}}}\left(\frac{dE}{dz}\right)_{\text{Ti}} + n_{\text{at}}^{\text{Zn}}\frac{M_{\text{Zn}}}{N_A}\frac{1}{\rho_{\text{Zn}}}\left(\frac{dE}{dz}\right)_{\text{Zn}}. \tag{4.6}$$

In Eq. (4.6) $n_{\mathrm{at}}^{\mathrm{Ti}}$ and $n_{\mathrm{at}}^{\mathrm{Zn}}$ present the unknown cell concentrations, M is the molar mass and N_A the Avogadro's constant. $\frac{1}{\rho_{\mathrm{Ti}}}\left(\frac{dE}{dz}\right)_{\mathrm{Ti}}$ and $\frac{1}{\rho_{\mathrm{Zn}}}\left(\frac{dE}{dz}\right)_{\mathrm{Zn}}$ are stopping powers for Ti and Zn in units $\left[\frac{keV}{mg/cm^2}\right]$ that can be calculated from the output of the SRIM code.

The proton range depends on the magnitude of the proton energy loss in the material. In each cell, the proton travels a distance Δz and looses $\Delta E = \left(\frac{dE}{dz}\right)\Delta z$ energy. If proton energy in the previous cell is known as well as elemental concentrations in cell k, the proton energy E_k in cell k can be calculated:

$$E_k = E_{k-1} - \left(\left(\frac{M_{\mathrm{Ti}}}{N_A} n_k^{\mathrm{Ti}} \frac{1}{\rho_{\mathrm{Ti}}} \left[\frac{dE}{dz}\left(E_{k-1}\right)\right]_{\mathrm{Ti}}\right) + \left(\frac{M_{\mathrm{Zn}}}{N_A} n_k^{\mathrm{Zn}} \frac{1}{\rho_{\mathrm{Zn}}} \left[\frac{dE}{dz}\left(E_{k-1}\right)\right]_{\mathrm{Zn}}\right)\right)\Delta z. \tag{4.7}$$

The iterative sequence starts with initial energy E_0, which is known.

Absorption

Equation similar to Bragg's rule (4.4) can be used to express the photon absorption on the way out of the sample. The total absorption coefficient for compounds and mixtures can be calculated from the absorption coefficients of the individual elements e [112]:

$$\frac{\mu_{\mathrm{full}}}{\rho} = \sum_e w_e \frac{\mu_e}{\rho_e}, \tag{4.8}$$

where $\frac{\mu}{\rho}$ is the mass attenuation coefficient, that is again tabulated in various published data libraries like [68, 96, 97].

As a matter of fact, we are interested only in the portion of photons emitted in the direction of the detector. The attenuation of Ti X-rays created in cell $(\tilde{k}, \tilde{j}, \tilde{i}_1)$ and emitted in the direction $-\vec{v}$ is described by the number of photons transmitted and is proportional to:

$$\prod_{\tilde{i}>\tilde{i}_1} \exp\left[-\left(\frac{M_{\mathrm{Ti}}}{N_A} n^{\mathrm{Ti}}(\tilde{k}, \tilde{j}, \tilde{i})\left(\frac{\mu}{\rho}\right)_{\mathrm{Ti1}} + \frac{M_{\mathrm{Zn}}}{N_A} n^{\mathrm{Zn}}(\tilde{k}, \tilde{j}, \tilde{i})\left(\frac{\mu}{\rho}\right)_{\mathrm{Zn1}}\right)\right]\Delta z''. \tag{4.9}$$

Similar expression holds for Zn X-rays:

$$\prod_{\tilde{i}>\tilde{i}_1} \exp\left[-\left(\frac{M_{\mathrm{Ti}}}{N_A} n^{\mathrm{Ti}}(\tilde{k}, \tilde{j}, \tilde{i})\left(\frac{\mu}{\rho}\right)_{\mathrm{Ti2}} + \frac{M_{\mathrm{Zn}}}{N_A} n^{\mathrm{Zn}}(\tilde{k}, \tilde{j}, \tilde{i})\left(\frac{\mu}{\rho}\right)_{\mathrm{Zn2}}\right)\right]\Delta z'', \tag{4.10}$$

for every $\tilde{k}$ and $\tilde{j}$. $\left(\frac{\mu}{\rho}\right)_{\mathrm{Ti1}}$ presents the mass attenuation coefficient of Ti K_α photons with

energy 4.51 keV in a pure Ti target, $\left(\frac{\mu}{\rho}\right)_{\mathrm{Ti2}}$ attenuation coefficient of Zn K_α photons with energy 8.64 keV in a pure Ti target, $\left(\frac{\mu}{\rho}\right)_{\mathrm{Zn1}}$ attenuation coefficient of Ti photons in Zn target and $\left(\frac{\mu}{\rho}\right)_{\mathrm{Zn2}}$ describes mass attenuation coefficient of Zn photons in Zn target. As it can be observed in both equations (4.9) and (4.10), the atomic densities of both elements that are to be determined are again present in both expressions.

Position of the lens transmission function

The lens transmission function (Equation (4.3)) is the key parameter for CF PIXE. We assumed that the center of the two-dimensional Gaussian profile coincides with the origin of the coordinate system S'' (and consequently with the origin of S and Σ system as well). This however is not true. No matter how good the alignment procedure is, there is always some offset regarding the axis υ.

Therefore, we must include in Eq. (4.3) a possible offset of the origin of Gaussian function, i.e. the misalignment vector (a_0, b_0):

$$T(x'', y'', z'') = T_0 \exp\left(-\frac{(x'' - a_0)^2 + (y'' - b_0)^2}{2\sigma^2}\right), \tag{4.11}$$

$$T(\varsigma, \tau, \upsilon) = T_0 \exp\left(-\frac{(\varsigma \sin\varphi - a_0)^2 + (\tau\cos\theta - \varsigma\cos\varphi\sin\vartheta - b_0)^2}{2\sigma^2}\right). \tag{4.12}$$

In principle, a_0 and b_0 are not known a priori and they have to be introduced into the fitting procedure as a pair of global variables, as they stay fixed during all the measurements. However, we can estimate the approximate value of the offset from measured X-ray maps. Equation (2.12) from section (2.4) describes the position of the spot on the map relative to the sample position z and set-up conditions. If the origin of the Gaussian function is not aligned with the z'' axis, then the position of the measured spot moves accordingly. We can follow the same procedure as in section 2.4 with the additional parameters (a_0, b_0) and obtain the following expression of the spot center (x_0, y_0):

$$\begin{aligned} x_0 &= \frac{a_0 - z\sin\varphi}{\cos\varphi}, \\ y_0 &= \frac{b_0}{\cos\vartheta} + \frac{(z - a_0\sin\varphi)\tan\vartheta}{\cos\varphi}. \end{aligned} \tag{4.13}$$

According to the alignment procedure with Ti foil, the focal position should be in the measured map No. 5 referring to the sequence 4.9 and 4.10. However, as the particle

is not flat and there are always some inevitable shifts during sample changing, the accurate focal position is actually displaced and in our case corresponds to the map No. 7 or 8. Normally, the central position is difficult to get from non-uniform maps, however, we can examine how the illuminated area is moving and find an approximate value for the center of the map. If we estimate (x_0, y_0) to be $(10, -5)$ at $z = 0$, then a fairly good guess of the offset can be obtained, $(a_0, b_0) = (8, -1.5)$. This is used as an initial value in the fitting procedure, which finally yields an optimal value of $(12, -1)$ for the offset (a_0, b_0).

Secondary fluorescence

The problem of secondary fluorescence was addressed during the analysis. The question opened, whether the Zn K_α X-rays, with energy of 8.64 keV well above the Ti K absorption edge, may induce important additional share of Ti K_α photons so that a considerable contribution of Ti photon yield does not originate from proton ionization. If the enhancement ratio that describes the number of X-rays of one element arising from fluorescence induced by X-rays of another element relative to the number of proton-induced X-rays of the first element [1] is high, without taking it into consideration the calculated Ti concentrations would be to high. Even further – since we are analyzing our sample with step by step procedure of every cell, the mismatch in the calculated concentration in the first cell would increase an error in the second and so on. In this way, the validation of both elements could be unrealistic.

On the other hand, the inclusion of the secondary fluorescence effect in our model brings serious consequences. The first is loss of plane symmetry of the problem, since photons are emitted isotropically and can induce new photons anywhere in the neighboring cells. Since these cells are in the lens field of view, we would detect secondary fluorescence photons and append it to proton-induced event. Second, the step by step reconstruction starting with the calculation of the concentration in the first edge column and continuing with the use of this values for second column etc. fails, since the secondary fluorescence originating from the first cell can be induced in the "second" or "third" cell as well and it would be rather difficult to consider it during the analysis.

It is known that in PIXE technique the effect of the secondary fluorescence is extremely important only in some special cases when the primary radiation energy is not very high above the absorption edge of the "secondary" elements and when those elements appear in the sample in trace amounts while the "primary" element is in abundance [1, 113]. As it turned out, the ratio $\frac{N^{\mathrm{Ti}}_{\mathrm{sec.fl.}}}{N^{\mathrm{Ti}}_{\mathrm{prot}}}$ was found to be around a few percent and so

we did not need to include this connection into the reconstruction procedure. However, as the topic may be important in some cases, some basic procedure of this calculation can be found in appendix B.

The reconstruction code

When all had been summed up, we wrote a simple program in Mathematica® [114] to extract unknown elemental concentrations from X-ray maps. The analysis like this, the three-dimensional reconstruction of elemental concentrations in a sample from a series of CF PIXE maps, in principle requires a sophisticated software that would include all features from PIXE analysis, the properties of the X-ray optics used and the reconstruction procedure. Only then would such analysis be relatively quick and effective for applicative purposes. As the development of this kind of software was beyond the scope of this work, we used the described procedure point by point and partly automatize it with the use of the appropriate algorithms.

Space in ς direction was divided into 12 cells, each was $\Delta\varsigma = \Delta z = 10$ μm long. Therefore, the combed area of interest in ς direction was 120 μm. The edge of the particle was assumed to be in the fourth cell, where we placed the origin, $\varsigma = z = 0$. Cells closer to the proton beam had a negative sign, the ones further away a positive sign. The cells in τ direction were much more narrower and followed the partition of pixels in a map. We divided the τ axis in 64 cell, $\Delta\tau = \Delta y = 1.28$ μm wide. Similar holds for axis υ, where the cells were $\Delta\upsilon = \Delta z'' = \frac{\Delta x}{\cos\vartheta \sin\varphi}$ wide. $\Delta x = \Delta y = 1.28$ μm.

σ_{Ti} and σ_{Zn} required for the description of the lens transmission were taken from the FWHM measurements of the standard material (Figure 2.18) and were 14.0 and 8.1 μm, respectively. The same goes for T_0; the value for Ti was 0.1 and for Zn 0.17. It is worth to mention that both σ-s of the lens acceptance volume were taken constant for all measurements and $\sigma(z'')$ was approximated by its value at $z'' = 0$. The broadening of the lens field of view with the distance from the focal point (Figure 2.17) was therefore neglected.

Other numerical values of quantities that appear in Equation (4.2) for both elements are gathered in Table 4.2. The values of proton stopping powers at different energies were taken from [90], while the ionization cross-sections were extracted from [93].

We made 15 scans ($n = 15$) at equidistant positions along the beam with $z_0 = 10$ μm step (Figure 4.1). The difference between each scan is that the value of the transmission function for a given cell changes. In principle, we had to assign the proper

quantity	Ti	Zn
σ [μm]	14.0	8.1
T_0	0.1	0.17
$\Delta\Omega$ [rad]	0.06	0.06
ϵ	1	1
η	0.94	0.99
K [μAs/count]	$3.3 \cdot 10^{-6}$	$3.3 \cdot 10^{-6}$
ω	0.214	0.474
b	0.91	0.90
M [g/mol]	47.9	65.4
$\frac{\mu}{\rho}$ [cm^2/g] (in Ti)	108	166
$\frac{\mu}{\rho}$ [cm^2/g] (in Zn)	280	47

Table 4.2: Numerical values of different quantities required in the quantitative CF PIXE analysis for both elements Ti and Zn used in the process.

PIXE equation (4.2) to every cell and multiplied it with adequate value of T for every position.

The procedure goes as follows:

1. For every column at fixed $\tilde{j}$ and $\tilde{i}$ the occupation of Ti and Zn is assumed to be a lists of numbers ($n_{\text{Ti }1}, n_{\text{Ti }2}, n_{\text{Ti }3}, \ldots, n_{\text{Ti }12}$) and ($n_{\text{Zn }1}, n_{\text{Zn }2}, n_{\text{Zn }3}, \ldots, n_{\text{Zn }12}$). n_i have units of [10^{22} cm^{-3}] and they are treated as free parameters during the analysis.

2. The data from each column at fixed $\tilde{j}$ and $\tilde{i}$ (from figure 4.12) for Ti and Zn are put together (Figure 4.13) in order to have one set of data to fit.

3. The measured Ti and Zn data yield is divided by F^{Ti} and F^{Zn}, respectively.

4. Transmission function for Ti and Zn is written for every cell and for every n.

5. Proton beam energy in every cell is governed by the equation (4.7), being a function of atomic concentrations of both elements in all previous cells. The ionization cross-section is then determined for that energy and enters into the fit as a function of atomic concentrations.

6. Absorption of photons emitted in every cell is determined via equations (4.9) and (4.10) and is a function of the occupation of cells at columns under the same $\tilde{j}$ and $\tilde{i} - N$. Absorption for the first full columns is 0 by definition.

7. A model is made, composed of multiplication of all quantities described above

(ion.cross-section∗occupation∗transmission∗absorption) and the values of n_i enter the fit as free parameters in order to describe the measured data. Fit is controlled by the minimization of the merit function $\chi^2 = \sum_n \left(\frac{Y_n^e - Y(\text{model})}{\sigma_n}\right)^2$, where σ_n is the standard deviation of each data point Y_n^e [115].

On page 107 an example of a model fit of the experimental data is presented. Figure 4.13 presents data under one pixel at $\tilde{j} = 40, \tilde{i} = 45$. Fifteen measured points presenting Ti K_α line were first normalized as described before and divided by factor F^{Ti}, while the normalized yield from fifteen positions for Zn K_α line were divided by F^{Zn}. Both data were put together in such a way, that $n \in [1, 15]$ on the abscissa from the graph present measurements of Ti yield of each successive sample move, while $n \in [16, 30]$ represent measurements of Zn K_α yield. This data set is now dependent on 28 parameters of concentration of Ti and Zn in every of the 12 cells the depth of the space was divided into. However, as it is safe to assume the particle is not so large, several cells are empty and their concentrations are 0. The blue line presents a fit of the data with the above mentioned model (together with the included X-ray transmission through columns under $\tilde{j} = 40, \tilde{i} = 46, 47, 48$). The concentrations in units of 10^{22} cm^{-3} that return the best result for this particular example are listed in the table next to Figure 4.13.

In Figure 4.14, the same data under pixel ($\tilde{j} = 40, \tilde{i} = 45$) is presented. This time, the model function presented with dashed red line is deliberately calculated with wrong assumptions for values of the concentrations within cells. If we assume both Ti and Zn are present in the same accumulative amount as it was obtained before, but only one cell (5.) contains the whole amount, the obtained function can not describe the measured signal accurately.

4.2.3 Results

As observed from Figures 4.9 and 4.10, we were unable to detect the whole particle with SDD lens detector in a single sweep of the object along the beam direction. The size of the measured part was governed with the lens FWHM of Zn K_α photons. So, only the lower part of the object was measured and consequentially reconstructed. If we refer to Fig. 4.11a, $\tilde{j}$ counts diagonal lines from the lower edge of the particle (where $\tilde{j} = 54$) up. With the reconstruction procedure described above, we obtained a set of concentrations of Ti and Zn in every cell up to $\tilde{j} = 29$. From this line on, the transmission of the lens for Zn photons is already too low to give significant number

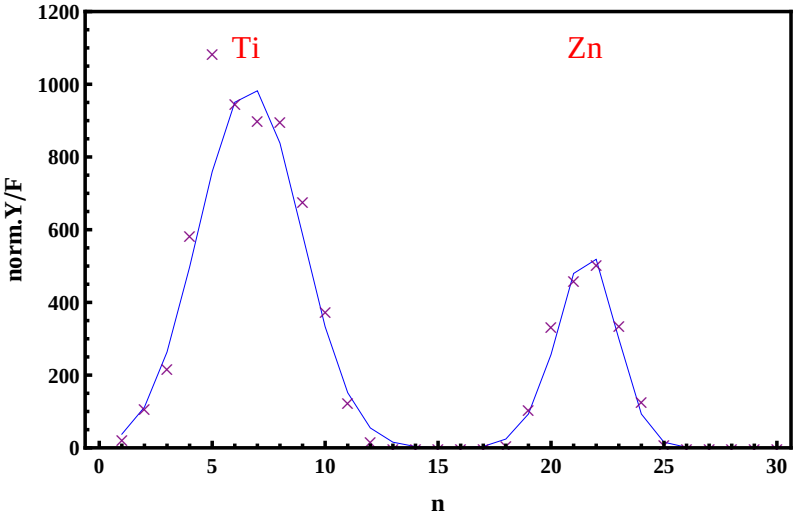

$\tilde{k}$	Ti	Zn
1	0	0
2	0	0
3	0	0
4	0.37	0.3
5	0	1.8
6	0.41	0.25
7	0	0.2
8	0	0
9	0	0
10	0	0
11	0	0
12	0	0

Figure 4.13: Modified measured data under pixel ($\tilde{j} = 40, \tilde{i} = 45$) and a fitted function (blue line) with concentrations (in units of 10^{22} cm^{-3}) of Ti and Zn presented in the table on the right.

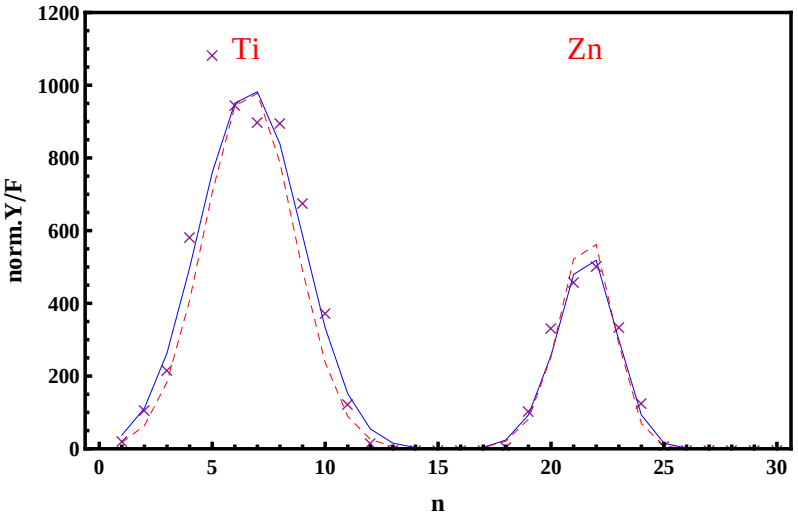

$\tilde{k}$	Ti	Zn
1	0	0
2	0	0
3	0	0
4	0	0
5	0.8	2.5
6	0	0
7	0	0
8	0	0
9	0	0
10	0	0
11	0	0
12	0	0

Figure 4.14: Measured data under the same pixel ($\tilde{j} = 40, \tilde{i} = 45$) and the difference between previously fitted function (blue line) and the one calculated from different set of concentrations of both elements (red dashed line) presented in the table on the right (in units of 10^{22} cm^{-3}).

of counts in the map.

The raw result is a set of matrices for every $\tilde{j}$ with index $\tilde{i}$ presenting rows and $\tilde{k}$ presenting columns. Every matrix has twelve $\tilde{k}$ values, however we always started the procedure at $\tilde{i}$ where a statistically significant number of counts were encountered and stopped considering the same criteria. This means that the reconstruction took place only within the particle. As the particle is of irregular shape, the number of $\tilde{i}$ with occupied cells differ for every $\tilde{j}$. Each matrix contains concentrations of Ti and Zn in every cell in the coordinate system Σ in units of 10^{22} cm^{-3}. There are 26×2 such matrices. One example for Ti and Zn is presented in Tables 4.3 and 4.4.

The matrices describe the cell concentration in system Σ. Every voxel $(\tilde{k}, \tilde{j}, \tilde{i})$ can be represented in coordinates by $(\Delta\varsigma(\tilde{k} - \frac{1}{2}), \Delta\tau(\tilde{j} - \frac{1}{2}), -\Delta\upsilon(\tilde{i}^{-}\frac{1}{2}))$. To obtain these coordinates in system S, transformation rules described in Appendix A.1 must be applied. Therefore, the centers (x_c, y_c, z_c) of each reconstructed cell in system S have coordinates:

$$\begin{aligned} x_c &= \frac{\Delta x}{\cos\vartheta \sin\varphi}\left(\tilde{i} - \frac{1}{2}\right)\cos\vartheta \sin\varphi \\ y_c &= \Delta y\left(\tilde{j} - \frac{1}{2}\right) - \frac{\Delta x}{\cos\vartheta \sin\varphi}\left(\tilde{i} - \frac{1}{2}\right)\sin\vartheta \\ z_c &= \Delta z\left(\tilde{k} - \frac{1}{2}\right) - \frac{\Delta x}{\cos\vartheta \sin\varphi}\left(\tilde{i} - \frac{1}{2}\right)\cos\vartheta \cos\varphi \end{aligned} \tag{4.14}$$

The results are presented on pages 113-117 as a series of slices at 27 different positions of x, each separated by $\Delta x = 1.28$ μm. Figure 4.15 shows the slice position. In order to fully understand the results, Figure 4.15 should be used as a reference. Coordinates x match the ones on the measured maps on Figures 4.9 and 4.10. The first edge of the particle is at around $x = 29$ μm and goes all the way to $x \approx 60$ μm. The coordinate y from the reconstructed maps has an offset regarding the measured maps, $y = 0$ on the reconstructed map matches $y = 40$ μm on the measured map. The coordinate z is somehow arbitrary and the negative sign only reflects the choice of the origin along ς direction. Care should be taken in the interpretation, as the y axis is presented on the abscissa and z on the ordinate axis. The color shade of the cell is related to the concentration of the element in the cell, starting from 0 (white) toward the maximum concentration of Ti $0.95 \cdot 10^{22}$ cm^{-3} (blue) and Zn $4.3 \cdot 10^{22}$ cm^{-3} (black).

We can assume with fair accuracy that Ti is in the form of TiO_2, while the original ZnO_2 is transformed into a standard ZnO. Taking into account densities of both compounds ($\rho_{TiO2} = 4.26$ g/cm^3 and $\rho_{ZnO} = 5.6$ g/cm^3), we can calculate the number of Ti and

	1	2	3	4	5	6	7	8	9	10	11	12
28	0	0	0	0	0.	0.06	0	0	0	0	0	0
29	0	0	0	0.02	0.23	0.37	0	0	0	0	0	0
30	0	0	0	0.26	0.3	0.41	0	0	0	0	0	0
31	0	0	0	0.37	0.	0.41	0	0	0	0	0	0
32	0	0	0	0.37	0.	0.25	0	0	0	0	0	0
33	0	0	0.05	0.32	0.	0.18	0	0	0	0	0	0
34	0	0	0.09	0.37	0.	0.18	0	0	0	0	0	0
35	0	0	0.21	0.29	0.07	0.05	0	0	0	0	0	0
36	0	0	0.36	0.25	0.06	0.05	0	0	0	0	0	0
37	0	0	0.38	0.25	0.08	0.1	0	0	0	0	0	0
38	0	0.07	0.45	0.1	0.29	0.1	0	0	0	0	0	0
39	0	0.1	0.44	0.09	0.32	0.07	0	0	0	0	0	0
40	0	0.05	0.44	0.09	0.32	0.	0	0	0	0	0	0
41	0	0.05	0.49	0.15	0.32	0.	0	0	0	0	0	0
42	0	0.18	0.48	0.16	0.3	0.	0	0	0	0	0	0
43	0	0.45	0.	0.35	0.05	0.	0	0	0	0	0	0
44	0	0.37	0.	0.32	0.05	0.	0	0	0	0	0	0
45	0	0.32	0.	0.3	0.05	0.	0	0	0	0	0	0
46	0.12	0.2	0.03	0.15	0.	0.	0	0	0	0	0	0
47	0.05	0.15	0.08	0.03	0.	0.	0	0	0	0	0	0
48	0	0.03	0.	0.04	0.	0.	0	0	0	0	0	0

Table 4.3: An example of calculated titanium concentrations in cells under diagonal $\tilde{j} = 40$. Rows corresponds to different $\tilde{i}$, while columns count cells in depth. The concentrations are given in units 10^{22} cm^{-3}.

	1	2	3	4	5	6	7	8	9	10	11	12
28	0	0	0	0	0.1	0.14	0	0	0	0	0	0
29	0	0	0	0	1	0.9	0	0	0	0	0	0
30	0	0	0	0.3	1.8	0.4	0.2	0	0	0	0	0
31	0	0	0	0.3	1.8	0.25	0.2	0	0	0	0	0
32	0	0	0	0.6	1	0.15	0.1	0	0	0	0	0
33	0	0	0.1	0.7	0.8	0.1	0.1	0	0	0	0	0
34	0	0	0.3	0.6	1.1	0.1	0.1	0	0	0	0	0
35	0	0	0.8	0	1.7	0.	0	0	0	0	0	0
36	0	0.1	1.3	0.2	1	0.1	0	0	0	0	0	0
37	0	0.1	1.1	0.5	1	0.1	0	0	0	0	0	0
38	0	0.1	1.1	0.6	1.	0.2	0	0	0	0	0	0
39	0	0.1	1.2	0.6	1.1	0.2	0	0	0	0	0	0
40	0	0.1	1.05	0.6	1.1	0	0	0	0	0	0	0
41	0	0.2	1.1	0.7	0.8	0	0	0	0	0	0	0
42	0	0.4	1.3	1	0.5	0	0	0	0	0	0	0
43	0	0.8	1.6	1	0.3	0	0	0	0	0	0	0
44	0	0.8	1	1.2	0	0	0	0	0	0	0	0
45	0	1.7	0	1.1	0	0	0	0	0	0	0	0
46	0	1.3	0.7	0.5	0	0	0	0	0	0	0	0
47	0	0.6	0.4	0	0	0	0	0	0	0	0	0
48	0	0.08	0.15	0	0	0	0	0	0	0	0	0

Table 4.4: An example of calculated zinc concentrations in cells under diagonal $\tilde{j} = 40$. Rows corresponds to different $\tilde{i}$, while columns count cells in depth. The concentrations are given in units 10^{22} cm^{-3}.

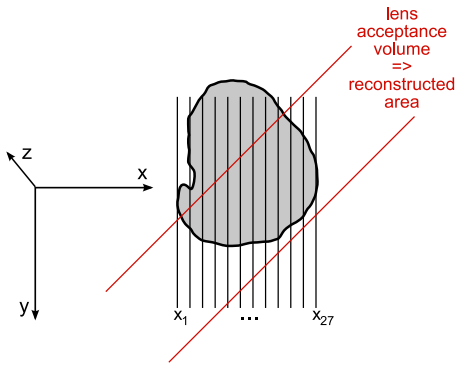

Figure 4.15: A scheme of planes yz at different fixed x as presented in Figures 4.16-4.21. The distance between x_i and x_{i+1} is 1.28 μm. Red lines present the reconstructed area. Proton beam was perpendicular to the xy plane.

Zn atoms that should exist in every unit cell that has a volume $16.4 \cdot 10^{-12}$ cm^3. In TiO_2 there is 61% of Ti and in ZnO the amount of Zn is 80%. Therefore, if our cell would be occupied with pure ZnO, there should have been $5.5 \cdot 10^{11}$ Zn atoms per cell and viceversa, if only TiO_2 would exist, the number of Ti atoms in such cell would have been $3.2 \cdot 10^{11}$. The average concentration of Zn atoms obtained in the analysis is around $1.7 \cdot 10^{22}$ cm^{-3} and Ti around $0.25 \cdot 10^{22}$ cm^{-3}. This yields $2.8 \cdot 10^{11}$ Zn atoms and $4.1 \cdot 10^{10}$ Ti atoms per unit cell or 51% and 13% of their pure values if compounds are considered, respectively. Now we can verify that the assumption made on page 93, $1 \times TiO_2 + 1 \times ZnO$ composition of the GSR particle, is incorrect. The porosity of the material and the organic compound leftovers are present in the particle that contibute to a lower mass procent of both compounds then expected.

Simultaneously with the lens detector, data acquisition of X-ray maps were recorded with the HPGe detector, positioned on the other side of the target in the horizontal plane. The reconstructed object concentrations were used to simulate the elemental map measured with the Ge detector in order to check the results. The angle between the axis of HPGe detector and the proton beam direction is 45° as described in section 2.1. The detector was retracted from its standard μ-PIXE measuring position for almost 10 cm and the detector solid angle was 5.5 msr. The dose was determined from the measurements of standard material as described before and the proton dose used for the simulation was $3.7 \cdot 10^8$ protons/pixel. The transmission of kapton absorbers placed before the detector was 0.51 for Ti K_α photons and 0.9 for Zn K_α. Detector efficiency can be safely regarded as 1 for both photon energies (in reality it is around 0.96 for 4.5

keV and 0.99 for 8.6 keV). The atomic factors (ionization cross-section, fluorescence yield, branching ratio etc.) are the same as for the measurements with the lens detector. Moreover, there is no X-ray lens in front of the germanium detector, so the "lens" transmission T is 1.

The procedure for this backward calculation of the yield is in principle straightforward. The known atomic concentrations in the coordinate system S are used first to calculate proton energy loss and thus the corresponding ionization cross-section, and this is then corrected with photon absorption along the Ge detector axis. As the detector lies in the y plane, the excitation-emission processes take part in the yz plane. We keep the cell division, but we had to divide the cells in z direction even further in order to calculate the absorption in a more precise way. Namely, the absorption "path" is directed at an angle 45° with respect to the proton direction. We must therefore know the occupation of cells along this path. The easiest way to approach this problem is to divide each of the unit cells into eight smaller ones in z direction, assuming each newly formed cell has the same atomic concentration as the former big one. In this way, every obtained cell has now a volume of $1.28 \times 1.28 \times 1.25\ \mu\text{m}^3$ and can be assumed with only small error as a cube. In this way, the path photons travels in each cell on their way back to the detector can be approximated with a diagonal of a yz cell rectangle, namely $l_1 = 1.8\ \mu\text{m}$.

Employing such a procedure, the Ti and Zn X-ray maps taken by the germanium detector without the lens can be simulated. The comparison is presented in Figure 4.22. Matching areas with higher or lower number of counts can be detected in both maps. Only the area marked by yellow circle in Ti map is calculated to have much higher yield as in the measured map but this can be easily understood, as the absorption of photons from this area happens in the cells left from it and these part was not analyzed by CF PIXE, so that the concentration is not known and the absorption effect could not be calculated. This tends to overestimate the yield. Similar happens with Zn in the same part of the map, however as Zn K_α photons have higher energy and are less affected by absorption, this difference is smaller.

With CF PIXE, three-dimensional elemental distribution can be obtained, providing extra in-depth resolved information about the composition of our gunshot residue particle. Our analysis shows how Ti and Zn are distributed within the reconstructed part of the object. The lower part (from $y = 0$ down in our reconstructed maps) is relatively heavily occupied with both elements, while there are some regions of lower concentrations and practically an empty space in the particle center. The central "hole" is

visible also in the measured maps (Figure 4.7) and is signaled also by GeoPIXE analysis of the HPGe map (Figure 4.8). However, only from the HPGe map, one can not deduce a strong abundance of both elements in the lower part of the particle. Figure 4.23 presents a map of mean concentrations along z at each (x,y) pixel. These are the "real" images if the particle with the same number of atoms of both elements would be considered flat and 40 μm thick. These can be compared to the concentration maps, produced by GeoPIXE code (page 95). The empty parts more or less coincide, however the occupancy in the lower part of the particle is underestimated by GeoPIXE. In our reconstruction, we failed to produce high concentrations (visible also in the mismatch in Figure 4.22) in the left edge of the particle. Two reasons may explain that effect. One is the low tail of the lens transmission function, and the other a slightly wrong origin used for the cell division. The assumption of the edge of the particle being in the fourth cell (page 104) turned out to be wrong and this resulted in the misfit of columns under the last few pixels for $\tilde{j} = 31, 30, 29$. The last issue could be corrected, but the whole procedure should start from the beginning. As these pixels are really only at the far edge of our reconstructed part, we did not repeat the whole calculations again.

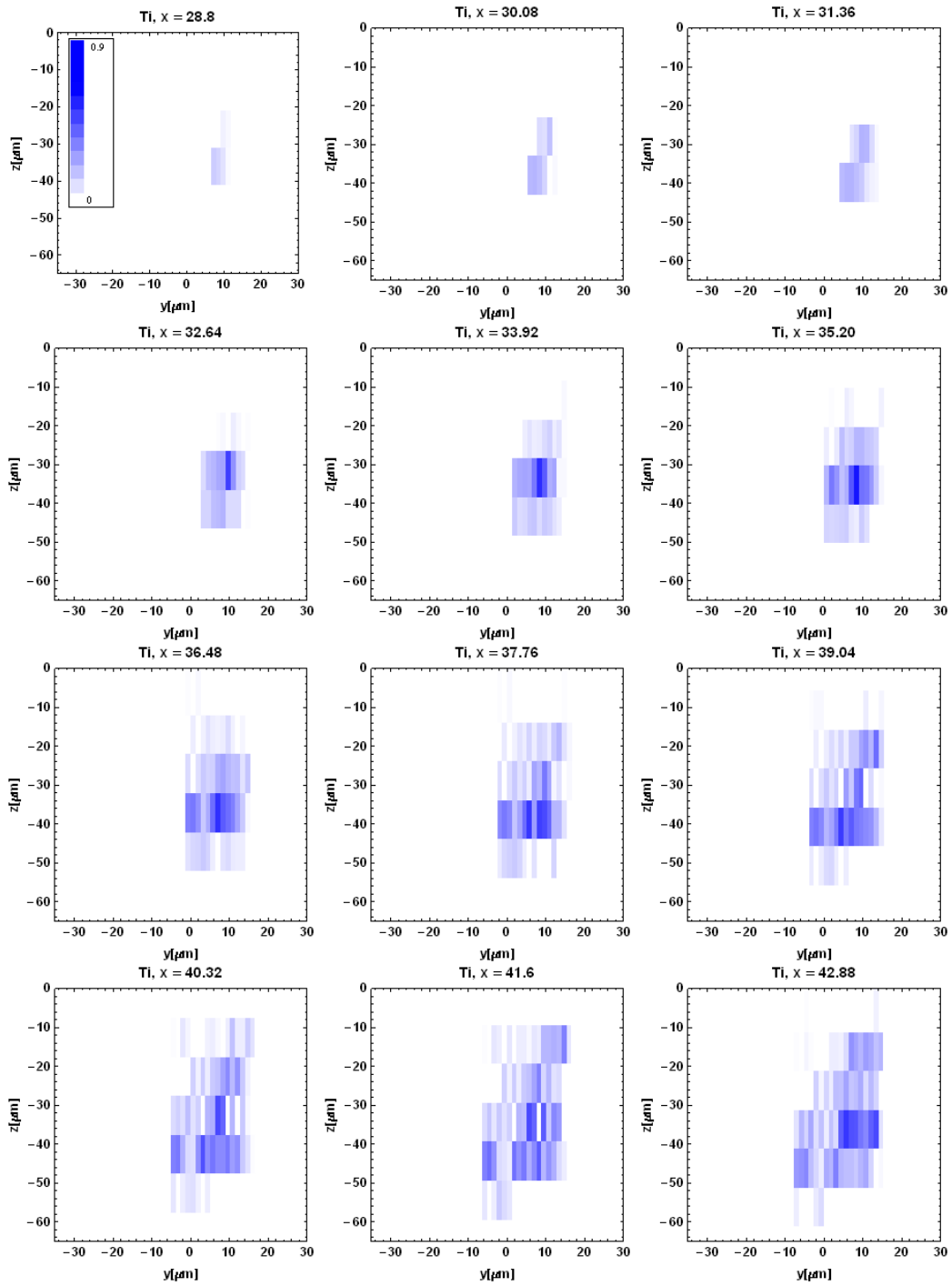

Figure 4.16: The first 12 slices at 12 different x positions from $x = 28.8$ μm to $x = 42.9$ μm of the reconstructed Ti distribution within the lower part of the GSR particle.

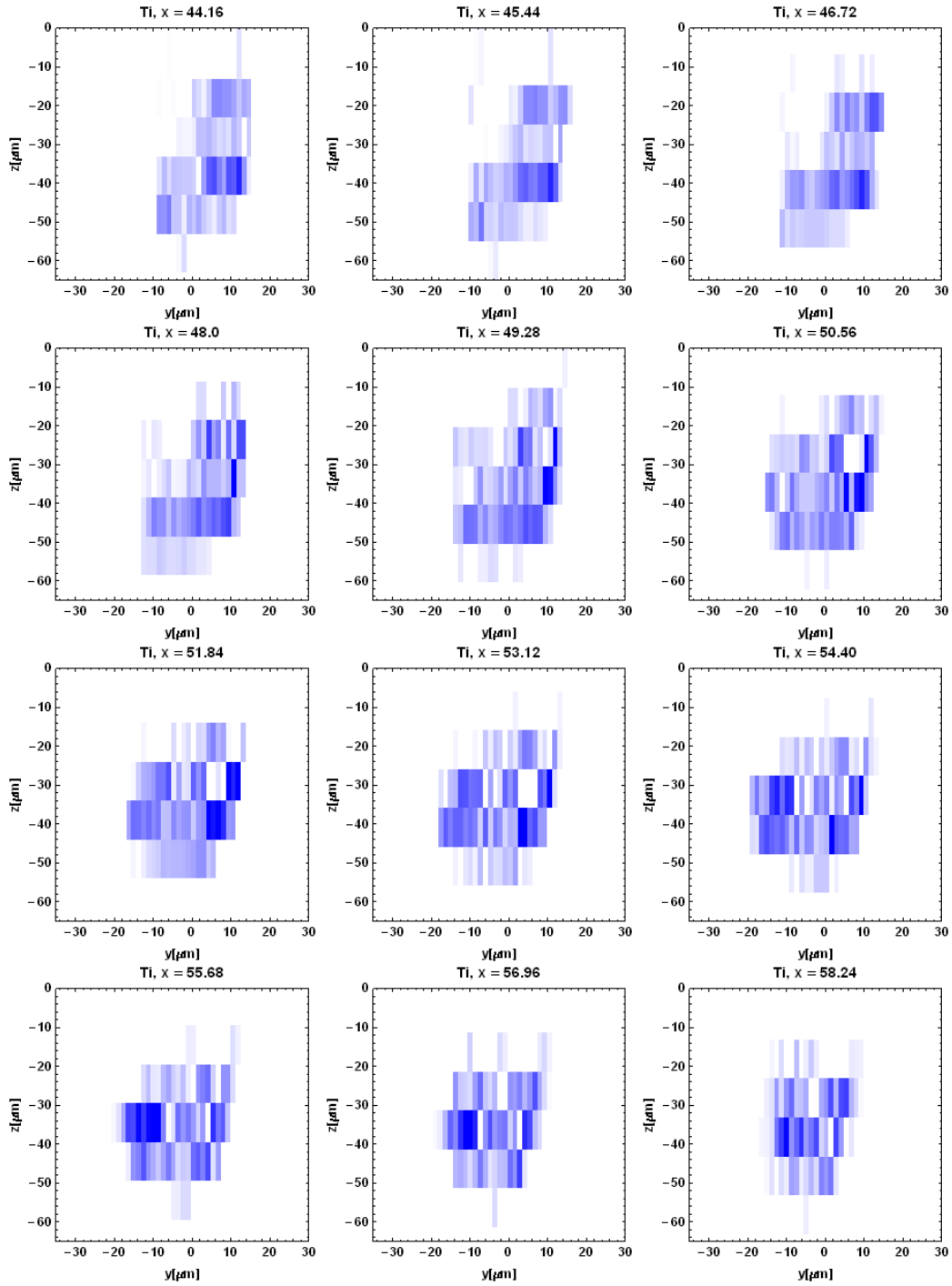

Figure 4.17: Next 12 slices from $x = 44.2$ μm to $x = 58.2$ μm of the reconstructed Ti distribution within the lower part of the GSR particle.

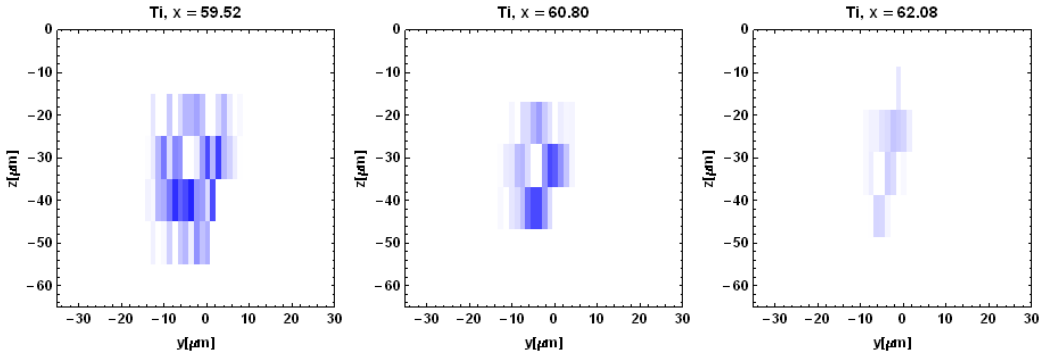

Figure 4.18: The last three slices from $x = 59.5$ μm to $x = 62.1$ μm of the reconstructed Ti distribution within the lower part of the GSR particle.

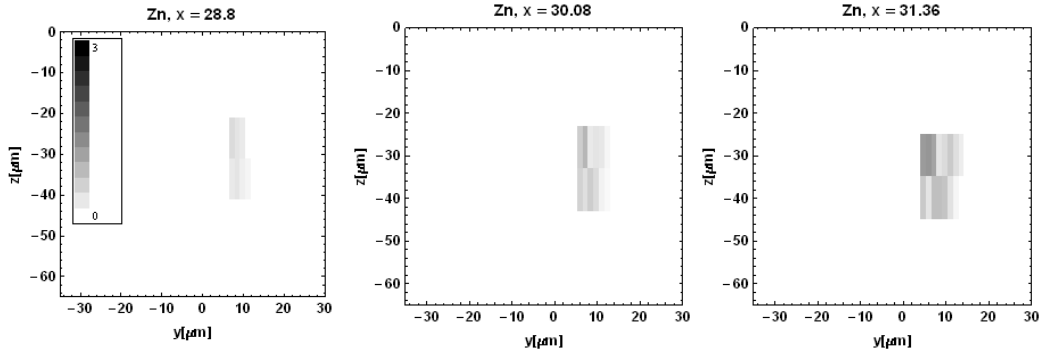

Figure 4.19: The first 3 slices at three different x positions from $x = 28.8$ μm to $x = 31.4$ μm of the reconstructed Zn distribution within the lower part of the GSR particle.

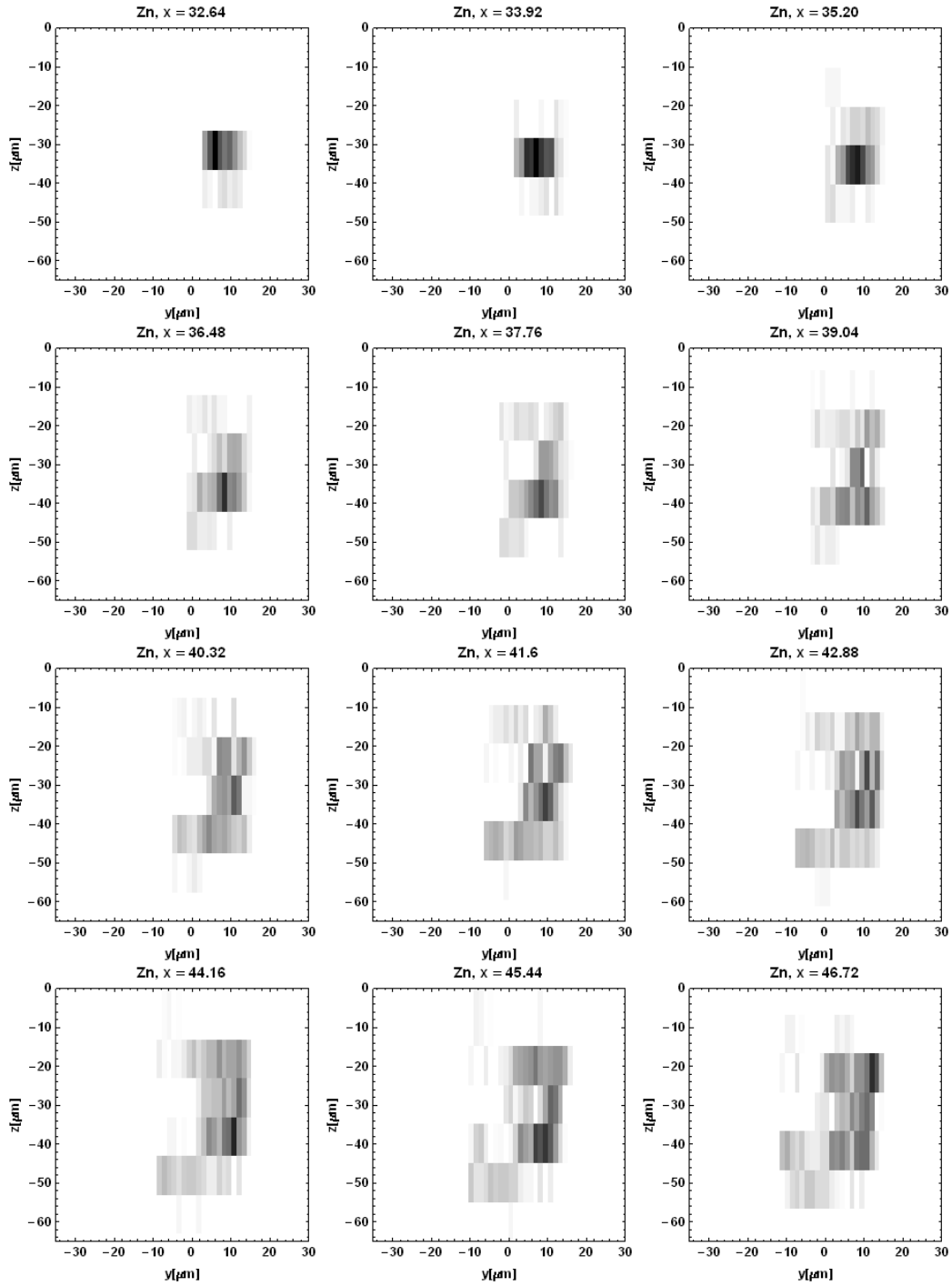

Figure 4.20: The next 12 slices from $x = 32.6$ μm to $x = 46.7$ μm of the reconstructed Zn distribution within the lower part of the GSR particle.

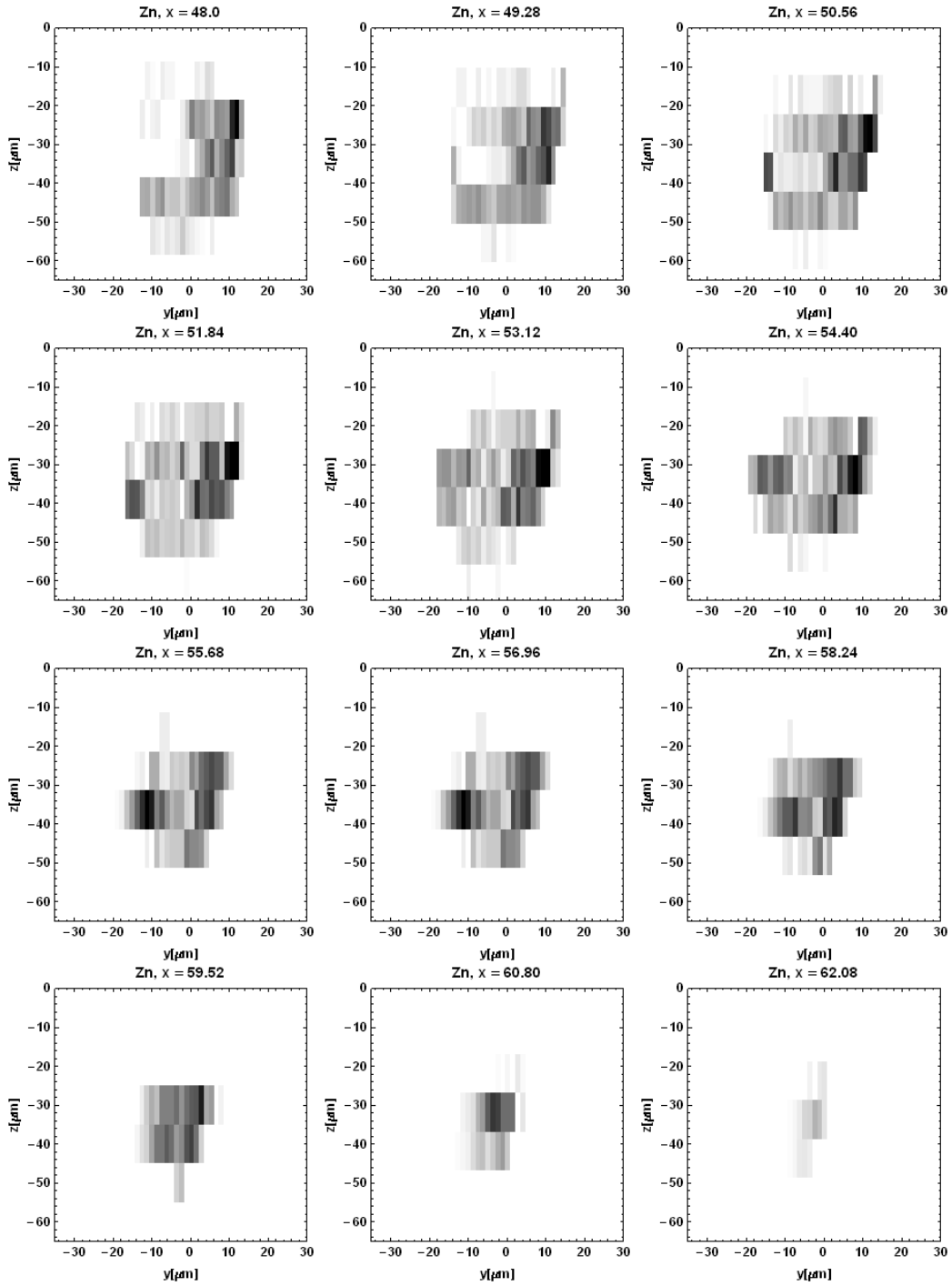

Figure 4.21: The last twelve slices from $x = 48$ μm to $x = 62.1$ μm of the reconstructed Zn distribution within the lower part of the GSR particle.

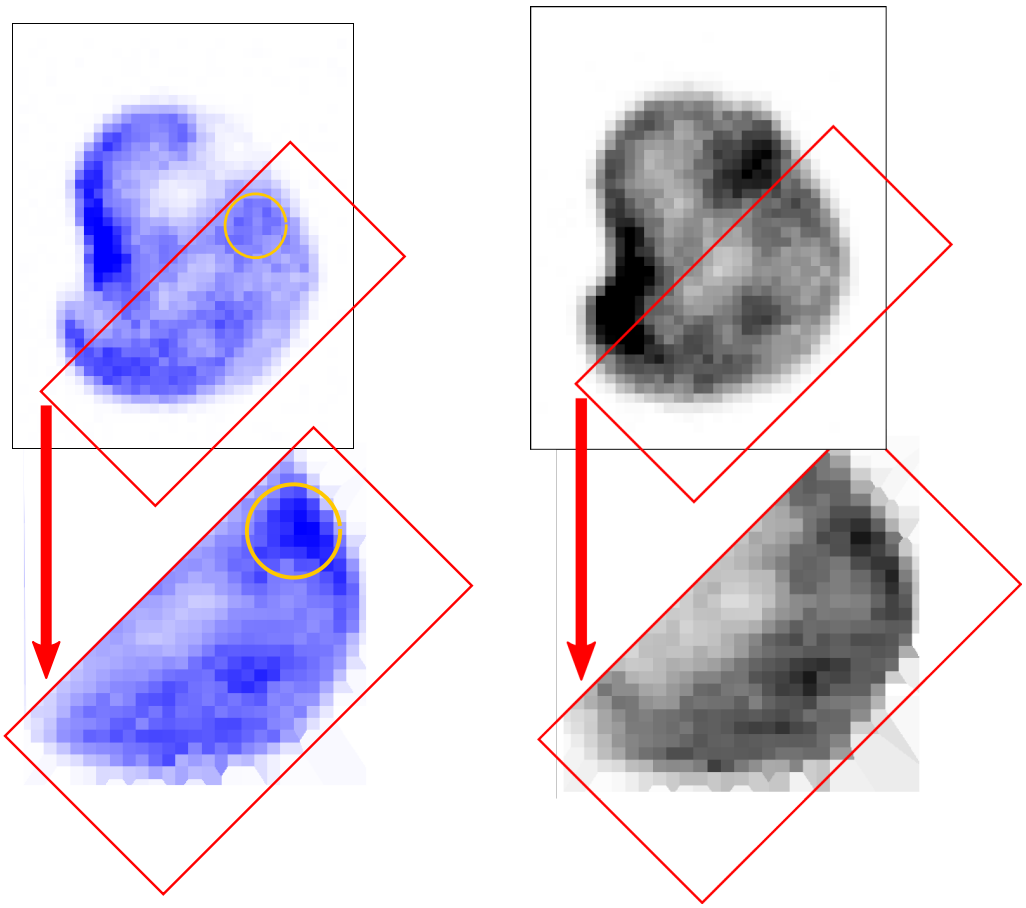

Figure 4.22: Comparison of the measured HPGe μ-PIXE map of Ti K_α (left) and Zn K_α (right) with the X-ray map generated from GSR particle concentrations reconstructed with CF PIXE. The area marked with yellow color differs in both Ti maps. This is due to the lack of reconstructed cells left of this area and consequentially insufficient absorption calculation. In Zn this effect is less visible, even though some areas at the far edge can not be accurately simulated.

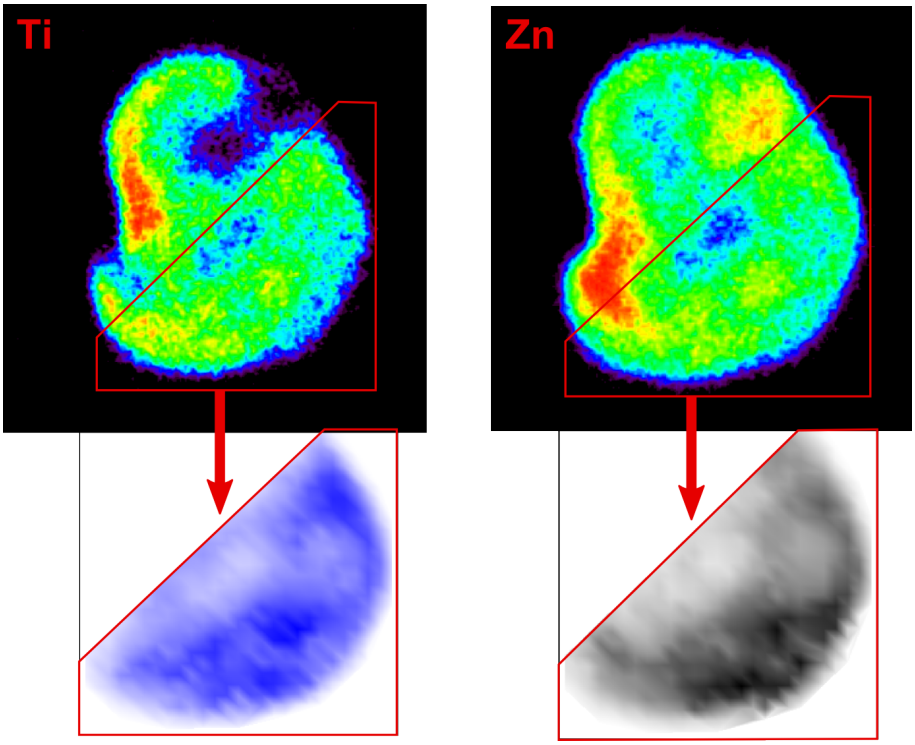

Figure 4.23: The comparison between the geoPIXE result (page 95) and the calculated concentration in each pixel averaged across 40 μm of particle depth.

4.3 Limitation of CF PIXE

The three-dimensional analysis presented in this chapter can bring comprehensive information about the sample and the distribution of elements. However, not all samples are suitable for such a spectroscopy at the present state of the art. Here, we will present some problems encountered by CF PIXE.

As we seen in Figure 2.22 on page 65, light elements with low X-ray energies undergo very strong absorption. Even targets composed of 100% of elements with characteristic lines below 3 keV need to be exposed for longer period in order to obtain sufficient statistics in the photon yield, while lighter elements that appear in trace amounts are more or less inappropriate for CF PIXE measurements. In addition, CF PIXE on light elements suffers from the unevitable increase of FWHM of the lens and therefore of the loss of spatial resolution.

An example of limited CF PIXE applicability is the analysis of textile fibers. These are samples with cotton or polymer matrix with several trace elements as additives for coloring purposes (Ti, Ca, Br, Zn), antibacterial protection (Ag) or some elements like Si, that remain in the sample after the oil treatment. The measured thread was antibacterial Antigard® polyester fiber (PES). The measurements at the external proton beam at two different facilities yield about 2.5% of Ti, the other elements were present in much smaller amount (Si 0.2, P 0.16, S 0.33, Cl 0.33, K 0.1, Ca 0.16, Mn 0.07, Fe 0.01 mass%) [106]. Ti comes mostly from nano TiO_2 which gives a white colour to the transparent polymer material. The polimer matrix is composed of light elements H, C, O that are undetectable by PIXE method.

Figure 4.24 shows several maps of the measured fiber at different positions from a measuring series, very similar as the ones described before (Figures 4.9 and 4.10). Presented positions along the beam are at 140 μm (1.), 85 μm (4.), 55 μm (6.), 10 μm (9.), -20 μm (11.) and -65 μm from the focal position. The proton energy was 2 MeV, the frame size 508×508 μm^2, however due to very slow accumulation of the signal we used only 35% of the frame (raster scan) in order to diminish the measurement time. This can clearly be seen in the HPGe X-ray maps presented in Figure 4.25. For the same reason, we also opened slits and widered the beam to around 4 μm^2, thus increasing the proton current on the sample to the order of 100 pA. Nevertheless, the map acquisition time was around 20 minutes, and the whole measurement lasted for almost 6 hours.

The only element visible with SDD detector equipped with the lens is Ti, however

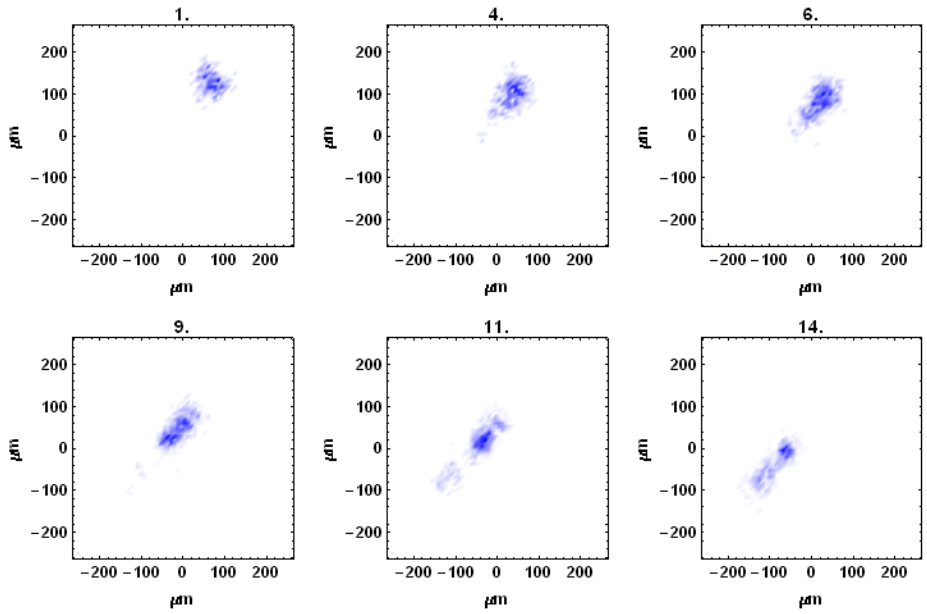

Figure 4.24: Several Ti X-ray maps from a series of Ti CF PIXE measurements from a fiber. Presented positions are 140 μm (1.), 85 μm (4.), 55 μm (6.), 10 μm (9.), -20 μm (11.) and -65 μm from the focal position along the beam. The original pixels were merged together in 64×64 pixel maps in order to increase the number of counts in one pixel. The frame size is 508×508 μm^2.

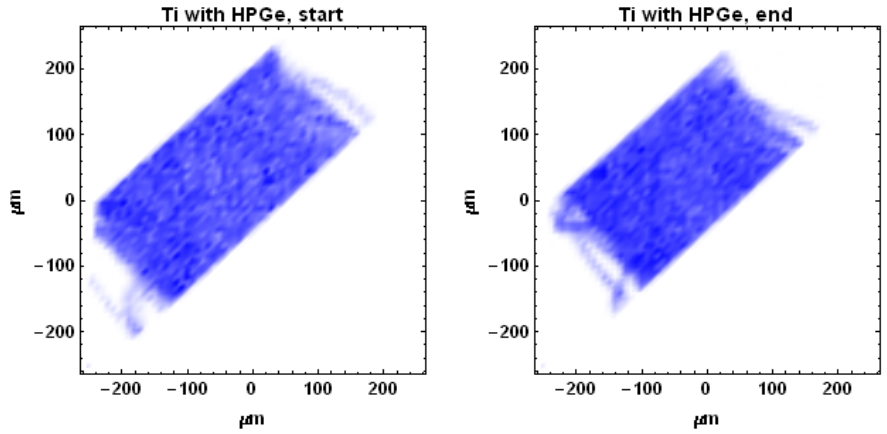

Figure 4.25: Two Ti X-ray map measured by HPGe detector with no lens at the beginning (left) and at the end (right) of the measuring process. The shrinking of the thread can be observed. The original pixels were merged together in 64×64 pixel maps. The frame size is 508×508 μm^2.

in 20 minutes only a few hundreds of counts were accumulated in the whole map. Germanium detector used for the monitoring detected Ti, as well as some uniformly distributed Mn and Fe. The concentration of the last two elements was obviously too low to be detected by the CF PIXE detector. Inspecting Figure 4.24, we can quickly realize that the CF measurements are of no real use. The Ti K_α yield is small and longer acquisition times would be required for reasonably accurate reconstruction. Related to that is the sample damage problem (Fig. 4.26 and 4.25). Long measurements over the same sample area (even though we move the target backward and forward, the proton beam strikes the same region all the time) introduced strong radiation damage – it caused carbonization of the fiber. Also the tensile strength of the fiber was drastically reduced – after the measurements the irradiated part was touched with a needle tip and the fiber was torn apart completely. The problem of such a damage is not only the change of the visual and physical proprieties of the material, it also has a consequence to induce shrinkage of the material during the measurements. On the two X-ray maps from germanium detector, taken at the beginning at the end of the measurement, presented in Figure 4.25, the rate of the fiber contraction is clearly visible. As the sample changes its shape with time, no object reconstruction can be done. The radiation damage and the consequent structure changes are one of the general problems that should be addressed in CF PIXE method.

Figure 4.26: A photograph taken with optical microscope of the fiber after the confocal measurements. The damage of the specimen is clearly seen in the irradiated region. At this area, the sample shrank considerately. The frame size is approximately 1.1×0.8 mm^2.

Another problem often encountered is again connected with long measurement periods and radiation damage effects. Even for heavy matrix and elements in abundance as in the gunshot residue particle, this phenomenon effects the surrounding material.

Particles, like GSR or small hematite particle analyzed before [47] are sticked or glued onto some substrate (SEM stubs with carbon tape, nuclepore filters, different plastic foils like Mylar, Kapton etc.). Proton beam deposits energy on the target which is therefore heated. When a substrate is composed of polymers that exhibit strong elasticity with increasing temperature, this can cause the particle attached to it to drift slightly during the measurement. Such an effect is demonstrated in Figure 4.27, which shows measurements at a few target positions of another gunshot residue particle. This particle came from similar ammunition as that analyzed in the first part of chapter 4 and is composed of Ti and Zn as well. Three $100 \times 100\ \mu\text{m}^2$ maps of Zn K_α line from HPGe detector are shown taken at three different target positions: 80 μm (1.), 10 μm (8.) and -70 μm (16.) from the focal point. The HPGe detector measures the emitted X-rays simultaneously with SDD and is used for monitoring the process. Each map was measured for around 15 minutes and the whole measurement again took several hours. The effect of particle drifting down is clearly visible. The whole particle shift was more than 10 μm. This is large, compared to the FWHM of the lens for Zn K_α X-rays, and such measurements can not be used for the reconstruction. However, if only a small drift occurs and the area observed with the lens does not change too much, then the movement can be eliminated by the alignment of HPGe maps during the analysis.

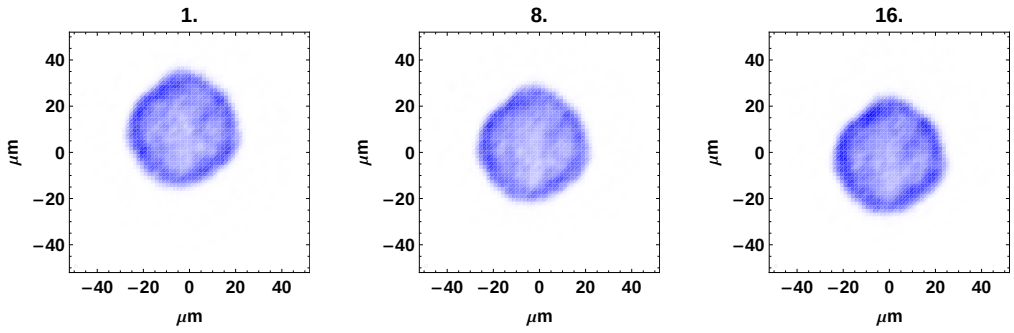

Figure 4.27: Zn K_α maps from germanium detector measured at three different target positions during the CF PIXE measurements of GSR particle. The positions are 80 μm (1.), 10 μm (8.) and -70 μm (16.) relative to the focal point. Movement of the particles during the experiment can be readily observed. The frame size is $100 \times 100\ \mu\text{m}^2$.

The fiber was a good example of a sample containing one or more trace elements (in concentrations of few mass percents or less) in a very light matrix. Similar examples are provided by botanical samples where the matrix is assumed to be celluloses while the trace elements of interest are heavier elements from Ca, through Ti, Mn, Fe, Zn, Cu to heavy metals like Cd, Pb or similar with concentrations not exceeding a few mass

percent. Such kind of samples are routinely measured by μ-PIXE at MIC and with the development of frozen tissue measurement possibilities that preserve sample morphology, the idea was to implement ion imaging by CF PIXE method for determination of 3D composition of trace elements. With the problems described, this will be very hard to achieve and we believe this types of samples are presently at the limit of the CF PIXE possibilities. The 3D analysis of such frozen hydrated tissues may be feasible only for few elements with sufficient concentrations, such as K.

Chapter 5

Summary and discussion

The idea to develop a new three-dimensionally elemental sensitive analytical technique (CF PIXE) was taken from 3D XRF method and successfully implemented at the nuclear microprobe. The lenses used for the first experiments in CF PIXE were taken from other applications and were mounted on the existing X-ray detectors mounted at the microbeam experimental chamber. As a consequence, the alignment procedure was improvised, and the resolution and performance compromised. Nevertheless, the first results were encouraging and we decided to build a dedicated CF PIXE set-up – the first of its kind in the similar ion beam laboratories in the world. This thesis describes the efforts required to achieve this goal and the applications of the new set-up.

The construction started with the choice of a new X-ray detector. The request for a detector that does not require heavy cryostat with liquid nitrogen for cooling led to the use of a Peltier-cooled SDD. The resulting alignment precision is now better also due to its lower mass. As we had a free flange in the experimental chamber elevated from the horizontal plane, the confocal set-up is implemented in a non-planar geometry. The detector characteristics are suited well for the targeted applications.

The difficulties encountered during the alignment phase of our first CF PIXE experiments encouraged us to build a dedicated interface that allows accurate positioning of the detector's snout in the plane perpendicular to the detector axis. The precise alignment is now much quicker and controlled. The associated load-lock system allows us to retract the detector with the lens attached and keep both in vacuum, when the interior of the chamber is vented to the atmospheric pressure. With the new system, the approximate confocal position is preserved over long periods of microprobe runs on other applications.

The selection of an optimal X-ray lens was another important step within the thesis. In collaboration with the selected manufacturer, we were looking for a compromise between demands for the smallest possible focal size in collecting regime, reasonable working distance and reasonable transmission. Three dedicated lenses were produced at IFG: the polycapillary half-lens 58mkl14, the polycapillary conic collimator CN01_PCCC (polyCCC), and finally, based on the available results, and in-line with the state of the art of the X-ray lens-production technology, the polycapillary semi-lens 119mmkl03. The three lenses were tested and characterized for the application in CF PIXE set-up. The size of the accepting volume was measured in dependence on the target-lens distance and on the X-ray energy. The transmission efficiency and the shape of the intensity distribution was investigated. The third lens (lens B) proved to have the best suited properties for confocal PIXE, with the FWHM of Ni K_α X-rays of 30 μm and larger transmission in comparison with the lens A. PolyCCC was eliminated from the quest due to its very small working distance, asymmetrical shapes of sensitive volume near the focal point and a prominent "halo" effect at the energies already above 9 keV. The effect of the lens application on the PIXE spectra background was also studied as it influences the detection sensitivity of PIXE.

PIXE method is known for its high elemental sensitivity and quantification ability. With the appropriate description of the lens properties, the same characteristics could be obtained for the CF PIXE. However, no standard software for PIXE spectra deconvolution and concentration calculation is able to describe such a complex "absorber", where the detection efficiency depends on the source position, and the calculations have to be done manually. We tested the quantification possibility at two reference materials – a thin Ni foil and a bulk Ti plate. The results confirmed the quantification ability at such basic sample geometries.

After the construction and detailed characterization of the set-up, possible applications were under consideration. Two types of materials were found to be of potential interest for CF PIXE analysis: laterally homogeneous layered materials and structured materials with non-homogeneous elemental distribution in all three dimensions.

Layered materials were analyzed in detail in the sample scanning mode at earlier improvised CF PIXE set-up. As the principles are the same and the analytical procedure does not depend on the geometry, we repeated the measurements on the new set-up for few artificially-made layered samples only. More emphasis was given to the possibilities of the analysis of layered material in the beam scanning mode. When the beam scans a layered sample, dislocated elemental "clouds" are obtained at the po-

sitions where the beam position overlaps with the lens acceptance volume. The elemental depth distributions of layers can be obtained within a single beam scanning of the sample. CF PIXE for depth-resolved analysis is limited by the depth resolution, however as it does not rely on the detection of the backscattered projectiles, elemental sensitivity of PIXE is preserved and any elemental combination of layers could be analyzed. Both abilities of CF PIXE ensure its future applications for the analysis on layered materials.

The combination of good lateral resolution provided by the microbeam and the depth sensitivity given by the X-ray lens enables tomography of micro-particles. The tomography implies both increased complexity of the measurements as well as the reconstruction. The simplest way of gaining such 3D distribution is by the division of the sample into unit cells. The elemental concentrations in each is considered constant and the values for each element in each cell is sought. The size of the cell is determined by the physical and experimental parameters of the set-up: size of the beam, FWHM of the lens acceptance angle, the steps of the target in z direction, the number of the steps made and maps measured, the initial proton energy etc. The shape of the cells is on the other hand determined by the processes in the target (beam stopping and the change of the ionization cross-section, the photon absorption etc.).

We tested the tomography possibilities of our set-up on the gunshot residue particle, created after the gun-shooting by Sintox-loaded ammunition. In this special type, the primer is composed from DDNP and tetracene as primary explosives, ZnO_2 as oxidizer and nitrocellulose with Ti metal powder as propellants. This results in two visible elements, Ti and Zn, in the gunshot residue. Due to the finite size of the lens acceptance volume, only half of the particle could be analyzed in a single sequence of shifts along the proton beam axis. Nevertheless, we managed to reconstruct the distribution of both elements in that part of the sample. As it could be intuitively predicted from the measured elemental maps, the center of the particle is depleted, while the lower part is relatively heavily loaded, as well as the thin shell above the center. The "bubble" inside could be result of gas trapped during the solidification. The particle has a diameter of approximately 40 μm.

With the reconstructed elemental distribution, we managed to calculate the yield, as expected to be measured with the HPGe detector with no lens attached. The back-projected X-ray map coincides well with the measured one at the HPGe. There are some discrepancies between the two at the areas where the composition of elements in the direction of Ge detector is not known, so the absorption could not be accurately

calculated.

As gunshot residue particles are usually analyzed by scanning electron microscope, the elements, their concentration and their relative amount from the surface can be obtained. Standard PIXE can provide insight into deeper structure averaging the concentrations and elemental ratios. CF PIXE is able to provide information on the distribution of elements within the GSR micro-particles and consequentially, improved knowledge on the GSR creation process.

No matter the complexity of the reconstruction, CF PIXE offers the possibility to obtain three-dimensional distribution of elements in micro-particles, even when they are too large to be transparent for protons or photons at some energy. In this case, only part of the particle that is closer to the surface can be investigated, however this is much more than the other methods offer. Naturally, CF PIXE method suffers from several severe limitations as well. The problem of small lens transmission at low X-ray energies disables the applicability for lighter elements. The same problem, relatively heavy absorption, limits the ability of the tomography for the trace elements. Due to relatively long exposure times, the radiation damage can interfere with the measurements and not all samples are suitable for CF PIXE analysis. The depth resolution is largely determined by the size of the acceptance volume, which is an order of magnitude larger than the available proton microbeam size. However, the size of the acceptance volume determines the area observed by the detector. If this is very small in order to gain the depth resolution, only small part of the particle could be visible and later reconstructed. This would involve additional sample movement also in directions perpendicularly to the proton beam and, consequently, it would increase the complexity of the measurements. A potential solution might be a lens with asymmetrical acceptance volume, well aligned in such a way that the shorter axis would point into the depth, while the longer axis would be aligned with the particle surface.

One of the positive properties of CF PIXE is the absence of required sample preparation. However, there are some limitation here as well. When particles are sticked or glued onto a substrate, such as carbon tape or nuclepore filters, long beam exposure times of the particular sample area can cause overheating of the surrounding substrate. This results in the movement of the particle. If only small shifts are encountered, they can be corrected by aligning the maps of the controlling detector. If they are to big and the particle moved essentially in the lens field of view, then the CF PIXE analysis is not possible.

The next step in the development would be to ease or automatize the reconstruction

process. No matter how complex the reconstruction is, its basic principles are now provided for a general case and could be implemented in the future within a dedicated CF PIXE software.

Bibliography

[1] S. Johansson, J. Campbell, K. Malmqvist, Particle-induced X-ray emission spectrometry (PIXE), John Wiley & sons, New York, 1995.

[2] W.-K. Chu, J. W. Mayer, M.-A. Nicolet, Backscattering spectrometry, Academic press, New York, 1978.

[3] J. R. Tesmer, M. Nastasi (Eds.), Handbook of modern ion beam materials analysis, Materials research society, Pittsburgh, 1995.

[4] Ž. Šmit, Spektroskopske metode s pospešenimi ioni, DMFA založništvo, Ljubljana, 2003.

[5] Ž. Šmit, Z ioni nad arheološke in umetniške predmete, Delo (znanost) 10.sept. 1997.

[6] J. Simčič, P. Pelicon, M. Budnar, Ž. Šmit, The performance of the Ljubljana ion microprobe, Nucl. Instrum. Methods Phys. Res., Sect. B 190 (2002) 283–286.

[7] S. Markelj, P. Pelicon, J. Simčič, Z. Rupnik, I. Čadež, Studying permeation of hydrogen (H and D) through Palladium membrane dynamically with ERDA method, Nucl. Instrum. Methods Phys. Res., Sect. B 261 (2007) 498–503.

[8] M. Kavčič, Improved detection limits in PIXE analysis employing wavelength dispersive X-ray spectroscopy, Nucl. Instrum. Methods Phys. Res., Sect. B 268 (2010) 3438–3442.

[9] M. Kavčič, A.-G. Karydas, C. Zarkadas, Chemical state analysis employing sub-natural linewidth resolution PIXE measurements of K[alpha] diagram lines, X-ray spectrom. 34 (2005) 310–314.

[10] Ž. Šmit, T. Knific, D. Jezeršek, J. Istenič, Analysis of early medieval glass beads — Glass in the transition period, Nucl. Instrum. Methods Phys. Res., Sect. B 278 (2012) 8–14.

[11] M. Žitnik, M. Jakomin, P. Pelicon, Z. Rupnik, J. Simčič, M. Budnar, N. Grlj, B. Marzi, Port of Koper – elemental concentrations in aerosols by PIXE, X-ray spectrom. 34 (2005) 330–334.

[12] P. Pongrac, K. Vogel-Mikuš, P. Vavpetič, J. Tratnik, M. Regvar, J. Simčič, N. Grlj, P. Pelicon, Cd induced redistribution of elements within leaves of the Cd/Zn hyperaccumulator Thlaspi praecox as revealed by micro-PIXE, Nucl. Instrum. Methods Phys. Res., Sect. B 268 (2010) 2205–2210.

[13] L. Lyubenova, P. Pongrac, K. Vogel-Mikuš, G. Kukec Mezek, P. Vavpetič, N. Grlj, P. Kump, M. Nečemer, M. Regvar, P. Pelicon, P. Schröder, Localization and quantification of Pb and nutrients in Typha latifolia by micro-PIXE, Metallomics 4 (2012) 333–341.

[14] B. Cestone, K. Vogel-Mikuš, P. Pongrac, P. Pelicon, P. Vavpetč, N. Grlj, L. Jeromel, P. Kump, M. Nečemer, M. Regvar, F. Navari-Izzo, Use of micro-PIXE to determine spatial distributions of copper in Brassica carinata plants exposed to CuSO4 or CuEDDS, Sci. total environ. 427-428 (2012) 339–346.

[15] Ž. Pipan Tkalec, D. Drobne, K. Vogel-Mikuš, P. Pongrac, M. Regvar, J. Štrus, P. Pelicon, P. Vavpetič, N. Grlj, M. Remškar, Micro-PIXE study of Ag in digestive glands of a nano-Ag fed arthropod (Porcellio scaber, Isopoda, Crustacea), Nucl. Instrum. Methods Phys. Res., Sect. B 269 (2011) 2286–2291.

[16] C. G. Ryan, Ion beam microanalysis in geoscience research, Nucl. Instrum. Methods Phys. Res., Sect. B 219-220 (2004) 534–549.

[17] Ž. Šmit, D. Jezeršek, P. Pelicon, P. Vavpetič, M. Jeršek, B. Mirtič, Analysis of a chondrite meteorite from Slovenia, X-ray spectrom. 40 (2011) 205–209.

[18] S. Matsuyama, G. Catella, K. Ishii, A. Terakawa, Y. Kikuchi, Y. Kawamura, S. Ohkura, M. Fujikawa, N. Hamada, K. Fujiki, Y. Hatori, Y. Ito, H. Yamazaki, Y. Hashimoto, M. Žitnik, P. Pelicon, N. Grlj, Microbeam analysis of individual particles in indoor working environment, X-ray spectrom. 40 (2011) 172–175.

[19] K. Stražar, M. Kavčič, J. Simčič, P. Pelicon, Ž. Šmit, P. Kump, R. Jaćimović, V. Antolić, A. Cör, Quantification of BaSO4 and polyacetal wear particles in the periprosthetic tissue around loosened isoelastic hip stems by nuclear microprobe, Nucl. Instrum. Methods Phys. Res., Sect. B 249 (2006) 719–722.

[20] L. Beck, P. Gutierrez, J. Salomon, P. Walter, M. Menu, Characterization of white pigments and paint layers by simultaneous PIXE and RBS, in: Proceeding of the XI International conference on PIXE and its Analytical Applications, Puebla, Mexico, 2007.

[21] C. Pascual-Izarra, N. Barradas, M. Reis, C. Jeynes, M. Menu, B. Lavedrine, J. Ezrati, S. Röhrs, Towards truly simultaneous PIXE and RBS analysis of layered objects in cultural heritage, Nucl. Instrum. Methods Phys. Res., Sect. B 261 (2007) 426–429.

[22] C. Neelemeijer, W. Wagner, H. Schramm, Depth resolved ion beam analysis of objects of art, Nucl. Instrum. Methods Phys. Res., Sect. B 118 (1996) 338–345.

[23] G. Weber, J. Delbrouck, D. Strivay, F. Kerff, L. Martinot, Use of a variable incidence angle PIXE arrangement for studying pigment multilayers, Nucl. Instrum. Methods Phys. Res., Sect. B 139 (1998) 196–201.

[24] Ž. Šmit, M. Holc, Differential PIXE measurements of thin metal layers, Nucl. Instrum. Methods Phys. Res., Sect. B 219-220 (2004) 524–529.

[25] Ž. Šmit, M. Uršič, P. Pelicon, T. Trček-Pečak, B. Šeme, A. Smrekar, I. Langus, I. Nemec, K. Kavkler, Concentration profiles in paint layers studied by differential PIXE, Nucl. Instrum. Methods Phys. Res., Sect. B 266 (2008) 2047–2059.

[26] A. Saint, M. Cholewa, G. Legge, PIXE tomography, Nucl. Instrum. Methods Phys. Res., Sect. B 75 (1993) 504–510.

[27] A. Antolak, G. Bench, PIXE tomography of samples with inhomogeneous elemental composition, Nucl. Instrum. Methods Phys. Res., Sect. B 88 (1994) 297–307.

[28] C. Michelet, P. Moretto, 3D mapping of individual cells using a proton microbeam, Nucl. Instrum. Methods Phys. Res., Sect. B 150 (1999) 173–178.

[29] D. Beasley, N. Spyrou, The University of Surrey's new proton microprobe and the feasibility of PIXE-tomography for trace element analysis of biological tissues, J. Radioanal. Nucl. Chem. 264 (2005) 289–294.

[30] D. Beasley, I. Gomez-Morilla, N. Spyrou, Elemental analysis of hair using PIXE-tomography and INAA, J. Radioanal. Nucl. Chem. 276 (2008) 101–105.

[31] A. Sakellariou, D. Jemieson, G. Legge, Three-dimensional ion microtomography, Nucl. Instrum. Methods Phys. Res., Sect. B 181 (2001) 211–218.

[32] T. Andrea, M. Rothermel, T. Butz, T. Reinert, The improved STIM tomography set-up at LIPSION: Three-dimensional reconstruction of biological samples, Nucl. Instrum. Methods Phys. Res., Sect. B 267 (2009) 2098–2102.

[33] T. Rainert, A. Sakellariou, M. Schwertner, J. Vogt, T. Butz, Scanning transmission ion microscopy tomography at the Leipzig nanoprobe LIPSION, Nucl. Instrum. Methods Phys. Res., Sect. B 190 (2002) 266–270.

[34] K. Ishii, S. Matsuyama, Y. Watanabe, Y. Kawamura, T. Yamaguchi, R. Oyama, G. Momose, A. Ishizaki, H. Yamazaki, Y. Kikuchi, 3D-imaging using micro-PIXE, Nucl. Instrum. Methods Phys. Res., Sect. A 571 (2007) 64–68.

[35] K. Tanaka, T. Shobu, H. Kimachi, Hybrid measurement of CT and strain distribution of internal crack using synchrotron high-energy monochromatic X-rays, Materials Science Forum 652 (2010) 202–209.

[36] B. Beckhoff, B. Kanngießer, N. Langhoff, R. Wedell, H. Wolff (Eds.), Handbook of Practical X-Ray Fluorescence Analysis, Springer-Verlag Berlin Heidelberg, 2006, Ch. 3 (X-Ray Optics), pp. 85–194.

[37] W. Chao, B. Harteneck, J. Liddle, E. Anderson, D. Attwood, Soft X-ray microscopy at a spatial resolution better than 15 nm, Nature 435 (2005) 1210–1213.

[38] A. Erko, A. Firsov, High-resolution diffraction X-ray optics, Optics and Precision Engineering 15 (2007) 1816–1822.

[39] P. Kirkpatrick, A. Baez, Formation of optical images by X-rays, J. Opt. Soc. Am. 38 (1948) 766–774.

[40] Y. Suzuki, F. Uchida, Hard X-ray microprobe with total reflection mirrors, Rev. Sci. Instrum. 63 (1992) 578–581.

[41] A. Snigirev, V. Kohn, I. Snigireva, B. Lengeler, A compound refractive lens for focusing high-energy X-rays, Nature 384 (1996) 49–51.

[42] B. Lengler, C. Schroer, M. Richwin, J. Tümmler, A microscope for hard X-rays based on parabolic compound refractive lenses, Appl. Phys. Lett. 74 (1999) 3924–3926.

[43] B. Kanngießer, W. Malzer, I. Reiche, A new 3D micro X-ray fluorescence analysis set-up – first archaeometric applications, Nucl. Instrum. Methods Phys. Res., Sect. B 221-222 (2003) 259–264.

[44] B. Kanngießer, I. Mantouvalou, W. Malzer, T. Wolff, O. Hahn, Non-destructive, depth resolved investigation of corrosion layers of historical glass objects by 3D Micro X-ray fluorescence analysis, J. Anal. At. Spectrom. 23 (2008) 814–819.

[45] I. Mantouvalou, W. Malzer, I. Schaumann, L. Lühl, R. Dargel, C. Vogt, B. Kanngießer, Reconstruction of thickness and composition of stratified materials by means of 3D micro X-ray fluorescence spectroscopy, Anal. Chem. 80 (2008) 819–826.

[46] A.-G. Karydas, D. Sokaras, C. Zarkadas, N. Grlj, P. Pelicon, M. Žitnik, R. Schütz, W. Malzer, B. Kanngießer, 3D micro PIXE – a new technique for depth-resolved elemental analysis, J. Anal. At. Spectrom. 22 (2007) 1260—-1265.

[47] M. Žitnik, N. Grlj, P. Vavpetič, P. Pelicon, K. Bučar, D. Sokaras, A.-G. Karydas, B. Kanngießer, 3D recostruction of an object by means of a confocal micro-PIXE, J. Anal. At. Spectrom. 25 (2010) 28–33.

[48] D. Sokaras, A.-G. Karydas, W. Malzer, R. Schütz, B. Kanngießer, N. Grlj, P. Pelicon, M. Žitnik, Quantitative analysis in confocal micro-PIXE – general concept and layered materials, J. Anal. At. Spectrom. 24 (2009) 611–621.

[49] M. Žitnik, P. Pelicon, N. Grlj, A.-G. Karydas, D. Sokaras, R. Schütz, B. Kanngießer, Three-dimensional imaging of aerosol particles with scanning proton microprobe in a confocal arrangement, Appl. Phys. Lett. 93 (2008) 094104–1–3.

[50] M. Žitnik, P. Pelicon, K. Bučar, N. Grlj, A.-G. Karydas, D. Sokaras, R. Schütz, B. Kanngießer, Element-selective three-dimensional imaging of microparticles with a confocal micro-PIXE arrangement, X-Ray spectrom. 38 (2009) 526–539.

[51] B. Kanngießer, A. Karydas, R. Schütz, D. Sokaras, I. Reiche, S. Röhrs, L. Pichon, J. Salomon, 3D micro-PIXE at atmospheric pressure: A new tool for the investigation of art and archaeological objects, Nucl. Instrum. Methods Phys. Res., Sect. B 264 (2007) 383–388.

[52] Oxford Microbeams, Ltd, accessed: 12th June 2012.
URL http://www.microbeams.co.uk

[53] P. Vavpetič, P. Pelicon, K. Vogel-Mikuš, N. Grlj, P. Pongrac, L. Jeromel, N. Ogrinc, M. Regvar, Micro-PIXE of thin plant tissue samples in frozen hydrated state: the first results at JSI nuclear microprobe, abstract accepted for presentation in ICNMTA 2012 (2012).

[54] P. Pelicon, P. Vavpetič, N. Grlj, I. Čadež, S. Markelj, S. Brezinšek, A. Kreter, T. Dittmar, E. Tsitrone, B. Pegourie, P. Languille, M. Rubel, T. Schwarz-Selinger, Fuel retention study in fusion reactor walls by micro-NRA deuterium mapping, Nucl. Instrum. Methods Phys. Res., Sect. B 269 (2011) 2317–2321.

[55] K. Vogel-Mikuš, P. Pelicon, P. Vavpetič, I. Kreft, M. Regvar, Elemental analysis of edible grains by micro-PIXE: Common buckwheat case study, Nucl. Instrum. Methods Phys. Res., Sect. B 267 (2009) 2884–2889.

[56] T. Žagar, Presevna ionska mikroskopija v združeni osno-izvenosni geometriji, Diploma work, University of Ljubljana, Faculty of Mathematics and Physics (2011).

[57] Ultra-thin AP3 X-ray windows datasheet, MOXTEK, Inc., 452 W 1260 N Orem, UT 84057, USA, accessed: 20th March 2012.
URL http://www.moxtek.com

[58] P. Pelicon, J. Simčič, M. Jakšič, Z. Medunić, F. Naab, F. McDaniel, Spherical chamber – effective solution for multipurpose nuclear microprobe, Nucl. Instrum. Methods Phys. Res., Sect. B 231 (2005) 53–59.

[59] e2v scientific instruments limited, accessed: 6th June 2012.
URL http://www.e2vsi.com

[60] The institute of low energy nuclear physics, accessed: 23rd May 2011.
URL http://lenp.bnu.edu.cn/lenp/introduction.htm

[61] X-ray optical systems, XOS, accessed: 23rd May 2011.
URL http://www.xos.com

[62] Institute for scientific instruments GmbH, accessed: 23rd May 2011.
URL http://www.ifg-adlershof.de/

[63] M. Haschke, M. Haller, Examination of poly-capillary lenses for their use in micro-XRF spectrometers, X-ray spectrom. 32 (2003) 239–247.

[64] A. Bzhaumikhov, N. Langhoff, J. Schmalz, R. Wedell, V. Beloglazov, N. Lebedev, Polycapillary conic collimator for micro-XRF, in: Proceeding of the SPIE conference on X-ray Optics, Instruments and Missions, Vol. 3444, 1998, pp. 430–435.

[65] M. Kumakhov, F. Komarov, Multiple reflection from surface X-ray optics, Physics reports 191 (1990) 289–350.

[66] N. Grlj, Uporaba polikapilar pri metodi mikro PIXE: karakterizacija ter globinska analiza vzorcev, Diploma work, University of Ljubljana, Faculty of Mathematics and Physics (2007).

[67] R. Guenther, Modern optics, John Wiley & sons, USA, 1990.

[68] Center for X-ray optics, accessed: 22nd March 2012.
URL `http://henke.lbl.gov/optical_constants`

[69] T. Wolff, I. Mantouvalou, W. Malzer, J. Nissen, D. Berger, I. Zizak, D. Sokaras, A.-G. Karydas, N. Grlj, P. Pelicon, R. Schütz, M. Žitnik, B. Kanngießer, Performance of a polycapillary halflens as focusing and collecting optics – a comparison, J. Anal. At. Spectrom. 24 (2009) 669–675.

[70] K. Tsuji, J. Injuk, R. Van Grieken (Eds.), X-Ray Spectrometry: Recent Technological Advances, John Wiley & Sons, 2004, Ch. 3.3 (Polycapillary X-ray Optics), pp. 81–110.

[71] J. Gormley, T. Jach, E. Steel, Q.-F. Xiao, Polycapillary X-ray optic spectral gain and transmission, X-Ray Sectrom. 28 (1999) 115–120.

[72] K. Proost, L. Vincze, K. Janssens, N. Gao, E. Bulska, M. Schreiner, G. Falkenberg, Characterization of a polycapillary lens for use in micro-XANES experiments, X-ray spectrom. 32 (2003) 215–222.

[73] A. Bjeoumikhov, M. Erko, S. Bjeoumikhova, A. Erko, I. Snigireva, A. Snigirev, T. Wolff, I. Mantouvalou, W. Malzer, B. Kanngießer, Capillary μ-focus X-ray lenses with parabolic and elliptic profile, Nucl. Instrum. Methods Phys. Res., Sect. A 587 (2008) 458–463.

[74] T. Sun, X. Ding, Determination of the properties of a polycapillary X-ray lens, X-Ray Spectrom. 35 (2006) 120–124.

[75] M. Kumakhov, Capillary optics and their use in X-ray analysis, X-ray spectrom. 29 (2000) 343.

[76] L. Wang, B. Rath, W. Gibson, J. Kimball, C. MacDonald, Performance study of polycapillary optics for hard x-rays, J. Appl. Phys. 80 (1996) 3628–3638.

[77] N. Gao, I. Ponomarev, Polycapillary X-ray optics: manufacturing status, characterization and the future of technology, X-ray spectrom. 32 (2003) 186–194.

[78] T. Sun, X. Ding, Study on the measurements of the properties of polycapillary X-ray lens, Nucl. Instr. and Meth. in Phys. Res. B 226 (2004) 651–658.

[79] T. Sun, X. Ding, Measurements of energy dependence of properties of polycapillary X-ray lens by using organic glass as a scatterer, J. Appl. Phys. 97 (2005) 124904.

[80] A. Bjeoumikhov, N. Langhoff, R. Wedell, V. Beloglazov, N. Lebedev, N. Skibina, New generation of polycapillary lenses: manufacture and applications, X-ray spectrom. 32 (2003) 172–178.

[81] A. Bjeoumikhov, S. Bjeoumikhova, R. Wedell, Capillary optics in X-ray analytics, Part. Part. Syst. Charact. 22 (2005) 384–390.

[82] D. Hampai, S. B. Dabagov, G. Cappuccio, G. Cibin, X-ray propagation through hollow channel: PolyCAD – a ray tracing code, Nucl. Instr. and Meth. in Phys. Res. B 244 (2006) 481–488.

[83] D. Hampai, S. B. Dabagov, G. Cappuccio, G. Cibin, X-ray propagation through polycapillary optics studied through a ray tracing approach, Spectrochimica Acta Part B 62 (2007) 608–614.

[84] V. Rackwitz, M. Procop, S. Bjeoumikhova, U. Panne, V.-D. Hodoroaba, A routine procedure for the characterisation of polycapillary X-ray semi-lenses in parallelising mode with SEM/EDS, J. Anal. At. Spectrom. 26 (2011) 499–504.

[85] N. Grlj, P. Pelicon, M. Žitnik, P. Vavpetič, D. Sokaras, A.-G. Karydas, B. Kangießer, Construction of a confocal PIXE set-up at the Jožef Stefan Institute and first results, Nucl. Instrum. Methods Phys. Res., Sect. B 269 (2011) 2237–2243.

[86] N. Grassi, C. Guazzoni, R. Alberti, T. Klatka, A. Bjeoumikhov, External scanning micro-PIXE for the characterization of a polycapillary lens: Measurement of the collected x-ray intensity distribution, Nucl. Instr. and Meth. in Phys. Res. B 268 (2010) 1945–1948.

[87] L. Vincze, B. Vekemans, F. Brenker, G. Falkenberg, K. Rickers, A. Somogyi, M. Kersten, F. Adams, Three-dimensional trace element analysis by confocal X-ray microfluorescence imaging, Anal. Chem. 76 (2004) 6786–6791.

[88] C. Fiorini, A. Longoni, A. Bjeoumikhov, A new detection system with polycapillary conic collimator for high-localized analysis of X-ray fluorescence emission, IEEE transactions on nuclear science 48 (2001) 268–271.

[89] G. Paternoster, R. Rinzivillo, F. Nunziata, E. M. Castellucci, C. Lofrumento, A. Zoppi, A. C. Felici, G. Fronterotta, C. Nicolais, M. Piacentini, S. Sciuti, M. Vendittelli, Study on the technique of the Roman age mural paintings by micro-XRF with Polycapillary Conic Collimator and micro-Raman analysis, J. Cult. Herit. 6 (2005) 21–28.

[90] J. Ziegler, SRIM – the stopping and range of ions in matter, accessed: 10th November 2011.
URL http://www.srim.org

[91] Micromatter XRF calibration standards, MICROMATTER, 4004 Wesbrook Mall, Vancouver, Canada, accessed: 8th December 2011.
URL http://www.micromatter.com/xrf.php

[92] N. Liebing, IfG, Berlin, personal correspondence.

[93] H. Paul, J. Sacher, Fitted empirical reference cross sections for K-shell ionization by protons, Atom. Data Nucl. Data 42 (1989) 105–156.

[94] R. Gardner, T. J. Gray, Cross sections for K-shell ionization, X-ray production or auger-electron production by ion impact, Atom. Data Nucl. Data 21 (1978) 515–536.

[95] M. H. Chen, B. Crasemann, Relativistic cross sections for atomic K- and L-shell ionization by protons, calculated from a Dirac-Hartree-Slater model, Atom. Data Nucl. Data 33 (1985) 217–233.

[96] B. Henke, E. Gullikson, J. Davis, X-ray interactions: Photoabsorption, scattering, transmission, and reflection at E = 50-30,000 eV, Z = 1-92, Atom. Data Nucl. Data 54 (1993) 181–342.

[97] X-ray data booklet, Lawrence Berkeley National Laboratory, University of California, Berkeley, CA 94720 (September 2009).

[98] J. Campbell, N.-I. Boyd, N. Grassi, P. Bonnick, J. Maxwell, The guelph PIXE software package IV, Nucl. Instrum. Methods Phys. Res., Sect. B 268 (2010) 3356–3363.

[99] GUPIX – the versatile PIXE spectrum fitting software, University of Guelph, accessed: 27th March 2012.
URL http://pixe.physics.uoguelph.ca/gupix/main/

[100] C. Ryan, D. Jamieson, C. Churms, J. Pilcher, A new method for on-line true-elemental imaging using PIXE and the proton microprobe, Nucl. Instrum. Methods Phys. Res., Sect. B 104 (1995) 157–165.

[101] GeoPIXE – quantitative PIXE imaging and analysis software, CSIRO Earth Science and Resource Engineering, accessed: 27th March 2012.
URL http://www.nmp.csiro.au/GeoPIXE.html

[102] J. Hubbell, P. Trehan, N. Singh, B. Chand, D. Mehta, M. Garg, R. Garg, S. Singh, S. Puri, A review, bibliography, and tabulation of K, L, and higher atomic shell X-ray fluorescence yields, J. Phys. Chem. Ref. Data 23 (1994) 339–364.

[103] M. Mayer, SIMNRA, a simulation program for the analysis of NRA, RBS and ERDA, in: J. Duggan, I. Morgan (Eds.), Proceedings of the 15th International Conference on the Application of Accelerators in Research and Industry, Vol. 475, American Institute of Physics Conference Proceedings, 1999, pp. 541–544.

[104] M. Mayer, SIMNRA, Max-Planck-Institut für Plasmaphysik, Germany, accessed: 29th March 2012.
URL http://www.simnra.com

[105] D. Jezeršek, Ž. Šmit, P. Pelicon, External beamline setup for plated target investigation, Nucl. Instrum. Methods Phys. Res., Sect. B 268 (2010) 2006–2009.

[106] D. Jezeršek, Ion beam analysis of geometrically structured samples, Ph.D. thesis, Jožef Stefan International Postgraduate School (august 2011).

[107] O. Dalby, D. Butler, W. B. Jason, Analysis of gunshot residue and associated materials – a review, J. Forensic Sci. 55 (2010) 924–943.

[108] M. J. Bailey, K. J. Kirkby, C. Jeynes, Trace element profiling of gunshot residues by PIXE and SEM-EDS: a feasibility study, X-ray spectrom. 28 (2009) 190–194.

[109] Z. Oommen, S. M. Pierce, Lead-free primer residues: a qualitative characterization of Winchester WinClean, Remington/UMC LeadLess, Federal Ballisti-Clean and Speer Lawman CleanFire handgun ammunition, J. Forensic Sci. 51 (2006) 509–519.

[110] R. Hagel, K. Redecker, Use of zinc peroxide as oxidant for explosives and pyrotechnical mixtures, US Patent no 4363679 (1982).

[111] L. Gunaratnam, K. Himberg, The identification of gunshot residue particles from lead-free Sintox ammunition, J. Forensic Sci. 39 (1994) 532–536.

[112] W. R. Leo, Techniques for nuclear and particle physics experiments, Springer-Verlag, Germany, 1992.

[113] Ž. Šmit, M. Budnar, V. Cindro, M. Ravnikar, V. Ramšak, Secondary fluorescence correction in thick target PIXE analysis, Nucl. Instrum. Methods Phys. Res., Sect. A 228 (1985) 482–489.

[114] MATHEMATICA, Wolfram Research, Inc., USA, accessed: 26th April 2012.
URL http://www.wolfram.com/mathematica/

[115] W. H. Press, S. A. Teukolsky, W. T. Vetterling, B. P. Flannery, Numerical recipies in C, Cambridge University Press, USA, 1992.

Appendix A

Some geometrical equations

This appendix is devoted to several geometrical calculations that are required in the analysis of the X-ray maps measured by the confocal PIXE set-up, either in the course of the reconstruction process (Chapter 4) or during the analysis of standard material (Chapter 2). The three coordinate systems were introduced and here we describe their basis vectors and the transformations between the coordinates. Further on, the calculation of the straight photon path in a flat thick target is presented.

A.1 Basis vectors of the coordinate systems S, S'' and Σ and the transformations between

The coordinate systems S and S'', the "beam" and the "lens" system, respectively, were presented in section 2.4. The coordinates of a given point in space can be written in any of them. The normalized basis vectors of S and S'' system with a common origin are presented in table A.1.

basis vector	coordinates in S	coordinates in S''
$\vec{e_x}$	$(1, 0, 0)$	$(\cos\varphi, \sin\varphi \sin\vartheta, -\cos\vartheta \sin\varphi)$
$\vec{e_y}$	$(0, 1, 0)$	$(0, \cos\vartheta, \sin\vartheta)$
$\vec{e_z}$	$(0, 0, 1)$	$(\sin\varphi, -\cos\varphi \sin\vartheta, \cos\vartheta \cos\varphi)$
$\vec{e_{x''}}$	$(\cos\varphi, 0, \sin\varphi)$	$(1, 0, 0)$
$\vec{e_{y''}}$	$(\sin\varphi \sin\vartheta, \cos\vartheta, -\cos\varphi \sin\vartheta)$	$(0, 1, 0)$
$\vec{e_{z''}}$	$(-\sin\varphi \cos\vartheta, \sin\vartheta, \cos\varphi \cos\vartheta)$	$(0, 0, 1)$

Table A.1: Basis vectors and transformation between S and S'' coordinate systems.

Coordinate system Σ was introduced in Chapter 4 in order to ease the reconstruction procedure. It is defined by three basis vectors $\vec{\varsigma}, \vec{\tau}$ and $\vec{\upsilon}$ that span the three-dimensional space (Equation (4.1)). Those vectors are not orthogonal, but they are linearly independent (Eq. (A.1)).

$$\begin{aligned} a\vec{\varsigma} + b\vec{\tau} + c\vec{\upsilon} &= 0 \\ a(0,0,1)_S + b(0,1,0)_S + c\,(-\cos\vartheta\sin\varphi, \sin\vartheta, \cos\varphi\cos\vartheta)_S &= 0 \\ (-c\cos\vartheta\sin\varphi, b + c\sin\vartheta, a + c\cos\varphi\cos\vartheta) &= 0 \\ \Rightarrow c = 0 \quad , b = 0 \quad , a &= 0 \end{aligned} \tag{A.1}$$

We want to describe the point with S coordinates (x_1, y_1, z_1) in system Σ:

$$\begin{aligned} (x_1, y_1, z_1)_S &= \tilde{a}\vec{\varsigma} + \tilde{b}\vec{\tau} + \tilde{c}\vec{\upsilon} \\ &= \tilde{a}(0,0,1)_S + \tilde{b}(0,1,0)_S + \tilde{c}\,(-\cos\vartheta\sin\varphi, \sin\vartheta, \cos\varphi\cos\vartheta)_S \\ &\Rightarrow \\ \tilde{c} = -\frac{x_1}{\cos\vartheta\sin\varphi}, &\qquad \tilde{b} = y_1 + \frac{x_1\tan\vartheta}{\sin\varphi}, \qquad \tilde{a} = z_1 + \frac{x_1\cos\varphi}{\sin\varphi} \\ (x_1, y_1, z_1)_S &= \left(z_1 + \frac{x_1\cos\varphi}{\sin\varphi},\ y_1 + \frac{x_1\tan\vartheta}{\sin\varphi},\ -\frac{x_1}{\cos\vartheta\sin\varphi}\right)_\Sigma . \end{aligned} \tag{A.2}$$

The backward transformation – the point $(\varsigma_1, \tau_1, \upsilon_1)$ in Σ is described in system S as:

$$(\varsigma_1, \tau_1, \upsilon_1)_\Sigma = (-\upsilon_1\cos\vartheta\sin\varphi,\ \tau_1 + \upsilon_1\sin\vartheta,\ \varsigma_1 + \upsilon_1\cos\vartheta\cos\varphi)_S\,. \tag{A.3}$$

In Section 4.2.2 we also need the transformation between systems S'' and Σ. An arbitrary point with S'' coordinates (x_1'', y_1'', z_1'') is written as a linear combination of vectors $\vec{\varsigma}$, $\vec{\tau}$, and $\vec{\upsilon}$:

$$\begin{aligned} (x_1'', y_1'', z_1'')_{S''} &= \alpha\,\vec{\varsigma} + \beta\,\vec{\tau} + \gamma\,\vec{\upsilon} \\ &= \alpha\,(\sin\varphi, -\cos\varphi\sin\vartheta, \cos\varphi\cos\vartheta)_{S''} + \\ &\quad + \beta\,(0, \cos\vartheta, \sin\vartheta)_{S''} + \gamma(0,0,1)_{S''} \\ \Rightarrow \alpha &= \frac{x_1''}{\sin\varphi}, \\ \beta &= \frac{y_1''}{\cos\varphi} + \frac{x_1''\tan\vartheta}{\tan\varphi}, \\ \gamma &= z_1'' - \frac{x_1''}{\tan\varphi\cos\vartheta} - y_1''\tan\vartheta. \end{aligned} \tag{A.4}$$

And vice versa:

$$
\begin{aligned}
(\varsigma_1, \tau_1, \upsilon_1)_\Sigma &= \tilde{\alpha}\, \vec{e_{x''}} + \tilde{\beta}\, \vec{e_{y''}} + \tilde{\gamma}\, \vec{e_{z''}} \\
&= \tilde{\alpha} \left(\frac{1}{\sin\varphi}, \frac{\tan\vartheta}{\tan\varphi}, -\frac{1}{\tan\varphi\cos\vartheta} \right)_\Sigma + \\
&\quad + \tilde{\beta} \left(0, \frac{1}{\cos\vartheta}, -\tan\vartheta \right)_\Sigma + \tilde{\gamma}(0,0,1)_\Sigma \\
\Rightarrow \tilde{\alpha} &= \varsigma_1 \sin\varphi, \\
\tilde{\beta} &= \tau_1 \cos\theta - \varsigma_1 \cos\varphi \sin\vartheta, \\
\tilde{\gamma} &= \upsilon_1 + \varsigma_1 \cos\varphi \cos\vartheta + \tau_1 \sin\vartheta.
\end{aligned} \tag{A.5}
$$

To sum up, in tables A.1, A.2 and A.3 the description of basis vectors from the three coordinate systems are given.

basis vector	coordinates in S	coordinates in S''
$\vec{\varsigma}$	$(0,0,1)$	$(\sin\varphi, -\cos\varphi\sin\vartheta, \cos\vartheta\cos\varphi)$
$\vec{\tau}$	$(0,1,0)$	$(0, \cos\vartheta, \sin\vartheta)$
$\vec{\upsilon}$	$(-\sin\varphi\cos\vartheta, \sin\vartheta, \cos\varphi\cos\vartheta)$	$(0,0,1)$

Table A.2: Basis vectors of the coordinate systems Σ written in the coordinates of systems S and S''.

basis vector	coordinates in Σ
$\vec{e_x}$	$\left(\frac{1}{\tan\varphi}, \frac{\tan\vartheta}{\sin\varphi}, -\frac{1}{\cos\vartheta\sin\varphi}\right)$
$\vec{e_y}$	$(0,1,0)$
$\vec{e_z}$	$(1,0,0)$
$\vec{e_{x''}}$	$\left(\frac{1}{\sin\varphi}, \frac{\tan\vartheta}{\tan\varphi}, -\frac{1}{\tan\varphi\cos\vartheta}\right)$
$\vec{e_{y''}}$	$\left(0, \frac{1}{\cos\vartheta}, -\tan\vartheta\right)$
$\vec{e_{z''}}$	$(0,0,1)$

Table A.3: Basis vectors of the coordinate systems S and S''.

A.2 Photon path in flat thick targets

In Chapter 2 we came across thick metal targets, with flat surfaces. They were used as standard reference material (Sections 2.4 and 2.6). In our geometrical situation of the CF PIXE set-up, we are interested in the distance l, that photons travel in the target

on their way to the detector. The tilt angle α (Equation (2.6)) is assumed to be zero and the sample upper surface is aligned in the xy plane. The proton beam strikes the upper target surface at the position $(x_1, y_1, 0)$. The photon is created somewhere in the sample along its path, namely at the point $\vec{B} = (x_1, y_1, z_1)$. Photon travels along vector $-\vec{v}$, which points in the detector direction. At distance l from the creation point it crosses the target boundary at point $\vec{C} = (x_2, y_2, 0)$ and steps into vacuum. Vector $\vec{C}$ can be written as:

$$\vec{C} = l(-\vec{v}) + \vec{B}, \tag{A.6}$$

while the surface of the target can be described as a set of points P with position vector $\vec{r}$ that satisfy the relation:

$$(\vec{r} - \vec{C}) \cdot \vec{n} = 0. \tag{A.7}$$

$\vec{n}$ is the plane normal with coordinates $(0, 0, 1)$. The distance l between the points B and C is:

$$\begin{aligned} l &= \frac{(\vec{C} - \vec{B}) \cdot \vec{n}}{-\vec{v} \cdot \vec{n}} = \\ &= \frac{((x_2 - x_1), (y_2 - y_1), -z_1) \cdot (0, 0, 1)}{(\cos\vartheta \sin\varphi, -\sin\vartheta, -\cos\varphi\cos\vartheta) \cdot (0, 0, 1)} = \\ &= \frac{z_1}{\cos\vartheta\cos\varphi} \end{aligned} \tag{A.8}$$

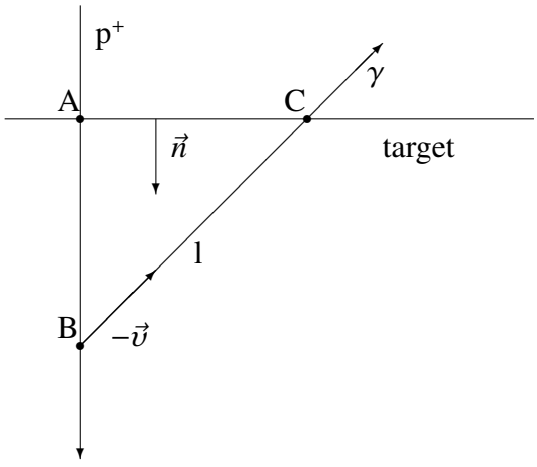

Figure A.1: Path of the emitted X-ray photons in thick target.

Appendix B

Secondary fluorescence

The major part of PIXE signal from GSR particles discussed in Chapter 4 consists of characteristic X-rays of Ti and Zn atoms. The number of Ti or Zn photons that are detected by the X-ray detector at a given proton beam and target position from every cell is given by Equation (4.2). However, some of the characteristic X-rays of Zn can be absorbed by Ti target atoms and as a consequence, additional Ti X-rays can be emitted. It is important to estimate the scale of the effect, neglected in the reconstruction process described in Chapter 4.

In order to calculate the additional Ti yield accurately, the rate of secondary emission from different directions and consequentially different absorption paths has to be considered. Careful analysis requires an accurate model and simulation and this is beyond the scope of this work. Moreover, the following rough estimate of the effect shows that in our conditions, the secondary fluorescence does not effect the results of the reconstruction significantly.

We can safely model the GSR particle as a sphere with 20 μm radius (R). A particle is considered homogeneous, with an average concentration of Ti and Zn, as determined by the reconstruction. As was argued when presenting results in Chapter 4, the average concentration of Ti atoms is $0.25 \cdot 10^{22}$ cm^{-3} or approximately 5% of the pure Ti value (not considering TiO_2!), while there is on average $1.7 \cdot 10^{22}$ cm^{-3} of Zn, or 26% of concentration in the pure Zn. The center of the sphere is considered to be aligned with the focal point of the lens and with the lens axis. Proton beam scans the surface of the sphere and at each position, the effect of the secondary fluorescence varies due to different lengths of photon path, the lens solid angle etc. The worst case scenario is when the proton beam is striking through the central point of the sphere, which is, as mentioned, at the center of the lens field of view.

Knowing the number of protons in the pixel (for the calculation we took approximately 10^9 protons in every pixel, a fairly realistic value) and the occupancy of the cell, the energy in the center of the cell is calculated from Equation (4.7) and the ionization cross sections at that point is estimated. Relating to Eq. (4.2) and (2.21), the number of Zn K_α photons emitted from the central cell in the whole solid angle after proton ionization is $1.1 \cdot 10^6$ and the number of proton induced Ti K_α photons is $8.3 \cdot 10^5$.

The fate of a single Zn K_α photon emitted in the central cell is:

- 9.7% to be absorbed by Ti atoms: $\left(1 - \exp\left[\frac{M_{\mathrm{Ti}}}{N_A} n_{at}^{\mathrm{Ti}} \left(\frac{\mu}{\rho}\right)_{\mathrm{Ti2}}\right] R\right)$,
- 14.5% to be absorbed by Zn atoms: $\left(1 - \exp\left[\frac{M_{\mathrm{Zn}}}{N_A} n_{at}^{\mathrm{Zn}} \left(\frac{\mu}{\rho}\right)_{\mathrm{Zn2}}\right] R\right)$,
- 75.8% to be transmitted out of the particle: $\left(\exp\left[\frac{M_{\mathrm{Ti}}}{N_A} n_{at}^{\mathrm{Ti}} \left(\frac{\mu}{\rho}\right)_{\mathrm{Ti2}} + \frac{M_{\mathrm{Zn}}}{N_A} n_{at}^{\mathrm{Zn}} \left(\frac{\mu}{\rho}\right)_{\mathrm{Zn2}}\right] R\right)$.

Quantities $\left(\frac{\mu}{\rho}\right)_{\mathrm{Ti2}}$ and $\left(\frac{\mu}{\rho}\right)_{\mathrm{Zn2}}$ were explained on page 101.

The Zn K_α photon that is absorbed by Ti atom may induce additional Ti K_α X-ray. The probability of this effect is governed by the fluorescence yield ω^{Ti} and b^{Ti}.

On the other hand, for a single Ti K_α photon created in the center of the sphere there is 56% probability that will be absorbed in the particle and the transmission probability is 44%. However, Ti K_α photon can not induce additional K_α X-rays of either of observed elements.

Estimating these rates, the number of Zn K_α X-rays that are transmitted out of the particle can be obtained, being $8.05 \cdot 10^5$. This is the measured yield neglecting absorption in the possible detector filters or the detector solid angle. The real yield is naturally much smaller, however these effects diminish the number of detected X-rays in the approximately same amount for all elements and are not considered.

Similarly, the number of Ti K_α X-rays transmitted out of the particle is $3.68 \cdot 10^5$. This is the yield related to the "true" Ti concentrations. Due to the secondary fluorescence, there are additional detected Ti photons that are misinterpreted in our model (Chapter 4) as belonging to the Ti atoms in the sample. The number of Ti K_α photons, induced by Zn K_α created in the center of the particle is:

$$N_{\mathrm{sec.fl.}}^{\mathrm{Ti}} = N_{\mathrm{prot}}^{\mathrm{Zn}} \left(1 - \exp\left[\frac{M_{\mathrm{Ti}}}{N_A} n^{\mathrm{Ti}} \left(\frac{\mu}{\rho}\right)_{\mathrm{Ti2}}\right] R\right) \omega^{Ti}\, b^{Ti} = 20100. \tag{B.1}$$

Therefore, due to the secondary fluorescence, the measured yield increases from $3.68 \cdot 10^5$ to $3.88 \cdot 10^5$. Computing the average concentration of Ti in the central cell from such increased yield, one would do about 5% error regarding the real values.

As already mentioned, this is expected to be the worst case scenario since all other cells in the particle would contribute less, due to the lack of surrounding material, different absorption paths, lens transmission probability, solid angles etc. Therefore, we estimate that in our case the secondary fluorescence effect amounts maximally few percent and can thus be neglected.

It is well known [1, 113] that the largest effect of the secondary fluorescence can be found in samples composed in majority of the "primary" element, while the concentration of the "secondary" element is small. Therefore it is interesting to estimate the upper limit in such case. The same procedure can be used, considering a spherical particle composed 99% of Zn and 1% of Ti. Here, the secondary fluorescence effect represents a dominant correction. The ratio $N^{\mathrm{Ti}}_{\mathrm{sec.fl.}}/N^{\mathrm{Ti}}_{\mathrm{prot}}$ from the central cell is 1.44, so the most of the detected Ti K_α X-ray are actually induced by X-ray emission of Zn atoms and not by protons. As mentioned, this is the maximum value and the effect for the whole particle is lower. Still however, without considering the secondary fluorescence effect, the reconstruction in such case would leed to large dicrepancies with respect to the real elemental concentrations.